学位論文

Theoretical study of exotic quantum phases in periodically-driven systems

(周期駆動系における新奇量子相の理論的研究)

平成28年12月博士（理学）申請

東京大学大学院理学系研究科

物理学専攻

北村 想太

Ph. D thesis

Theoretical study of exotic quantum phases in periodically-driven systems

Sota Kitamura
(北村 想太)

Department of Physics, University of Tokyo

December 2016

Abstract

In this thesis, we theoretically investigate exotic quantum phenomena underlying periodically-driven systems. We discuss three distinct systems, noninteracting Dirac systems, lattice systems with a strong repulsive interaction, and lattice systems with a strong attractive interaction. We reveal various novel phenomena underlying these systems, and provide clear understanding of them.

Periodically-driven systems, i.e., systems with a discrete time-translational symmetry, are described by the Floquet formalism, which maps the time-dependent Hamiltonian to a static "photon-dressed Hamiltonian". While a perturbative expansion of this Hamiltonian from the limit of high driving frequency has clarified various novel phenomena peculiar to periodically-driven systems, such an approach suffers from serious heating or damage when it is applied to realistic condensed matters.

In this thesis, we focus on a lower-frequency regime, especially when the heating should be suppressed due to the small driving amplitude or an energy gap larger than the driving frequency. There, the high-frequency expansion cannot capture the relevant physics, so that we first formulate various perturbative expansions for three distinct regimes, i.e., high-frequency, small-amplitude, and strong-coupling regimes.

We apply the small-amplitude expansion to two- and three-dimensional Dirac electrons driven by a circularly-polarized light to explore their behavior in the low-frequency regime. We find an emergence of infinite numbers of topological gaps for the former and Weyl nodes for the latter. We also discuss how a regularization of the model affects this topological structure.

We then introduce a strong repulsive interaction, and discuss behaviors of spins using the strong-coupling expansion. We predict an emergence of scalar spin chirality when a circularly-polarized light is illuminated, and discuss possible applications to photo-induced chiral spin liquids, and optical probing of spin chirality.

Finally we turn to a strong attractive interaction to discuss the fate of the ordinary s-wave superconductivity under the periodic driving. We demonstrate an emergence of long sought-after η-pairing superconductivity, first as a ground state of the photon-dressed Hamiltonian, and then as a consequence of a dynamical phase transition in an isolated system such as an optical lattice system.

Acknowledgments

I would like to express my deepest gratitude to Professor Hideo Aoki for his patient supervision and continuous encouragement on the present study. I am also indebted to Prof. Takashi Oka and Dr. Naoto Tsuji for a number of illuminating discussions and guidance during the research. It is a pleasure to thank Prof. Shinji Tsuneyuki and Prof. Ryotaro Arita for their helpful discussions and continual support. I am grateful to Dr. Leda Bucciantini, Sthitadhi Roy, Dr. Takahiro Mikami, and Kenji Yasuda, for stimulating discussions leading to great collaborations. I would like to acknowledge Prof. Masahito Ueda, Prof. Masaki Oshikawa, Prof. Yusuke Kato, Prof. Ryo Shimano, and Prof. Atsushi Fujimori for constructive comments and careful reading of the thesis. I would also like to thank Prof. Philipp Werner, Prof. Martin Eckstein, Dr. Hugo U. R. Strand, Prof. Masahiro Sato, Dr. Shintaro Takayoshi, Dr. Yasuhiro Tada, and Dr. Yohei Fuji for fruitful discussions and valuable suggestions. During the course of the present study, I have benefited from suggestions and comments by the previous and present members of Aoki-Tsuneyuki group. Especially I would like to thank Prof. P. Maksym, Dr. Y. Tatetsu, and M. Kitatani. Finally, I wish to thank my family for their continuous support and encouragement for the completion of the present study.

A list of publications

Publications relevant to the present thesis are marked with *.

[1] Sota Kitamura, Naoto Tsuji, and Hideo Aoki, "Interaction-Driven Topological Insulator in Fermionic Cold Atoms on an Optical Lattice: A Design with a Density Functional Formalism," Phys. Rev. Lett. **115**, 045304 (2015).

[2*] Takahiro Mikami, Sota Kitamura, Kenji Yasuda, Naoto Tsuji, Takashi Oka, and Hideo Aoki, "Brillouin-Wigner theory for high-frequency expansion in periodically driven systems: Application to Floquet topological insulators," Phys. Rev. B **93**, 144307 (2016).

[3*] Sota Kitamura and Hideo Aoki, "η-pairing superfluid in periodically-driven fermionic Hubbard model with strong attraction," Phys. Rev. B **94**, 174503 (2016).

[4] Chanchal Sow, Shingo Yonezawa, Sota Kitamura, Takashi Oka, Kazuhiko Kuroki, Fumihiko Nakamura, and Yoshiteru Maeno, "Current-induced Giant Diamagnetism in the Mott insulator Ca_2RuO_4," arXiv:1610.02222.

[5*] Leda Bucciantini, Sthitadhi Roy, Sota Kitamura, and Takashi Oka, "Emergent Weyl nodes and Fermi arcs in a Floquet Weyl semimetal," arXiv:1612.01541.

[6*] Sota Kitamura, Takashi Oka, and Hideo Aoki, "Circularly polarized lasers as a probe of spin chirality in Mott insulators," in preparation.

Contents

Chapter 1

Introduction

1.1 Motivation of the thesis

One of major goals in studies of condensed-matter physics is to control phases of matter and their physical properties. The photo-induced phase transition [1, 2], the phase transition triggered by illuminating light, opens up a plenty of possibilities for achieving of this goal, and yields new ways to control materials as well, such as dynamical switching of material properties.

A significant difference of the photo-induced phase transition from conventional ones is that it is a nonequilibrium phenomenon, where richer physics unattainable in equilibrium systems can emerge. To explore and understand such exotic phenomena peculiar to nonequilibrium systems is one of strong aims in studies of the photo-induced phase transition.

The study of the photo-induced phase transitions has been attracting growing interests stimulated by recent developments in experimental techniques. Along with wider intensity and frequency ranges of available lasers, a key experimental technique is the pump-probe measurement. There, an intense pump laser pulse is applied for exciting the system, with a probe laser applied subsequently with some time delay for observing transient responses. The temporal evolution of the system is tracked by sweeping the time delay, with reflectance measurements for an optical conductivity and with photoemission measurements for a density of occupied states. They enable us to observe ultrafast real-time dynamics of electrons directly, which yields a number of remarkable reports including experimental evidences for the photo-induced metal-insulator [3], superconductivity [4–6], and topological phase transitions [7–10].

Remarkable progress in experimental techniques in ultracold atom systems has also been accelerating the understanding and interests in nonequilibrium phenom-

ena. The optical lattice [11, 12], optical potential from standing waves of lasers, provides an ideal realization of an isolated correlated lattice model such as the Hubbard model. Various measurement techniques including in situ imaging of atomic density [13] and the momentum distribution [14] make the cold atom systems as a suitable platform for investigating various nonequilibrium phenomena. The time scale in the cold atom systems, which is orders of magnitude slower than in solid-state systems, also helps nonequilibrium experiments. Recent progress even provides information in a single-site resolution and non-destructive manners [15].

There are also increasing fascinations in theoretical studies of nonequilibrium phenomena including the photo-induced phase transition. While there are diverse approaches for analyzing microscopic quantum systems out of equilibrium [16–24], the Floquet formalism among them is arousing much interests for investigating interesting nonequilibrium phenomena. The Floquet formalism is a framework for periodically-driven quantum systems, i.e., systems with a discrete time-translational symmetry, which stems from a mathematical theorem for periodic ordinary differential equations [25]. There, nonequilibrium steady states are described in terms of an effective Hamiltonian for "photon-dressed" electrons, called the Floquet Hamiltonian. The Floquet Hamiltonian turns out to provide nontrivial forms hard to implement in equilibrium systems, which urges us to recognize optically-driven systems anew as a platform for potentially novel physics beyond a simple heating.

One advantage in this formalism is that one can employ a perturbative approach, which enables us to analytically treat complicated nonequilibrium phenomena, as well as to grasp a clear physical picture. Thanks to this, several phenomena, which are peculiar but universal to periodically-driven systems, have been established. One of them is the dynamical localization [26] on lattice systems and the accompanying photo-induced Mott transition [27, 28], where the band width is dynamically reduced due to the periodic driving (see Sec. 4.1 in the present thesis for details). It has been observed in bosonic optical lattice systems with a remarkable agreement between theory and experiment [29, 30], and is even realized in an organic conductor using a short pulse [31]. Another phenomenon which has successfully been analyzed in terms of the Floquet picture is the Floquet topological phase transition [32, 33]. As we shall review and discuss in detail in Chapter 3, the Floquet Hamiltonian under a circularly-polarized laser has turned out to realize a model that shows the quantum Hall effect without Landau levels (so-called "anomalous quantum Hall effect"), which had been regarded as an unrealistic toy model. This phenomenon is also confirmed experimentally, first by using a surface state of topological insulators [7, 8, 10], and also in cold atom systems [9] as a more direct implementation of the original proposal [32].

Theoretical understanding of these phenomena has been obtained clearly by a perturbative approach from the limit of high driving frequency [34–37]. However, as the target of interest evolves from noninteracting systems to correlated systems, a fatal flaw inherent in the formalism has been clarified. The Floquet formalism is based on a discrete temporal translational symmetry, so that it describes continuously-driven systems. Particularly for closed systems without any dissipation channel, the framework may not make sense, since their temperature may increase ad infinitum in thermodynamical arguments. Indeed, in the thermodynamic limit, the Floquet Hamiltonians have turned out to be random matrices in general, except for integrable systems [38, 39]. Namely, it has been clarified that the perturbative expansion of the Floquet Hamiltonian is only an asymptotic expansion.

On the other hand, as the phenomena found with the asymptotic expansion are indeed observed experimentally, such expansions must retain some meaning. Indeed, it has been shown that heating of the system becomes very slow when the driving frequency is much higher than all the typical energy scales in the system considered [40, 41].

While basic properties of the periodically-driven systems described by the Floquet formalism have continued to be revealed and comprehended, there has still been a large gap between experiments and theories. The suppression of the heating in the high-frequency driving should be spoiled in realistic situations, where a number of high-energy states not considered in a theoretical model may exist, which give upper bounds for the frequency such as the work function for the photoelectric effect or the damaged samples via, e.g., interband transitions and phonon excitations. Hence, to achieve a microscopic understanding of intriguing experiments and to propose a feasible proposal from a theoretical view, we should,

1. clarify the relation between the Floquet Hamiltonian, which describes continuously-driven systems, and real-time dynamics on an ultrafast time scale where serious heating or damage does not start.

2. explore novel phenomena in a lower-frequency regime, where the high-frequency expansion cannot capture the relevant physics, especially when the driving amplitude is small or when there is an energy gap larger than the driving frequency, since the heating should be suppressed in these situations.

In the present thesis, we focus on the latter problem; namely, we explore exotic phenomena in the periodically-driven quantum systems, especially in the cases where the high-frequency expansion cannot be applied. We discuss:

1. noninteracting Dirac systems (in Chapter 3), where we predict an emergence of infinite numbers of topological gaps for the Floquet topological insulators

and Weyl nodes for Floquet Weyl semimetals in the low-frequency regime by constructing a Brillouin-Wigner formalism,

2. lattice systems with a strong repulsive interaction (in Chapter 4), where we predict an emergence of scalar spin chirality when a circularly-polarized light is illuminated,

3. lattice systems with a strong attractive interaction (in Chapter 5), where we predict an emergence of long sought-after η-pairing superconductivity.

We formulate various perturbative expansions for each case, and analyze nontrivial structures appearing in obtained Floquet Hamiltonians. We provide understanding of the novel phenomena emerging from them in this thesis.

1.2 Organization of the thesis

Here we present the contents of the present thesis.

In Chapter 2, we first review the Floquet formalism as a fundamental framework for the present study. There, we introduce the basic notions in the Floquet formalism, a quasienergy as an analog of the crystal momentum in time domain, and various frameworks to describe the quasienergy eigenstates. We also review statistical properties of the periodically-driven systems.

Then in Chapter 3 we discuss the Floquet topological phases realized in noninteracting Dirac systems driven by a circularly-polarized laser. After a brief review given in Sec. 3.1, we formulate a perturbative expansion using the Brillouin-Wigner theory in Sec. 3.2. While the earlier perturbative formulations are based on a unitary transformation, here we consider a new one based on a projection. This yields a much more transparent picture with a smaller number of terms. The expansion is also applicable to resonant structures emerging in the low-frequency driving, by choosing an appropriate projection. We discuss topological structures in such a regime in Secs. 3.3 and 3.4, for two- and three-dimensional Dirac systems, which host the "Floquet topological insulator" and "Floquet Weyl semimetal" phases, respectively.

Chapter 4 is devoted to the system with strong repulsive interactions driven by the circularly-polarized light. In Sec. 4.2, we consider a strong-coupling expansion in the presence of the periodic driving, and derive the low-energy Hamiltonian for the spin degree of freedom in a systematic manner. The circularly-polarized laser induces a three-body correlation called the "spin scalar chirality" (as introduced in Sec. 4.1), which we discuss in Sec. 4.3, in particular on a chiral spin-liquid phase and an optical response of general Mott insulators.

In Chapter 5 we turn to the attractively-interacting systems. We discuss the fate of the ordinary s-wave superconductivity under the periodic driving. We first introduce an important symmetries (spin-SU(2) and η-SU(2)) known in the Hubbard model, and its significant modification in nonequilibrium situations in Sec. 5.2. We apply the strong-coupling expansion given in Sec. 4.2 to the attractive case, and discuss the obtained Hamiltonian for Cooper pairs in Sec. 5.3. This reveals an emergence of the η-pairing superconductivity as a ground state. We then discuss how to induce the phase transition to η-pairing superconductivity dynamically. We perform a stability analysis in Sec. 5.4, and reveal the presence of the dynamical instability. We exploit this to propose protocols for the dynamical phase transition, and demonstrate by calculating mean-field time evolution in Sec. 5.5. We also discuss experimental implications for cold atom systems in Sec. 5.5.

Finally, we conclude the thesis in Chapter 6.

Chapter 2

Floquet formalism

In this chapter, we shall introduce the Floquet formalism, a fundamental framework for analyzing periodically-driven systems. The Floquet formalism itself has a long history starting from the establishment of a theorem on periodic ordinary differential equations, the Floquet theorem, in 1883 [25]. Here we concentrate on quantum mechanical applications [42–45], and explain from a modern view to clarify relations between various frameworks.

The periodically-driven systems are defined as systems with a discrete time-translational symmetry, so that the conserved quantity in this symmetry, the quasienergy, is an important observable to characterize the system. The quasienergy is the temporal analog of the crystal momentum in a spatially periodic potential.

First, by starting from a mathematical structure in the discrete time translation, we derive the concept of the quasienergy and several frameworks to calculate quasienergy eigenstates.

While the dynamics of the periodically-driven systems is characterized by the quasienergy, statistical mechanics of the periodically-driven systems, being nonequilibrium, has not been established completely so far, including the relation with the quasienergy spectrum. This is an important open question in nonequilibrium statistical mechanics, and we would like to review recent progress in this field, and explain the motivation why we focus on the quasienergy eigenstates.

2.1 Quasienergy eigenstates

2.1.1 Effective Hamiltonian at stroboscopic times

In general, for a quantum system with a time-dependent Hamiltonian, the system is described by the time-evolution operator. The time-evolution operator from time t_0

to t, denoted here as $\hat{U}(t,t_0)$, can be explicitly expressed as

$$\hat{U}(t,t_0) = \sum_{\alpha} |\alpha(t)\rangle\langle\alpha(t_0)| \tag{2.1}$$

with an arbitrary basis in the Schrödinger representation $\{|\alpha(t)\rangle\}$. From this definition, it follows

$$\hat{U}(t,t) = 1, \tag{2.2}$$

$$\hat{U}^{\dagger}(t,t_0) = \hat{U}(t_0,t), \tag{2.3}$$

$$\hat{U}(t,t')\hat{U}(t',t_0) = \hat{U}(t,t_0). \tag{2.4}$$

The time-evolution operator obeys the time-dependent Schrödinger equation,

$$i\partial_t \hat{U}(t,t_0) = \hat{H}(t)\hat{U}(t,t_0). \tag{2.5}$$

This equation of motion has a formal solution with an infinite series

$$\begin{aligned}\hat{U}(t,t_0) &= \mathscr{T}\exp\left[-i\int_{t_0}^{t} dt'\,\hat{H}(t')\right] \\ &= \sum_{n=0}^{\infty}\frac{(-i)^n}{n!}\int_{t_0}^{t} dt_1 \cdots \int_{t_0}^{t} dt_n\,\mathscr{T}\left[\hat{H}(t_1)\ldots\hat{H}(t_n)\right],\end{aligned} \tag{2.6}$$

where $\mathscr{T}[\ldots]$ represents a time-ordered product.

If the Hamiltonian $\hat{H}$ is time-independent, the time-evolution operator is represented as

$$\hat{U}(t_0+t,t_0) = e^{-i\hat{H}t}, \tag{2.7}$$

which manifests the temporal translational invariance of the system. Namely, eigenstate of $\hat{H}$ remains the eigenstate under a time evolution, with the eigenvalue conserved. While such a conservation law is invalidated for the time-dependent Hamiltonian, a discrete translational symmetry

$$\hat{H}(t) = \hat{H}(t+T), \tag{2.8}$$

still holds for periodically-driven systems with a driving frequency $\omega = 2\pi T^{-1}$. For these special cases, the time-evolution operator has a periodicity

$$\hat{U}(t+T,t_0+T) = \hat{U}(t,t_0), \tag{2.9}$$

and in particular,

$$\hat{U}(t_0+nT,t_0) = [\hat{U}(t_0+T,t_0)]^n \tag{2.10}$$

holds with an arbitrary integer n. This property is analogous to the case of continuous translation, Eq. (2.7); if we denote

$$\hat{U}(t_0+T,t_0)=e^{-i\hat{F}(t_0)T}, \tag{2.11}$$

stroboscopic time evolution of state vectors at $t=t_0+nT$ can be regarded as if it is evolved under a static Hamiltonian

$$\hat{F}(t_0)=\frac{i}{T}\ln\hat{U}(t_0+T,t_0). \tag{2.12}$$

$\hat{F}(t_0)$ is called the Floquet-Magnus Hamiltonian (or the stroboscopic Floquet Hamiltonian), and the eigenvalues of $\hat{F}(t_0)$ are called quasienergy, which is a temporal analog of the crystal momentum in a spatially periodic potential. The quasienergy has an indefiniteness of integer multiples of $\omega=2\pi T^{-1}$ due to the complex logarithm.

Let us consider the eigenstate of $\hat{F}(t_0)$ (or $\hat{U}(t_0+T,t_0)$), which we denote as

$$\hat{F}(t_0)|\psi(t_0)\rangle=\epsilon|\psi(t_0)\rangle, \tag{2.13}$$

and its time evolution

$$|\psi(t)\rangle\equiv\hat{U}(t,t_0)|\psi(t_0)\rangle. \tag{2.14}$$

For $t\neq t_0+nT$, $|\psi(t)\rangle$ is not an eigenstate of $\hat{F}(t_0)$ in general, while for $t=t_0+nT$ it is [due to Eq. (2.11)]. However, since

$$\begin{aligned}\hat{U}(t+T,t)|\psi(t)\rangle&=\hat{U}(t+T,t_0+T)\hat{U}(t_0+T,t_0)|\psi(t_0)\rangle\\&=\hat{U}(t,t_0)e^{-i\epsilon T}|\psi(t_0)\rangle=e^{-i\epsilon T}|\psi(t)\rangle,\end{aligned} \tag{2.15}$$

$|\psi(t)\rangle$ is the eigenstate of $\hat{U}(t+T,t)$ and $\hat{F}(t)$, with a time-independent eigenvalue ϵ. Namely, the quasienergy ϵ characterizes the time evolution of periodically-driven systems as a conserved quantity derived from the discrete temporal translational symmetry. The quasienergy can be calculated by diagonalizing Eq. (2.12), and the eigenvector represents the snapshot of the quasienergy eigenstate at $t=t_0$. The time-dependence of the quasienergy eigenstate can be obtained by applying $\hat{U}(t,t_0)$.

2.1.2 Effective Hamiltonian in an extended Hilbert space

As we have seen, the mathematical structure of periodically-driven systems has a tight relation to that of the static systems: In terms of the stroboscopic time evolution, Eq. (2.11), effects of the periodic driving can be regarded as a modulation of the static Hamiltonian.

However, this modulation should not be directly interpreted as a physical effect because the Floquet-Magnus Hamiltonian has a spurious dependence on a strobe timing t_0. Namely, the Floquet-Magnus Hamiltonian $\hat{F}(t_0)$ represents information at a particular time t_0, which is physically meaningless, rather than physical information of the system itself. This sometimes results in, for instance, a loss of characteristic symmetries for the system from the effective Hamiltonian. While this does not matter as a prescription for calculating quasienergy eigenstates, we are often interested in the physical meaning of the effective Hamiltonian itself, so that it would be undesirable.

Thus in this subsection we would like to discuss properties of the quasienergy eigenstate $|\psi(t)\rangle$ itself, without picking up a particular time t_0. First, let us rewrite the time-evolution operator as

$$\hat{U}(t,t_0) = e^{-i\hat{\Lambda}(t,t_0)} e^{-i\hat{F}(t_0)(t-t_0)}. \tag{2.16}$$

Here the second exponential factor describes a static time evolution generated by the effective static Hamiltonian $\hat{F}(t_0)$, while the first one describes deviation[1] from the eigenstate of $\hat{F}(t_0)$ at $t \neq t_0 + nT$. The definition of $\hat{F}(t_0)$, Eq. (2.12), reads

$$\hat{\Lambda}(t+T,t_0) = \hat{\Lambda}(t,t_0), \tag{2.17}$$

with a boundary condition $\hat{\Lambda}(t_0,t_0) = 0$, i.e., $\hat{\Lambda}(t,t_0)$ is a time-periodic function. Thus, from Eqs. (2.14, 2.16), the quasienergy eigenstates at general time t, $|\psi(t)\rangle$, can be written as [25]

$$|\psi(t)\rangle = e^{-i\hat{\Lambda}(t,t_0)}|\psi(t_0)\rangle e^{-i\epsilon(t-t_0)} \equiv |u(t)\rangle e^{-i\epsilon t}, \tag{2.18}$$

with a time-periodic state vector $|u(t+T)\rangle = |u(t)\rangle$. From the equation of motion, the time-periodic part $|u(t)\rangle$ satisfies

$$\sum_{n=-\infty}^{\infty} (\hat{H}_{m-n} - \delta_{m-n} m\omega)|u_n\rangle = \epsilon|u_m\rangle, \tag{2.19}$$

[1]Sometimes this deviation is called a micromotion, and $e^{-i\hat{\Lambda}(t,t_0)}$ a micromotion operator [37], or a fast-motion operator [36].

or, in a matrix form,

$$\begin{pmatrix} \ddots & \ddots & \ddots & & \\ \ddots & \hat{H}_0 - \omega & \hat{H}_{+1} & \hat{H}_{+2} & \\ \ddots & \hat{H}_{-1} & \hat{H}_0 & \hat{H}_{+1} & \ddots \\ & \hat{H}_{-2} & \hat{H}_{-1} & \hat{H}_0 + \omega & \ddots \\ & & \ddots & \ddots & \ddots \end{pmatrix} \begin{pmatrix} \vdots \\ |u_1\rangle \\ |u_0\rangle \\ |u_{-1}\rangle \\ \vdots \end{pmatrix} = \epsilon \begin{pmatrix} \vdots \\ |u_1\rangle \\ |u_0\rangle \\ |u_{-1}\rangle \\ \vdots \end{pmatrix}, \tag{2.20}$$

where

$$\hat{H}(t) = \sum_{m=-\infty}^{\infty} \hat{H}_m e^{-im\omega t}, \tag{2.21}$$

$$|u(t)\rangle = \sum_{m=-\infty}^{\infty} |u_m\rangle e^{-im\omega t}. \tag{2.22}$$

Namely, the calculation of the quasienergy eigenstates can be reformulated as a matrix eigenvalue problem in the extended Hilbert space [43] (the Sambe space). Because the Floquet state may be regarded as a photon-dressed electronic state, the additional index to label Fourier components is sometimes referred to as a "photon number", although it can take negative values.

While the extension of the Hilbert space makes the number of eigenstates larger, additional eigenstates are merely redundant solutions due to the indefiniteness of quasienergy; i.e., if $\{|u_m\rangle\}_{m=-\infty}^{\infty} \equiv {}^t(\ldots, |u_{-1}\rangle, |u_0\rangle, |u_1\rangle, \ldots)$ is the eigenvector with eigenvalue ϵ, $\{|u_{m+1}\rangle\}_{m=-\infty}^{\infty} = {}^t(\ldots, |u_0\rangle, |u_1\rangle, |u_2\rangle, \ldots)$ is also the eigenvector, with an eigenvalue $\epsilon + \omega$. They are distinguished in the extended Hilbert space, but give the same eigenvector in the original Hilbert space, as Eq. (2.18).

2.1.3 Effective Hamiltonian for dressed particles

We have derived an effective static Hamiltonian Eq. (2.20), without any dependence on strobe timing t_0, but in turn it has an additional degree of freedom, the photon number. It is indeed a static Hamiltonian, but now one cannot interpret the effect of the periodic driving as a modulation of the static Hamiltonian defined in a common Hilbert space. Here we consider to reduce the dimension of the Floquet Hamiltonian in the extended Hilbert space by a block diagonalization.

First we note that the Floquet-Magnus Hamiltonian Eq. (2.12) can also be regarded as a result of the block diagonalization of Eq. (2.20). By differentiating

Eq. (2.16) and using Eq. (2.5), we can rewrite $\hat{F}(t_0)$ as

$$\hat{F}(t_0) = e^{i\hat{\Lambda}(t,t_0)}(\hat{H}(t) - i\partial_t)e^{-i\hat{\Lambda}(t,t_0)} \tag{2.23}$$

$$= \sum_{n=-\infty}^{\infty}\sum_{m=-\infty}^{\infty} \hat{U}_{-n}(\hat{H}_{n-m} - \delta_{n-m}m\omega)\hat{U}_m^\dagger, \tag{2.24}$$

by [2] expanding $e^{-i\hat{\Lambda}(t,t_0)}$ in a Fourier series as

$$e^{-i\hat{\Lambda}(t,t_0)} = \sum_{m=-\infty}^{\infty} \hat{U}_m^\dagger e^{-im\omega t}. \tag{2.25}$$

Namely, $e^{-i\hat{\Lambda}(t,t_0)}$ is a time-periodic unitary transformation which block-diagonalizes the Hamiltonian Eq. (2.20) to eliminate the time dependence.

While the unitary transformation that block-diagonalizes Eq. (2.20) is not unique, here $\hat{\Lambda}(t,t_0)$ is uniquely[3] determined because of the boundary condition $\hat{\Lambda}(t_0,t_0) = 0$. Thus, if one chooses other boundary conditions, one can generate an effective Hamiltonian other than the Floquet-Magnus Hamiltonian with the original dimension. We can choose a new unitary transformation

$$\hat{F}_\Gamma = e^{i\hat{\Gamma}(t)}(\hat{H}(t) - i\partial_t)e^{-i\hat{\Gamma}(t)}, \tag{2.26}$$

with a natural boundary condition

$$\int_0^T dt\,\hat{\Gamma}(t) = 0, \tag{2.27}$$

which means that the transformation does not introduce further hybridization within a block labeled by the photon number. Namely, we can regard the transformed basis as that of "dressed particles".

By applying $\hat{U}(t_0,t)e^{-i\hat{\Gamma}(t)}$ from the left to Eq. (2.26) and integrating it over $[t_0,t]$, we have

$$\hat{U}(t,t_0) = e^{-i\hat{\Gamma}(t)}e^{-i\hat{F}_\Gamma(t-t_0)}e^{i\hat{\Gamma}(t_0)}, \tag{2.28}$$

so that it is related to the Floquet-Magnus Hamiltonian via

$$\hat{F}_\Gamma = e^{i\hat{\Gamma}(t_0)}\hat{F}(t_0)e^{-i\hat{\Gamma}(t_0)}, \tag{2.29}$$

$$e^{-i\hat{\Gamma}(t)}e^{i\hat{\Gamma}(t_0)} = e^{-i\hat{\Lambda}(t,t_0)}. \tag{2.30}$$

[2] Here, we denote $\hat{U}_m^\dagger = (\hat{U}^\dagger)_m = (\hat{U}_{-m})^\dagger$.
[3] This is up to integer multiples of 2π.

Also, an eigenstate of $\hat{F}_\Gamma$, $|u_\Gamma\rangle$, is related to a quasienergy eigenstate as

$$|\psi(t)\rangle = e^{-i\hat{\Gamma}(t)}|u_\Gamma\rangle e^{-i\epsilon t}. \tag{2.31}$$

Now, the problem is how to determine $\hat{\Gamma}(t)$ systematically. One way to calculate $e^{-i\hat{\Gamma}(t)}$ and $\hat{F}_\Gamma$ is the perturbative expansion [36, 37], which we explain in the next subsection. Another way to construct $\hat{F}_\Gamma$ is the continuous unitary transformation (also known as the flow equation approach [22, 46]). Namely, we consider a transformation parametrized by a flow parameter l, to block-diagonalize the Hamiltonian in the extended Hilbert space,

$$\hat{F}_{i-j}(l) - \delta_{i-j} j\omega = \sum_{n=-\infty}^{\infty} \sum_{m=-\infty}^{\infty} \hat{U}_{i-n}(l)(\hat{H}_{n-m} - \delta_{n-m} m\omega)\hat{U}^\dagger_{m-j}(l). \tag{2.32}$$

Here we have introduced a canonical generator[4] of the transformation

$$\hat{\eta}_n(l) = -n\omega \hat{F}_n(l), \tag{2.33}$$

which defines a continuous transformation as

$$\partial_l \hat{U}_m(l) = \sum_{n=-\infty}^{\infty} \hat{\eta}_n(l)\hat{U}_{m-n}(l). \tag{2.34}$$

This generator leads to a flow equation for $\hat{F}_m(l)$ as

$$\partial_l \hat{F}_m(l) = -m^2\omega^2 \hat{F}_m(l) - \sum_{n=-\infty}^{\infty} n\omega[\hat{F}_n(l), \hat{F}_{m-n}(l)], \tag{2.35}$$

or, in the time domain,

$$\frac{\partial \hat{F}}{\partial l} = \frac{\partial^2 \hat{F}}{\partial t^2} - i\left[\frac{\partial \hat{F}}{\partial t}, \hat{F}\right]. \tag{2.36}$$

Since the generator does not have the intra-sector ($n = 0$) term, asymptotic forms for $l \to \infty$ should be

$$\hat{F}_m(l) \to \hat{F}_\Gamma \delta_m, \tag{2.37}$$

$$\sum_{m=-\infty}^{\infty} \hat{U}_m(l) e^{-im\omega t} \to e^{i\hat{\Gamma}(t)}, \tag{2.38}$$

if we assume that $\hat{F}_m(l)$ converges to a static solution. This can be explicitly

[4] In Ref. [22], a different generator is chosen to reproduce the Floquet-Magnus Hamiltonian for $l \to \infty$.

checked by expanding the flow equation Eq. (2.35) and Eq. (2.26) in ω^{-1} and compare them [22].

2.1.4 High-frequency expansion

So far, we have introduced three different formalisms to calculate quasienergy eigenstates. However, except for very limited cases, the exact analytical solution is impossible to obtain even for noninteracting systems. One can invoke numerical methods for calculating quasienergy eigenstates; the numerical integration of Eqs. (2.5, 2.35) yields the Floquet-Magnus Hamiltonian and the effective Hamiltonianfor dressed particles, respectively. One can also diagonalize Eq. (2.20) numerically, by truncating the Fourier index at a sufficiently large number, although the existence of redundant solutions makes practical computations not so efficient. The numerical integration requires computational costs of, at least[5], $\mathcal{O}(N^3)$ with N being the dimension of the original Hilbert space, which is comparable to the exact diagonalization. Thus the application is more or less limited to noninteracting or few-body systems.

Here we introduce an alternative way to calculate the effective Hamiltonian by the perturbative expansion, which is referred to as the high-frequency expansion. Both the Floquet-Magnus Hamiltonian and the dressed-particle Hamiltonian are obtained as the block diagonalization of the static Hamiltonian in the extended Hilbert space as

$$\hat{F} = e^{i\hat{\Lambda}(t)}(\hat{H}(t) - i\partial_t)e^{-i\hat{\Lambda}(t)}. \tag{2.39}$$

As we have seen, the boundary condition $\hat{\Lambda}(t_0) = 0$ reproduces the Floquet-Magnus Hamiltonian $\hat{F}(t_0)$, while $\int dt\hat{\Lambda}(t) = 0$ the dressed-particle one $\hat{F}_\Gamma$. Thus, by expanding $\hat{\Lambda}(t)$ and the effective Hamiltonian $\hat{F}$ in an infinite series, one can evaluate them order by order.

Here, we first derive the equation of motion for[6] $\hat{\Lambda}(t)$, instead of $e^{-i\hat{\Lambda}(t)}$. The first term in Eq. (2.39) can be expressed as

$$\begin{aligned} e^{i\hat{\Lambda}(t)}\hat{H}(t)e^{-i\hat{\Lambda}(t)} &= \sum_{n=0}^{\infty}\frac{1}{n!}\left[\frac{\partial^n}{\partial\lambda^n}(e^{i\lambda\hat{\Lambda}(t)}\hat{H}(t)e^{-i\lambda\hat{\Lambda}(t)})\right]_{\lambda=1} = \sum_{n=0}^{\infty}\frac{1}{n!}\mathrm{ad}^n_{i\hat{\Lambda}(t)}\hat{H}(t) \\ &= \exp[\mathrm{ad}_{i\hat{\Lambda}(t)}]\hat{H}(t) \qquad (2.40) \\ &= \hat{H}(t) + [i\hat{\Lambda}(t),\hat{H}(t)] + \frac{1}{2!}[i\hat{\Lambda}(t),[i\hat{\Lambda}(t),\hat{H}(t)]] + \dots, \qquad (2.41) \end{aligned}$$

[5]For the flow equation, we have the additional Fourier index, so that the computational cost is more demanding.

[6]Sometimes $\hat{\Lambda}(t)$ is called the kick operator [36].

where $\mathrm{ad}_X \bullet \equiv [X, \bullet]$. Similarly, the second term is expressed as

$$\begin{aligned} e^{i\hat{\Lambda}(t)} i\partial_t e^{-i\hat{\Lambda}(t)} &= \int_0^1 d\lambda \frac{\partial}{\partial\lambda}(e^{i\lambda\hat{\Lambda}(t)} i\partial_t e^{-i\lambda\hat{\Lambda}(t)}) \\ &= \int_0^1 d\lambda e^{i\lambda\hat{\Lambda}(t)} \frac{\partial\hat{\Lambda}}{\partial t} e^{-i\lambda\hat{\Lambda}(t)} = \int_0^1 d\lambda \exp[\lambda \mathrm{ad}_{i\hat{\Lambda}}] \frac{\partial\hat{\Lambda}}{\partial t} \\ &= \frac{\exp[\mathrm{ad}_{i\hat{\Lambda}}] - 1}{\mathrm{ad}_{i\hat{\Lambda}}} \frac{\partial\hat{\Lambda}}{\partial t}. \end{aligned} \tag{2.42}$$

Thus the equation of motion is expressed as

$$\frac{\partial\hat{\Lambda}}{\partial t} = \frac{\mathrm{ad}_{-i\hat{\Lambda}}}{\exp[\mathrm{ad}_{-i\hat{\Lambda}}] - 1} \hat{H}(t) - \frac{\mathrm{ad}_{i\hat{\Lambda}}}{\exp[\mathrm{ad}_{i\hat{\Lambda}}] - 1} \hat{F}. \tag{2.43}$$

Since

$$\frac{x}{e^x - 1} = \sum_{n=0}^{\infty} \frac{B_n}{n!} x^n \tag{2.44}$$

is the generating function for the Bernoulli number[7] B_n, we have [34, 35]

$$\frac{\partial\hat{\Lambda}}{\partial t} = \sum_{n=0}^{\infty} \frac{B_n}{n!} \mathrm{ad}_{i\hat{\Lambda}}^n ((-1)^n \hat{H}(t) - \hat{F}). \tag{2.45}$$

Since $\hat{\Lambda}(t)$ and $\hat{H}(t)$ are time-periodic functions, they can be decomposed into the Fourier components as $\hat{\Lambda}(t) = \sum_{m=-\infty}^{\infty} \hat{\Lambda}_m e^{-im\omega t}$ and $\hat{H}(t) = \sum_{m=-\infty}^{\infty} \hat{H}_m e^{-im\omega t}$. Then Eq. (2.45) becomes a set of algebraic equations for $\hat{\Lambda}_m$ with $m \neq 0$, while $\hat{\Lambda}_0$ is determined from the boundary condition.

One can construct a series solution by expanding $\hat{\Lambda}_m = \sum_{n=1}^{\infty} \hat{\Lambda}_m^{(n)}$ and $\hat{F} = \sum_{n=0}^{\infty} \hat{F}_m^{(n)}$ as a function of $1/\omega$. With the boundary condition $\hat{\Lambda}(t_0 = 0) = 0$, the Floquet-

[7] $B_0 = 1, B_1 = -1/2, B_2 = 1/6, B_3 = 0, B_4 = -1/30, B_5 = 0, B_6 = 1/42, B_7 = 0, B_8 = -1/30, \ldots$

Magnus Hamiltonian is obtained as [28, 34, 35]

$$\hat{F}^{(0)} = \hat{H}_0, \tag{2.46}$$

$$\hat{F}^{(1)} = \sum_{m\neq 0} \frac{[\hat{H}_{-m}, \hat{H}_m]}{2m\omega} + \sum_{m\neq 0} \frac{[\hat{H}_m, \hat{H}_0]}{m\omega}, \tag{2.47}$$

$$\begin{aligned}\hat{F}^{(2)} = &\sum_{m\neq 0} \frac{[[\hat{H}_{-m}, \hat{H}_0], \hat{H}_m]}{2m^2\omega^2} + \sum_{m\neq 0} \sum_{n\neq 0,m} \frac{[[\hat{H}_{-m}, \hat{H}_{m-n}], \hat{H}_n]}{3mn\omega^2} \\ &- \sum_{m\neq 0} \frac{[[\hat{H}_m, \hat{H}_0], \hat{H}_0]}{m^2\omega^2} - \sum_{m,n\neq 0} \frac{[[\hat{H}_m, \hat{H}_n], \hat{H}_{-n}]}{3mn\omega^2} + \sum_{m,n\neq 0} \frac{[[\hat{H}_n, \hat{H}_{-n}], \hat{H}_m]}{3mn\omega^2} \\ &- \sum_{m\neq 0} \sum_{n\neq 0,m} \frac{[[\hat{H}_n, \hat{H}_{m-n}], \hat{H}_0]}{2mn\omega^2} + \sum_{m,n\neq 0} \frac{[[\hat{H}_m, \hat{H}_n], \hat{H}_0]}{2mn\omega^2} - \sum_{m,n\neq 0} \frac{[[\hat{H}_m, \hat{H}_0], \hat{H}_n]}{2mn\omega^2},\end{aligned} \tag{2.48}$$

with

$$i\hat{\Lambda}_0^{(n)} = -i \sum_{m\neq 0} \hat{\Lambda}_m^{(n)}, \tag{2.49}$$

$$i\hat{\Lambda}_{m\neq 0}^{(1)} = -\frac{\hat{H}_m}{m\omega}, \tag{2.50}$$

$$i\hat{\Lambda}_{m\neq 0}^{(2)} = \frac{[\hat{H}_m, \hat{H}_0]}{m^2\omega^2} + \sum_{n\neq 0,m} \frac{[\hat{H}_n, \hat{H}_{m-n}]}{2mn\omega^2} - \sum_{n\neq 0} \frac{[\hat{H}_n, \hat{H}_m]}{2mn\omega^2}. \tag{2.51}$$

The result for general t_0 is recovered by replacing $\hat{H}_m \to \hat{H}_m e^{-im\omega t_0}$, $\hat{\Lambda}_m \to \hat{\Lambda}_m e^{-im\omega t_0}$.

On the other hand, the dressed-particle Hamiltonian is obtained as a van Vleck

perturbation series, with [28, 36, 37]

$$\hat{F}^{(0)} = \hat{H}_0, \tag{2.52}$$

$$\hat{F}^{(1)} = \sum_{m\neq 0} \frac{[\hat{H}_{-m}, \hat{H}_m]}{2m\omega}, \tag{2.53}$$

$$\hat{F}^{(2)} = \sum_{m\neq 0} \frac{[[\hat{H}_{-m}, \hat{H}_0], \hat{H}_m]}{2m^2\omega^2} + \sum_{m\neq 0} \sum_{n\neq 0,m} \frac{[[\hat{H}_{-m}, \hat{H}_{m-n}], \hat{H}_n]}{3mn\omega^2}, \tag{2.54}$$

$$\begin{aligned}\hat{F}^{(3)} = &\sum_{m\neq 0} \frac{[[[\hat{H}_{-m}, \hat{H}_0], \hat{H}_0], \hat{H}_m]}{2m^3\omega^3} + \sum_{m\neq 0} \sum_{n\neq 0,m} \frac{[[[\hat{H}_{-m}, \hat{H}_0], \hat{H}_{m-n}], \hat{H}_n]}{3m^2n\omega^3} \\ &+ \sum_{m\neq 0} \sum_{n\neq 0,m} \frac{[[[\hat{H}_{-m}, \hat{H}_{m-n}], \hat{H}_0], \hat{H}_n]}{4mn^2\omega^3} - \sum_{m,n\neq 0} \frac{[[[\hat{H}_{-m}, \hat{H}_m], \hat{H}_{-n}], \hat{H}_n]}{12mn^2\omega^3} \\ &+ \sum_{m\neq 0} \sum_{n\neq 0,m} \frac{[[\hat{H}_{-m}, \hat{H}_0], [\hat{H}_{m-n}, \hat{H}_n]]}{12m^2n\omega^3} + \sum_{m,n\neq 0} \sum_{l\neq 0,m,n} \frac{[[[\hat{H}_{-m}, \hat{H}_{m-l}], \hat{H}_{l-n}], \hat{H}_n]}{6lmn\omega^3} \\ &+ \sum_{m,n\neq 0} \sum_{l\neq 0,m-n} \frac{[[[\hat{H}_{-m}, \hat{H}_{m-n-l}], \hat{H}_l], \hat{H}_n]}{24lmn\omega^3} + \sum_{m,n\neq 0} \sum_{l\neq 0,m,n} \frac{[[\hat{H}_{-m}, \hat{H}_{m-l}], [\hat{H}_{l-n}, \hat{H}_n]]}{24lmn\omega^3},\end{aligned} \tag{2.55}$$

and

$$i\hat{\Lambda}_0^{(n)} = 0, \tag{2.56}$$

$$i\hat{\Lambda}_{m\neq 0}^{(1)} = -\frac{\hat{H}_m}{2m\omega}, \tag{2.57}$$

$$i\hat{\Lambda}_{m\neq 0}^{(2)} = \sum_{n\neq 0,m} \frac{[\hat{H}_n, \hat{H}_{m-n}]}{2mn\omega^2} + \frac{[\hat{H}_m, \hat{H}_0]}{m^2\omega^2}, \tag{2.58}$$

$$\begin{aligned}i\hat{\Lambda}_{m\neq 0}^{(3)} = &-\frac{[[\hat{H}_m, \hat{H}_0], \hat{H}_0]}{m^3\omega^3} + \sum_{n\neq 0} \frac{[\hat{H}_m, [\hat{H}_{-n}, \hat{H}_n]]}{4m^2n\omega^3} \\ &- \sum_{n\neq 0,m} \frac{[[\hat{H}_n, \hat{H}_0], \hat{H}_{m-n}]}{2mn^2\omega^3} - \sum_{n\neq 0,m} \frac{[[\hat{H}_n, \hat{H}_{m-n}], \hat{H}_0]}{2m^2n\omega^3} \\ &- \sum_{n\neq 0} \sum_{l\neq 0,n,m} \frac{[[\hat{H}_n, \hat{H}_{l-n}], \hat{H}_{m-l}]}{4mnl\omega^3} - \sum_{n\neq 0} \sum_{l\neq 0,m-n} \frac{[\hat{H}_n, [\hat{H}_l, \hat{H}_{m-n-l}]]}{12mnl\omega^3}.\end{aligned} \tag{2.59}$$

Note that these expressions are invariant under $\hat{H}_m \to \hat{H}_m e^{-im\omega t_0}$, $\hat{\Lambda}_m \to \hat{\Lambda}_m e^{-im\omega t_0}$.

2.2 Statistical properties of periodically-driven systems

We have reviewed the various frameworks for calculating the quasienergy eigenstates, which are analogous to the energy eigenstates in static systems. Here we would like to reconfirm why we focus on the (quasi-)energy eigenstates. This is, in a context of dynamics, because energy eigenstates are special states where expectation values of observables do not change during a time evolution. Also, they provide the solution for the time-dependent Schrödinger equation. This reasoning is closely related to the observation given in the previous section.

On the other hand, the diagonalization of the Hamiltonian is also motivated by the equilibrium statistical mechanics, where the statistical expectation value in thermal equilibrium is calculated with an ensemble diagonal with respect to energy.

Then, should the statistical properties of the periodically-driven systems be described by an ensemble diagonal in quasienergy? This question is still open, although the answer is expected not to be as universal as that for the equilibrium states. However, thanks to recent studies, various characteristic features in the statistical properties of periodically-driven systems have been unveiled. In this section, we would like to review these recent progresses, and clarify the standpoint for this problem in the present thesis.

2.2.1 Ensemble diagonal in quasienergy

Statistical properties of nonequilibrium systems can be discussed with a time evolution of the ensemble, i.e., the density matrix. The quasienergy eigenstates, $\{|\psi_\alpha(t)\rangle\}_\alpha = \{|u_\alpha(t)\rangle e^{-i\epsilon_\alpha t}\}_\alpha$, span an orthonormal basis at any time t, since their snapshots are a set of the eigenstate of the Floquet-Magnus Hamiltonian. Thus the density matrix $\hat{\rho}(t)$ can be decomposed as

$$\hat{\rho}(t) = \sum_{\alpha\beta} \rho_{\alpha\beta} |u_\alpha(t)\rangle\langle u_\beta(t)| e^{-i(\epsilon_\alpha - \epsilon_\beta)t} \tag{2.60}$$

with time-independent coefficients $\rho_{\alpha\beta}$. The statistical expectation value of an observable $\hat{\mathcal{O}}$ is given as

$$\langle\hat{\mathcal{O}}(t)\rangle = \mathrm{Tr}[\hat{\mathcal{O}}\hat{\rho}(t)] = \sum_{\alpha\beta} \rho_{\alpha\beta} \langle u_\beta(t)|\hat{\mathcal{O}}|u_\alpha(t)\rangle e^{-i(\epsilon_\alpha - \epsilon_\beta)t}. \tag{2.61}$$

Thus, if we have an ensemble diagonal in quasienergy ($\rho_{\alpha\beta} = 0$ for $\alpha \neq \beta$), the density matrix is time-periodic, i.e., represents a steady state. Namely, if we as-

sume that a steady state is realized under a periodic driving, we can expect that off-diagonal components should be irrelevant.

While the quasienergy distribution $\rho_{\alpha\alpha}$ is unknown here, we would like to discuss how the temporal average of $\langle\hat{\mathcal{O}}(t)\rangle_\alpha \equiv \langle u_\alpha(t)|\hat{\mathcal{O}}|u_\alpha(t)\rangle$ should be calculated in each formalism. First, we consider $\langle\hat{\mathcal{O}}(t)\rangle_\alpha$ in the notation of the extended Hilbert space. The Fourier transformation yields

$$\langle\hat{\mathcal{O}}(t)\rangle_\alpha = \sum_{n=-\infty}^{\infty}\sum_{m=-\infty}^{\infty}\langle u_{\alpha,n}|\hat{\mathcal{O}}|u_{\alpha,m}\rangle e^{-i(m-n)\omega t}. \tag{2.62}$$

In the temporal average, the terms off-diagonal in Fourier index vanish. Thus in the extended Hilbert space, we should take an expectation value of a redefined operator

$$\hat{\mathcal{O}} \to \begin{pmatrix} \ddots & \ddots & \ddots & & \\ \ddots & \hat{\mathcal{O}} & 0 & 0 & \\ \ddots & 0 & \hat{\mathcal{O}} & 0 & \ddots \\ & 0 & 0 & \hat{\mathcal{O}} & \ddots \\ & & \ddots & \ddots & \ddots \end{pmatrix}. \tag{2.63}$$

On the other hand, for the Floquet-Magnus Hamiltonian, since the eigenstates are snapshots of the quasienergy eigenstates, $|\psi_\alpha(t_0)\rangle$, we have $\langle\hat{\mathcal{O}}(t_0)\rangle_\alpha$ if we calculate the expectation value for each eigenstate. At general time t, we can rewrite $\langle\hat{\mathcal{O}}(t)\rangle_\alpha$ as

$$\langle\hat{\mathcal{O}}(t)\rangle_\alpha = \langle\psi_\alpha(t_0)|e^{i\hat{\Lambda}(t,t_0)}\hat{\mathcal{O}}e^{-i\hat{\Lambda}(t,t_0)}|\psi_\alpha(t_0)\rangle, \tag{2.64}$$

so that we should redefine the operator as

$$\hat{\mathcal{O}} \to T^{-1}\int_0^T dt\, e^{i\hat{\Lambda}(t,t_0)}\hat{\mathcal{O}}e^{-i\hat{\Lambda}(t,t_0)} \tag{2.65}$$

for time-averaged expectation values. The case of the dressed particle can also be obtained just by replacing $\hat{\Lambda}(t,t_0)$ with $\hat{\Gamma}(t)$.

In the case of high-frequency driving, one can expand the unitary transformation in ω^{-1}, as

$$\hat{\mathcal{O}} \to \hat{\mathcal{O}} + [i\hat{\Lambda}_0^{(1)} + i\hat{\Lambda}_0^{(2)}, \hat{\mathcal{O}}] + \frac{1}{2}\sum_{m=-\infty}^{\infty}[i\hat{\Lambda}_m^{(1)}, [i\hat{\Lambda}_{-m}^{(1)}, \hat{\mathcal{O}}]] + \mathcal{O}(\omega^{-3}). \tag{2.66}$$

This clarifies that in the van Vleck expansion for dressed particles, the first-order term vanishes due to the boundary condition, so that the correction to $\hat{\mathcal{O}}$ is small in

the high-frequency regime.

Here we have introduced how the observables should be described in wave-function-based arguments. Another way to describe the non-equilibrium statistical properties is based on the Green function, namely the nonequilibrium Green function method [16, 23]. While the nonequilibrium Green function method describes the nonequilibrium ensemble evolving from the Gibbs ensemble in a nonempirical manner, with an assumption corresponding to a quasienergy-diagonal ensemble, i.e., the periodicity of the Green function, one can transform the nonequilibrium Green function to what is called the Floquet Green function [18, 23, 47, 48], which describes steady states of periodically-driven systems.

2.2.2 Eigenstate thermalization hypothesis

In the previous subsection, we have assumed that the ensemble for steady states is diagonal in quasienergy. In this subsection, we would like to mention how this assumption would be justified in isolated systems.

As Eq. (2.60) shows, the coefficients $\rho_{\alpha\beta}$ do not change in time evolution. Namely, if one has an initial state with off-diagonal coefficients, they will never vanish. This is also the case for static Hamiltonians; components off-diagonal in eigenenergy never vanish in time evolution. Nonetheless, it is known that expectation values under the time evolution via a static Hamiltonian will converge to thermal values, namely those described by the microcanonical ensemble. If we accept this statement, periodically-driven systems are expected to evolve to the microcanonical distribution of quasienergy, since the stroboscopic time evolution is equivalent to that via the static Floquet-Magnus Hamiltonian. Therefore, in this subsection we discuss this statement further.

This statement is closely related to the nonintegrability of the system, so that it does not hold for, e.g., non-interacting systems. The relaxation of the system toward thermal equilibrium can be intuitively understood by the argument of the typicality in nonintegrable systems [49]. Namely, for physical systems, almost all the states on the isoenergy surface should be typical, i.e., indistinguishable from the thermal equilibrium state. The typicality seems quite universal for physical systems, which is implied from the universality and accuracy of the equilibrium statistical mechanics; The microcanonical ensemble contains all the states on the isoenergy surface, including states far from equilibrium, with same weight. Namely, states realized after the time evolution in an isolated system should also be indistinguishable with thermal equilibrium states. This might seem contradicting the fact that $\rho_{\alpha\beta}$ never vanish, but the contribution from the off-diagonal components in macroscopic systems are in fact infinitesimally small in a long-time average [50, 51]. This justifies the as-

sumption of a diagonal ensemble, and the ensemble is in fact indistinguishable from the microcanonical ensemble if a hypothesis called the eigenstate thermalization hypothesis [52–55] holds; namely, the hypothesis that energy eigenstates themselves are already thermalized. Indeed, this hypothesis is believed to hold generically for nonintegrable systems.

2.2.3 Thermalization toward infinite temperature

If we assume that the eigenstate thermalization hypothesis holds, statistical properties of periodically-driven isolated system should be described by the microcanonical distribution of quasienergy. However, this in turn might contradict an intuitive expectation from thermodynamics. According to Planck's principle, which is equivalent to the second law of thermodynamics, the total work after an adiabatic cyclic operation must be nonnegative. The periodic driving of an isolated system is nothing but an adiabatic cyclic operation, so that it continuously provides thermodynamic work to the system.

Since Planck's principle is believed to hold generally for quantum-mechanical macroscopic systems as proved with generic assumptions [56, 57], we cannot expect ordinary thermalization for the periodically-driven system in the thermodynamic limit.

Indeed, the Floquet-Magnus Hamiltonian for nonintegrable systems has been known to take a form of a random matrix in the thermodynamic limit [38, 39]. There the eigenvectors are totally random, which implies the system is at infinite temperature[8].

2.2.4 Floquet prethermalization

This may seem to make engineering exotic phases using periodic driving hopeless if the thermodynamic limit is universally random and featureless. However, it has also been known that this does not immediately make the periodically-driven systems unmanageable, thanks to some loopholes.

For instance, one can make the final state nontrivial by employing the many-body localization [59–61], which is a disordered state known to be never thermalized without a heat bath in spite of the nonintegrability.

Another important possibility is a situation where the evolution toward infinite temperature is extremely slow, so that we can have a transient state with an extremely long lifetime. Indeed, it is the case if the driving frequency is high enough;

[8] In the context of thermal pure quantum states [58], infinite-temperature states are also generated as totally-random state vectors.

in such a situation, the heating rate of the system is exponentially slow $\sim e^{-\mathcal{O}(\omega)}$. This is rigorously proved for energetically bounded systems [40, 41], and up to $t \sim e^{\mathcal{O}(\omega)}$, the system is accurately described by the Floquet-Magnus Hamiltonian expanded in an asymptotic series in $1/\omega$ and truncated at an appropriate order. Namely, before reaching infinite temperature, the system is expected to show a thermalization with the microcanonical distribution of the truncated Floquet-Magnus Hamiltonian, which is sometimes called the Floquet prethermalization.

On the other hand, some examples imply the presence of other transient states with a long lifetime, referred to as nonthermal fixed points, in the quench dynamics with static Hamiltonian [23, 62]. Therefore, what kind of metastable states should be observed in realistic situations depends on details of the system, such as the relation between the lifetimes for the truncated Floquet-Magnus Hamiltonian and that for the nonthermal fixed point, and on the timing at which the system is observed, and how the initial state is prepared.

The microcanonical description with the truncated Floquet-Magnus Hamiltonian can also be degraded in continuous systems, since the mechanism of slow heating is essentially derived from the bounded energy spectrum. While the theoretical models defined on lattices are energetically bounded, originally they should be regarded as low-energy effective models downfolded from the (first-principle) solid-state Hamiltonian defined in a continuous space. Hence the slow heating should not occur unless the low-energy degrees of freedom are isolated well in the energy spectrum. At any rate, the lifetime should be characterized by the inverse transition amplitude for a level resonance, so that a similar long lifetime is expected to be realized in various situations, e.g., when the driving frequency is smaller than the energy gap.

2.2.5 Dissipative Floquet systems

Finally, we briefly mention heat baths. Unlike the canonical distribution in equilibrium systems, we cannot expect to have a universal description of open systems coupled to a heat bath.

First, the quasienergy itself cannot be ordered due to the indefiniteness on an integral multiple of the driving frequency, so that one cannot define the Boltzmann factor unless the indefiniteness is removed in some way.

Also, we have at least two kinds of effective Hamiltonians; the truncated Floquet-Magnus Hamiltonian in $1/\omega$ asymptotic series and a random matrix. Even if the system is described by the canonical distribution, which one should be adopted depends on the time scale for exchanging energy between the heat bath [63, 64]. A nonthermal distribution different from the canonical distribution can also be realized in some cases. Indeed, with the Floquet Green function method, a nonthermal distribution

in dissipative systems is reported [18, 23, 28, 65].

As we have seen in this section, statistical properties of the periodically-driven systems have a complicated structure compared with equilibrium systems, and depend on details of the problem. At any rate, we can expect some close relations between quasienergy and distributions, thus we shall focus on the quasienergy eigenstates in this thesis, especially their asymptotic form. We also consider the explicit time evolution of the system for discussing metastable states.

Chapter 3

Brillouin-Wigner formalism for Floquet topological phases

In this chapter, we discuss periodically-driven noninteracting systems, and their topological properties [28, 66]. After a brief review of the topologically nontrivial systems in condensed matter and their implementation for periodically-driven systems, we develop a framework suitable for understanding the topological phase transition occurring both in high- and low-frequency driving in a unified manner. This framework, based on the Brillouin-Wigner perturbation theory in elementary quantum mechanics [67–70], is proposed by the present author [28], and we apply this to the static Floquet Hamiltonian in the extended Hilbert space. We shall also discuss the application of this framework to the Floquet topological insulators and Floquet Weyl semimetals, and mathematical structures underlying these systems.

3.1 Introduction and motivation

3.1.1 Chern insulators

Topological properties play an essential role in condensed matter physics; they are crucial ingredients to characterize macroscopic phases such as quantum Hall insulators. One of the typical examples in which a topological number becomes a physically observable quantity can be found in the quantization of the Hall conductivity in two-dimensional solid-state systems. As the so-called TKNN formula [71] shows, the Hall conductivity σ_{xy} of noninteracting band insulators with the Fermi energy in a band

gap is expressed as

$$\sigma_{xy} = \frac{e^2}{h} \sum_{\alpha}^{\text{occ}} C_\alpha, \tag{3.1}$$

$$C_\alpha = \int_{\text{BZ}} \frac{d^2\boldsymbol{k}}{2\pi} \sum_{i,j=1,2} \epsilon_{ij} \frac{\partial}{\partial k_i} \left(-i \langle u_{\alpha \boldsymbol{k}} | \frac{\partial}{\partial k_j} | u_{\alpha \boldsymbol{k}} \rangle \right) \tag{3.2}$$

at zero temperature. Here $|u_{\alpha \boldsymbol{k}}\rangle$ is the Bloch wave function with a band index α and a crystal momentum $\boldsymbol{k} = (k_1, k_2)$, and ϵ_{ij} is the Levi-Civita symbol. The integral is taken over the first Brillouin zone. C_α is a topological invariant called the Chern number, which always takes an integer value.

Essential properties related to the Chern number are minimally captured in two-band systems,

$$\hat{H}(\boldsymbol{k}) = \boldsymbol{R}(\boldsymbol{k}) \cdot \hat{\boldsymbol{\sigma}} = \begin{pmatrix} R_3 & R_1 - iR_2 \\ R_1 + iR_2 & -R_3 \end{pmatrix}, \tag{3.3}$$

with $\hat{\boldsymbol{\sigma}}$ being the Pauli matrices. This Hamiltonian has two eigenvalues $\epsilon = \pm|\boldsymbol{R}(\boldsymbol{k})|$, so that it is insulating if $|\boldsymbol{R}(^\forall \boldsymbol{k})| \neq 0$. If we denote $\hat{\boldsymbol{R}}(\boldsymbol{k}) \equiv \boldsymbol{R}(\boldsymbol{k})/|\boldsymbol{R}(\boldsymbol{k})|$, the Chern number $C_\pm$ for upper (+) and lower (−) band can be reformulated as

$$C_\pm = \pm \int_{\text{BZ}} \frac{d^2\boldsymbol{k}}{4\pi} \hat{\boldsymbol{R}} \cdot \left(\frac{\partial \hat{\boldsymbol{R}}}{\partial k_1} \times \frac{\partial \hat{\boldsymbol{R}}}{\partial k_2} \right). \tag{3.4}$$

As the integrand measures a (signed) solid angle spanned by $\hat{\boldsymbol{R}}(\boldsymbol{k})$ as $\boldsymbol{k}$ is varied, the Chern number for two-level systems is nothing but the winding number, namely how many times $\hat{\boldsymbol{R}}(\boldsymbol{k})$ wraps the unit sphere when $\boldsymbol{k}$ is swept over the whole Brillouin zone. C cannot be changed unless one has a gap closing point $\boldsymbol{R} = 0$, hence robust against perturbations.

Since the conductivity is antisymmetric against time reversal, the Chern number must be zero in time-reversal symmetric systems. While the time-reversal symmetry is usually broken by applying a magnetic field as typified by the integer quantum Hall system for free electrons, Haldane showed that the Hall conductivity can be nonzero even in the absence of a net magnetic flux [72]. This is a crucial implication that the quantum Hall effect is essentially derived from the topological property, not necessarily from the magnetic field. Band insulators with a nonzero Hall conductivity is thus referred to as Chern insulators.

Let us briefly review the model proposed by Haldane. It is defined on a honeycomb

lattice with

$$\hat{H}(\boldsymbol{k}) = \sum_{l=0}^{2} \begin{pmatrix} 2t'\cos(\boldsymbol{k}\cdot\boldsymbol{b}_l + \phi) & -te^{-i\boldsymbol{k}\cdot\boldsymbol{e}_l} \\ -te^{i\boldsymbol{k}\cdot\boldsymbol{e}_l} & 2t'\cos(\boldsymbol{k}\cdot\boldsymbol{b}_l - \phi) \end{pmatrix} + \begin{pmatrix} M & 0 \\ 0 & -M \end{pmatrix}, \tag{3.5}$$

where $\boldsymbol{e}_l = (-\sin(2\pi l/3), \cos(2\pi l/3))$ and $\boldsymbol{b}_l = \boldsymbol{e}_{l+1} - \boldsymbol{e}_l$. Namely, the model is composed of a (real) nearest-neighbor hopping t, a complex next-nearest-neighbor hopping $t'e^{i\phi}$ with a phase ϕ, and a staggered potential M, as depicted in Fig. 3.1(a). The time-reversal symmetry is broken for a nonzero phase $\phi \neq 0$. We exemplify the texture of $\hat{\boldsymbol{R}}(\boldsymbol{k})$ defined in Eq. (3.3) for $t = 2t' = 1$, $\phi = \pi/2$, and $M = 0$ in Fig. 3.1(b), which clearly shows that the associated Chern number is 1, whereas for $\phi = 0$ and $M \neq 0$, the system is topologically trivial.

The topological transition in the Haldane model occurs at the Dirac points at $\boldsymbol{k} = \pm(4\pi/3\sqrt{3}, 0)$, which are respectively called K (+) and K' (−) and shown in Fig. 3.1(d). By linearizing Eq. (3.5) around these k-points, one obtains the two-dimensional Dirac Hamiltonian with a mass term,

$$\hat{H}(\boldsymbol{k}) = \begin{pmatrix} m & c(k_1 - ik_2) \\ c(k_1 + ik_2) & -m \end{pmatrix}, \tag{3.6}$$

with a parametrization $c = \pm 3t/2$ and $m = \mp M - 3\sqrt{3}t'\sin\phi$. While the linearized Hamiltonian is defined on an unbounded and nonperiodic momentum space, the Chern number calculated with Eq. (3.4) reads[1]

$$C_- = -\frac{1}{2}\operatorname{sgn} m. \tag{3.7}$$

A topological phase transition occurs at $m = 0$, at which the gap is closed and the massless Dirac cone appears in the dispersion relation. The Chern number for the whole system is given by the sum of the two contributions from K and K' points, so that the Chern number is nonzero if $|M| < 3\sqrt{3}|t'\sin\phi|$, as depicted in Fig. 3.1(c).

The fact that the topological number cannot change without a gap closing leads to a quite remarkable consequence peculiar to the topological systems when a boundary of the system is considered; the system has to close its energy gap at the edge of the system (an interface with a vacuum, which is topologically trivial) to change the topological number. Namely, for the Chern insulators, their bulk is insulating, but the edge has conducting states. Indeed, the gapless edge state carries a Hall current, and the bulk topological number determines how many gapless modes appear at

[1]Note that here the Chern number is quantized into half integers, since non-integer values are allowed in the absence of the periodicity in the momentum space.

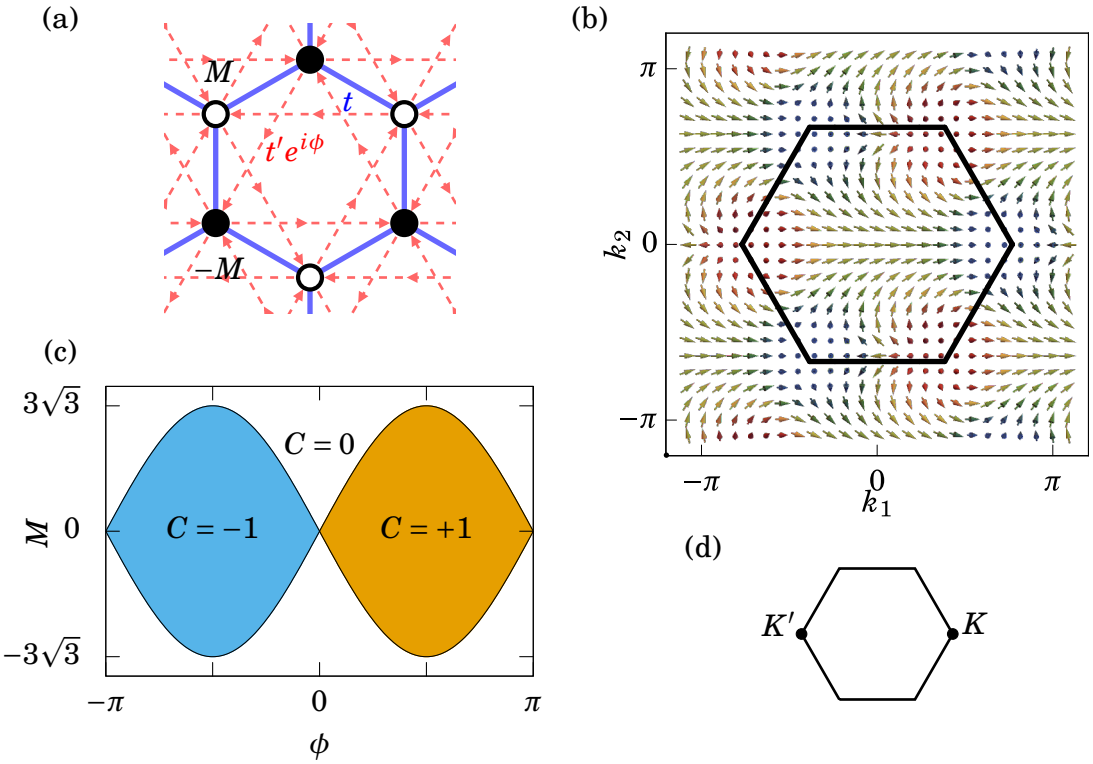

Figure 3.1: (a) The configuration of the Haldane model. Blue solid lines represent the hopping with an amplitude t, while red dashed lines hopping with $t'e^{i\phi}$ for the direction of arrows. The onsite potential M ($-M$) is applied on black (white) sites. (b) Texture of $\hat{\boldsymbol{R}}(\boldsymbol{k})$ for the Haldane model, here for $t = 2t' = 1$, $\phi = \pi/2$, $M = 0$. The first Brillouin zone is depicted with a black hexagon. The value of R_z is represented by the color of arrows, where red (blue) is assigned to $R_z = +1$ (-1). (c) The phase diagram of the Haldane model. (d) The positions of K and K' in the first Brillouin zone.

the boundary, which is called the "bulk-edge" correspondence [73]. This is clearly shown in Fig. 3.2(b); while the bulk dispersion calculated with the periodic boundary condition in Fig. 3.2(a) is gapped, a pair of gapless states appears in the dispersion when an edge as depicted in Fig. 3.2(c) is introduced.

3.1.2 Floquet topological insulators

As manifested by the Haldane model, the quantum Hall effect without the Landau levels is remarkable, but the model showing nonzero Chern numbers seems not so realistic as Haldane himself admits in his paper; the key ingredient, the complex hopping to break the time-reversal symmetry, is hard to realize in condensed matters.

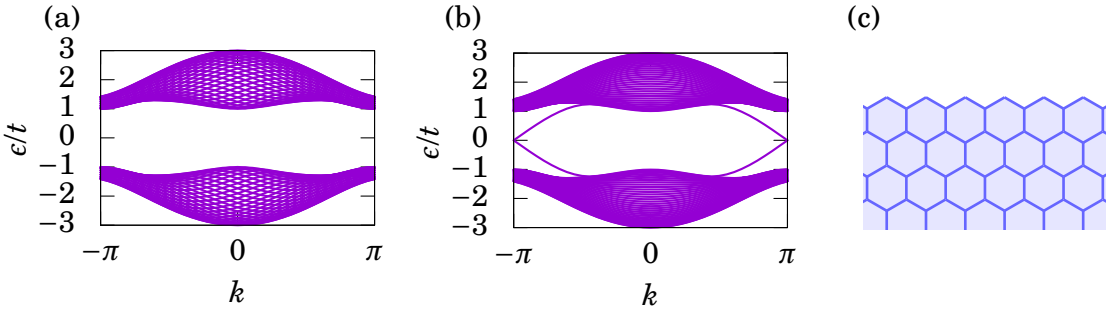

Figure 3.2: (a) The band dispersion of the Haldane model with parameters used in Fig. 3.1(c) and the periodic boundary condition. (b) The band dispersion with the edge depicted in (c). (c) A schematic picture of the zigzag edge introduced for (b).

One way to circumvent this difficulty is considering a spin analog of the quantum Hall insulator [74], the Z_2 insulator, which is feasible with a spin-orbit coupling, and indeed has been found experimentally [75, 76]. The mechanism for realizing the complex hopping as a mean-field Hamiltonian due to the spontaneous symmetry breaking is also conceived [77, 78], but has not been realized yet.

An entirely different pathway is turned out to lie in periodically-driven systems: By driving the system with circularly-polarized lasers, the time-reversal symmetry is explicitly broken, and the system can exhibit Hall responses. This was first pointed out by Oka and Aoki [32], in the study of irradiated graphene. This is now called the "Floquet topological insulator".

After that, their proposal has turned out to be indeed a realization of the Haldane model, in terms of the high-frequency expansion in the Floquet formalism [33]. The lowest-order correction to the time-averaged Hamiltonian,

$$\hat{H}^{(1)} = \sum_{n\neq 0} \frac{[\hat{H}_{-n}, \hat{H}_n]}{2n\omega}, \tag{3.8}$$

indeed gives the complex next-nearest-neighbor hopping. The Haldane model was finally realized experimentally in a cold-atom implementation of this model for the Floquet topological insulator [9].

The high-frequency expansion captures the topology of the system even for stronger intensities, and there topological-to-topological phase transitions (e.g., from $C = -1$ to $+1$, see inset of Fig. 3.3) are found [9, 28]. A systematic improvement of the high-frequency expansion reveals the presence of topological phases with higher Chern numbers (e.g., from $C = +1$ to $C = -2$, see inset of Fig. 3.3), which are absent in the high-frequency limit [28].

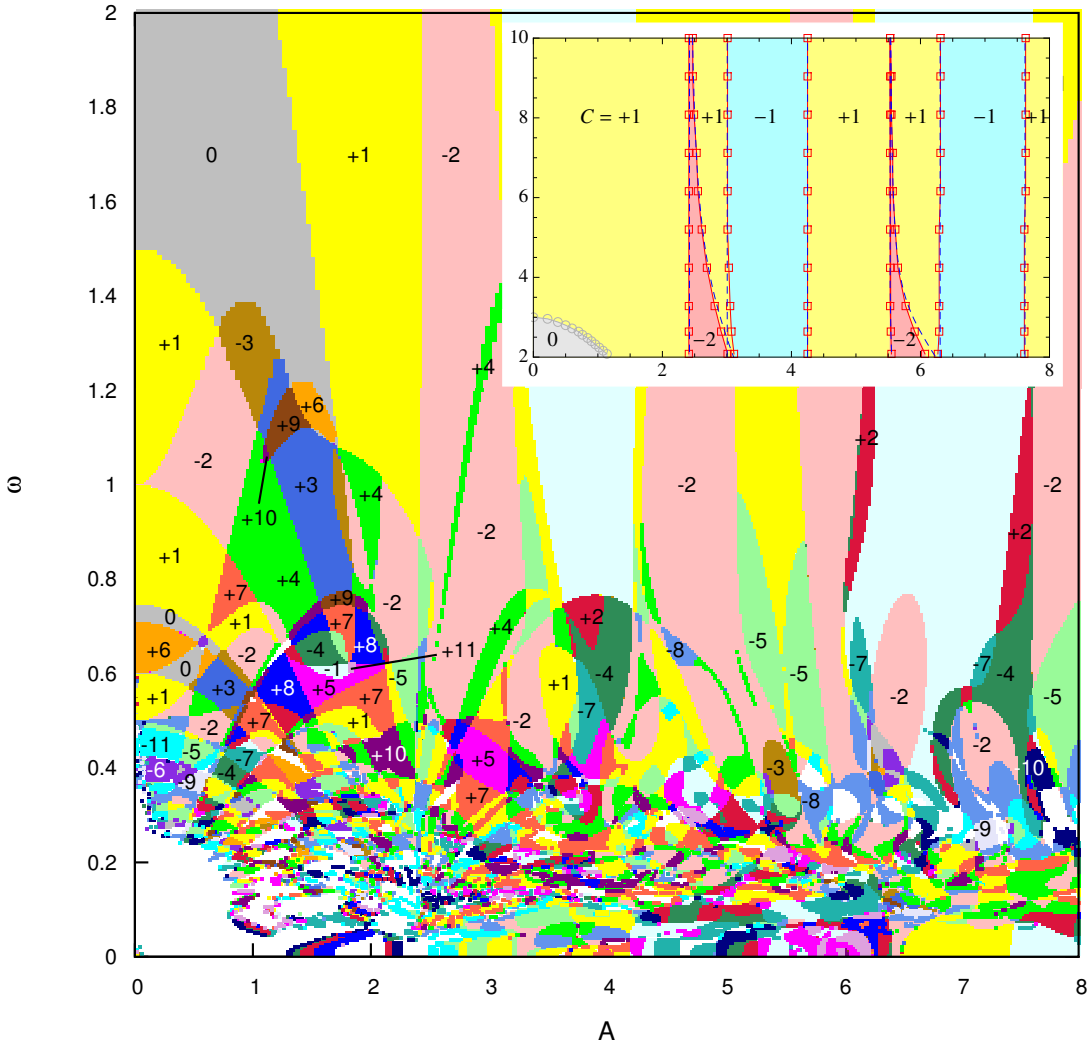

Figure 3.3: Topological phase diagram for the honeycomb lattice system driven by a circularly-polarized laser, against the driving amplitude A and frequency ω. The numbers in the phase diagram are the Chern number for the lower band in the Floquet Brillouin zone $(-\omega/2, \omega/2]$. Inset: the phase diagram in a higher frequency regime. After Ref. [28].

On the other hand, the topological structure appearing in the low-frequency regime has been also investigated numerically [28, 79, 80]. As Ref. [32] has already shown, the topological gaps open not only at the Dirac points but also in the Floquet sidebands, due to the avoided level crossing. These sideband effects make the topological phase diagram rather complicated, which has not been captured in the high-frequency expansion. This structure is partially investigated analytically by Kundu, *et al.* [79], and Perez-Piskunow, *et al.* [80], using (an analog of) $\boldsymbol{k}\cdot\boldsymbol{p}$ theory and the projected Green function method, respectively. These behaviors are summarized in the topological phase diagram for the honeycomb lattice shown in Fig. 3.3, which is taken from Ref. [28].

3.1.3 Weyl semimetals

The Weyl semimetal is another type of condensed-matter systems where topological properties play a crucial role [81–84]. While the Weyl semimetal is realized in three-dimensional systems, its physics can be interpreted in terms of Chern insulators in two dimension. The low-energy Hamiltonian for Weyl semimetals is expressed as

$$\hat{H}_{\mathrm{Weyl}}(\boldsymbol{k}) = c\Gamma\boldsymbol{k}\cdot\hat{\boldsymbol{\sigma}} = c\Gamma\begin{pmatrix} k_3 & k_1 - ik_2 \\ k_1 + ik_2 & -k_3 \end{pmatrix}, \tag{3.9}$$

where c is the Fermi velocity, $\Gamma = \pm 1$ is the chirality and $\boldsymbol{k} = (k_1, k_2, k_3)$ is a three-dimensional wave number. This Hamiltonian has a gapless (degenerated) point at $\boldsymbol{k} = (0,0,0)$, which is called the Weyl node. The Weyl node is robust against perturbations, since, even if one adds, e.g., a term $M\hat{\sigma}_3$, to this Hamiltonian, it just shifts the location of the Weyl node to $\boldsymbol{k} = (0,0,-\Gamma M/c)$. In lattice systems, Weyl nodes appear in pairs with opposite chiralities, due to the Nielsen-Ninomiya theorem [85]. If the pair of Weyl nodes is located at the same k-point, it is called the Dirac semimetal. The degenerate Weyl nodes can be separated in momentum space if the time-reversal symmetry is broken.

The Weyl semimetals with separated Weyl nodes have anomalous surface states, called the surface Fermi arc [82]. The presence of the Fermi arc can be deduced from the physics of the Chern insulators. Let $\boldsymbol{k}^{(\pm)}$ be respective locations of the Weyl nodes with the chirality ± 1 and $k_3^{(+)} < k_3^{(-)}$. If one regards k_3 as a parameter, one can view Eq. (3.9) as a two-dimensional system represented in the form of Eq. (3.6) with $m = \pm c(k_3 - k_3^{(\pm)})$. Then we can consider a Chern number as a function of k_3, which has a nontrivial value $C(k_3) = 1$ only for $k_3^{(+)} < k_3 < k_3^{(-)}$. Namely, if one introduces a boundary along the k_2k_3-plane, the dispersion along k_1 has gapless states only in this region. This clarifies the presence of the surface Fermi arc at the Fermi level,

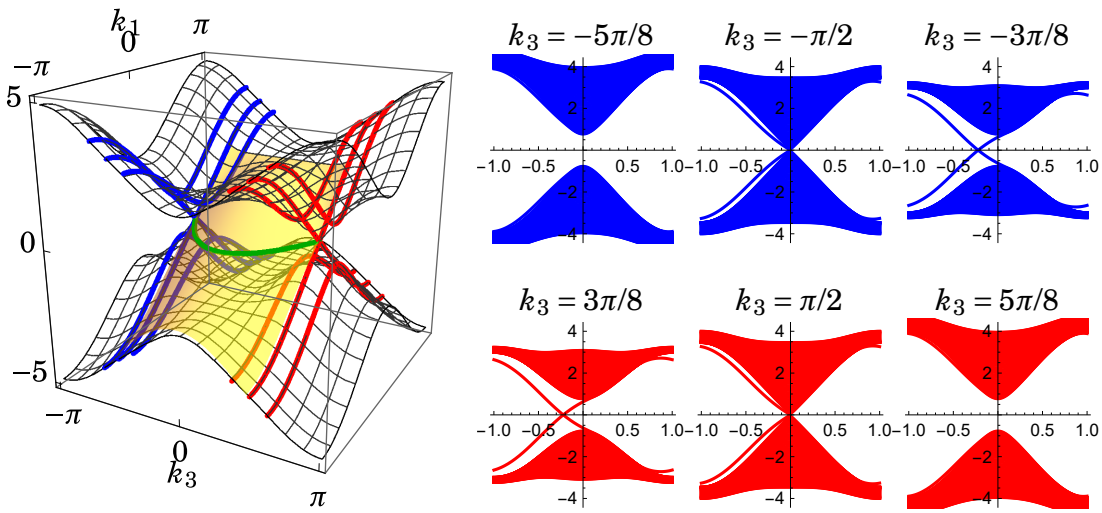

Figure 3.4: Illustration of the topological surface Fermi arc in Weyl semimetals. Left: The energy spectrum of a typical Weyl seimimetal [95] against (k_1, k_3). The Weyl nodes locate at $(k_1, k_3) = (0, \pm\pi/2)$ here. Above and below the curved surfaces (drawn by black lines) correspond to the bulk states. Blue and red lines are slices at $k_3 = \pm 3\pi/8,\ \pm\pi/2,\ \pm 5\pi/8$. A yellow surface depicts one of the surface states appearing with an open boundary condition along the k_2-direction. A green curve indicates the surface Fermi arc. Right: Energy spectra against k_1/π on the slices at $k_3 = \pm 3\pi/8,\ \pm\pi/2,\ \pm 5\pi/8$, with the open boundary condition. As the Chern number (for fixed k_3) changes at $k_3 = \pm\pi/2$, the nonzero Chern number and accompanying chiral edge states appear in $|k_3| < \pi/2$, which give the surface state and the Fermi arc shown in the left panel.

which connects the projected Weyl nodes, as shown in Fig. 3.4. As we see here, the Weyl nodes act as a monopole for the Berry flux, where, we define the monopole charge as the change of the Chern number for the lower band as k_3 is increased.

The Weyl semimetal exhibits characteristic electromagnetic responses due to the nontrivial topology, such as the negative magnetoresistance [86, 87], chiral magnetic effect [88, 89], and anomalous Hall effect.

Because of the resemblance to Chern insulators, the periodic driving can be a source of the Weyl semimetals [90–94]. By illuminating three-dimensional Dirac semimetal by a circularly-polarized laser propagating along the z-axis, an additional term $-(A^2/\omega)\hat{\sigma}_3$ appears in the high-frequency expansion of the Dirac Hamiltonian, so that the degenerated Weyl nodes shift to opposite directions.

3.1.4 Motivation of this chapter

As we have briefly reviewed, periodically-driven systems provide a rich source of topological phases of matter. While a basic aspect is captured by the high-frequency expansion, more complicated structures lying for low-frequency driving have not been understood in such a perturbative expansion. This has motivated us to construct a framework to understand the entire topological structure in the periodically-driven systems with a unified picture here.

We shall find that the Brillouin-Wigner perturbation theory is suitable for this purpose, so that we apply this to the effective static Hamiltonian defined in the extended Hilbert space. First, we develop the Brillouin-Wigner high-frequency expansion applicable to general periodically-driven systems. The Brillouin-Wigner expansion is a systematic procedure to project out irrelevant subspaces, so that we can derive the high-frequency expansion by extracting the zero-photon sector. We shall compare this expansion with those in the existing Floquet-Magnus and van Vleck schemes, and clarify the following features:

1. The expansion is composed of simple operator products $\hat{H}_m\hat{H}_n\ldots$, unlike the other expansions expressed with nested commutators. This significantly reduces the number of terms appearing in the expansion, and makes the theoretical framework much more transparent.

2. The higher-order terms are generated with a simple recurrence equation.

3. As a drawback against these advantages, the effective Hamiltonian can be non-hermitian. This may at first seem unphysical, but it is just due to a nonorthogonal basis. While the imaginary part of the quasienergy should be zero, it may emerge as a truncation error.

Since the Brillouin-Wigner method is advantageous in deriving higher-order terms, one can partially sum up the infinite series. This clarifies that the perturbative expansion tends to produce discontinuous dispersion relations, which leads to a finite radius of convergence and a failure of capturing the topological phase transition in the low-frequency regime.

On the other hand, the Brillouin-Wigner framework can be applicable not only for the projection on the zero-photon sector, but also for an arbitrary projection. Hence, by choosing an appropriate projection, one can describe the topological phase transition outside the radius of convergence for the high-frequency expansion. We shall apply these observations to the two- and three-dimensional Dirac systems in the continuous limit, and clarify their topological structures. We also discuss lattice-specific effects caused by putting them on lattice systems.

3.2 Brillouin-Wigner theory for Floquet systems

3.2.1 General framework

The Brillouin-Wigner theory [28, 67–70], the central ingredient in this chapter, is a general perturbative method to reduce the dimension of a Hilbert space. We call the reduced Hilbert space as a model space, and focus on the projection of the energy eigenstates onto the model space in this formalism. Here we denote the eigenstate of a Hamiltonian $\hat{H}$ as $|\phi\rangle$, i.e.,

$$\hat{H}|\phi\rangle = \epsilon|\phi\rangle, \tag{3.10}$$

with ϵ being the eigenenergy.

In the framework of the Brillouin-Wigner theory, a map, called the wave operator $\hat{\Omega}$, from the projected eigenstates $\hat{P}|\phi\rangle$ to the original ones $|\phi\rangle$ plays a key role. Namely, $\hat{\Omega}$ satisfies

$$\hat{\Omega}\hat{P}|\phi\rangle = |\phi\rangle. \tag{3.11}$$

With this, one can define an effective Hamiltonian $\hat{H}_{\mathrm{BW}}$ as

$$\hat{H}_{\mathrm{BW}} = \hat{P}\hat{H}\hat{\Omega}\hat{P}, \tag{3.12}$$

which is defined on the model space and satisfies

$$\hat{H}_{\mathrm{BW}}\hat{P}|\phi\rangle = \epsilon\hat{P}|\phi\rangle. \tag{3.13}$$

Namely, if one can construct the wave operator $\hat{\Omega}$ systematically, one can derive a Hamiltonian in the reduced Hilbert space that has the same energy spectrum and projected eigenstates.

As we shall see in the following subsections with an application to the Floquet systems, one can construct the wave operator by deforming the Schrödinger equation. The constructed wave operator, however, explicitly depends on eigenenergy ϵ. Namely, ϵ has to be determined in a self-consistent manner, and Eq. (3.11) is applicable only for the single eigenstate (with eigenvalue ϵ). Thus here we refer to the formalism with this wave operator as the single-root formalism. We can also formulate the multi-root formalism, by eliminating the ϵ-dependence by using Eq. (3.13) recursively.

3.2.2 Application to Floquet systems

Now we develop the systematic construction of the wave operator, with the application to periodically-driven systems. In this section, we denote the Floquet Hamilto-

nian in the extended Hilbert space as $(\hat{\mathscr{H}}-\hat{\mathscr{M}}\omega)$, with the Fourier indices suppressed. Namely, if we write the Fourier indices explicitly, it is written with operators in the original Hilbert space as

$$[\hat{\mathscr{H}}-\hat{\mathscr{M}}\omega]_{m,n} = \hat{H}_{m,n} - \delta_{m,n} m\omega. \tag{3.14}$$

Here, $\hat{H}_{m,n} = \hat{H}_{m-n}$ is the $(m-n)$-th component of the time-periodic Hamiltonian $\hat{H}(t)$. We also denote the time-periodic part of the quasienergy eigenstate labeled by α, $\{|u_{\alpha,m}\rangle\}_{m=-\infty}^{\infty}$, as a vector in the extended Hilbert space, $|\boldsymbol{u}_\alpha\rangle$. Namely, the eigenvalue equation (2.20) is rewritten as

$$(\hat{\mathscr{H}}-\hat{\mathscr{M}}\omega)|\boldsymbol{u}_\alpha\rangle = \epsilon_\alpha|\boldsymbol{u}_\alpha\rangle. \tag{3.15}$$

By denoting the projection operator to the model space as $\hat{\mathscr{P}}$ and the wave operator as $\hat{\Omega}$, we obtain the wave operator $\hat{\Omega}$ and the Brillouin-Wigner effective Hamiltonian $\hat{\mathscr{F}}_{\mathrm{BW}}$ as

$$\hat{\Omega}\hat{\mathscr{P}}|\boldsymbol{u}_\alpha\rangle = |\boldsymbol{u}_\alpha\rangle, \tag{3.16}$$

$$\hat{\mathscr{F}}_{\mathrm{BW}} = \hat{\mathscr{P}}(\hat{\mathscr{H}}-\hat{\mathscr{M}}\omega)\hat{\Omega}\hat{\mathscr{P}}. \tag{3.17}$$

In general, there is no restriction on the choice of the model space $\hat{\mathscr{P}}$ for the Brillouin-Wigner framework. For our purpose, we choose the model space diagonal in the photon number, i.e., $[\hat{\mathscr{P}}]_{m,n} \propto \delta_{m,n}$. One of the natural choices under this restriction is the zero-photon projection[2], $[\hat{\mathscr{P}}]_{m,n} = \delta_{m,n}\delta_{m,0}$. We adopt this projection below, while we shall also introduce another type of projection in a later section.

3.2.3 Single-root formalism

As the wave operator $\hat{\Omega}$ is a map from a restricted Hilbert space to a larger one, it is not fullrank. Thus Eq. (3.16) cannot be satisfied for all eigenstates. In this subsection let us consider a wave operator $\hat{\Omega}_\alpha$, for a given single eigenstate $|\boldsymbol{u}_\alpha\rangle$, which we call here a single-root wave operator.

The single-root wave operator can be formally derived from the eigenvalue equation Eq. (3.15): If we denote projection on the complementary space as $[\hat{\mathscr{Q}}]_{m,n} = \delta_{m,n} - [\hat{\mathscr{P}}]_{m,n}$, we can apply this to Eq. (3.15) to have

$$\hat{\mathscr{Q}}|\boldsymbol{u}_\alpha\rangle = \frac{\hat{\mathscr{Q}}}{\epsilon_\alpha + \hat{\mathscr{M}}\omega}\hat{\mathscr{H}}|\boldsymbol{u}_\alpha\rangle, \tag{3.18}$$

[2]One can also choose the n-photon projection, but it gives an equivalent mapping due to the redundancy in the eigenstates.

where we have defined

$$\left[\frac{\hat{\mathscr{Q}}}{\epsilon_\alpha + \hat{\mathscr{M}}\omega}\right]_{m,n} = \begin{cases} 0 & (m=0) \\ \dfrac{\delta_{m,n}}{\epsilon_\alpha + m\omega} & (\text{otherwise}) \end{cases}. \tag{3.19}$$

In general $(\epsilon_\alpha + \hat{\mathscr{M}}\omega)$ is not necessarily invertible, but if we fix the indefiniteness of the quasienergy as satisfying $\epsilon_\alpha \in [-\omega/2, \omega/2)$, it is invertible in the complementary space $\hat{\mathscr{Q}}$.

Then we can express $|\boldsymbol{u}_\alpha\rangle$ as

$$|\boldsymbol{u}_\alpha\rangle = \hat{\mathscr{P}}|\boldsymbol{u}_\alpha\rangle + \frac{\hat{\mathscr{Q}}}{\epsilon_\alpha + \hat{\mathscr{M}}\omega}\hat{\mathscr{H}}|\boldsymbol{u}_\alpha\rangle. \tag{3.20}$$

By iteratively substituting the right-hand side, we obtain

$$|\boldsymbol{u}_\alpha\rangle = \hat{\mathscr{P}}|\boldsymbol{u}_\alpha\rangle + \frac{\hat{\mathscr{Q}}}{\epsilon_\alpha + \hat{\mathscr{M}}\omega}\hat{\mathscr{H}}\hat{\mathscr{P}}|\boldsymbol{u}_\alpha\rangle + \frac{\hat{\mathscr{Q}}}{\epsilon_\alpha + \hat{\mathscr{M}}\omega}\hat{\mathscr{H}}\frac{\hat{\mathscr{Q}}}{\epsilon_\alpha + \hat{\mathscr{M}}\omega}\hat{\mathscr{H}}\hat{\mathscr{P}}|\boldsymbol{u}_\alpha\rangle + \dots \tag{3.21}$$

$$= \left(1 - \frac{\hat{\mathscr{Q}}}{\epsilon_\alpha + \hat{\mathscr{M}}\omega}\hat{\mathscr{H}}\right)^{-1}\hat{\mathscr{P}}|\boldsymbol{u}_\alpha\rangle, \tag{3.22}$$

namely, this equation implies that the single-root wave operator is expressed as

$$\hat{\Omega}_\alpha = \left(1 - \frac{\hat{\mathscr{Q}}}{\epsilon_\alpha + \hat{\mathscr{M}}\omega}\hat{\mathscr{H}}\right)^{-1}\hat{\mathscr{P}}, \tag{3.23}$$

$$[\hat{\Omega}_\alpha]_{m_1,0} = \delta_{m_1,0} + (1-\delta_{m_1,0})\sum_{n=1}^{\infty}\sum_{m_2,\dots,m_n\neq 0}\frac{(\prod_{j=1}^{n-1}\hat{H}_{m_j,m_{j+1}})\hat{H}_{m_n,0}}{\prod_{j=1}^{n}(\epsilon_\alpha + m_j\omega)}. \tag{3.24}$$

Since we have not imposed any assumption on the eigenstate $|\boldsymbol{u}_\alpha\rangle$, one can use the same expression Eq. (3.23) for all the eigenstates, but it explicitly depends on the quasienergy ϵ_α, thus $\hat{\Omega}_\alpha$'s are different operators for different eigenstates (α).

One can express the Brillouin-Wigner Hamiltonian as a function of ϵ_α,

$$\hat{\mathscr{F}}_{\mathrm{BW}}(\epsilon_\alpha) = \hat{\mathscr{P}}\hat{\mathscr{H}}\left(1 - \frac{\hat{\mathscr{Q}}}{\epsilon_\alpha + \hat{\mathscr{M}}\omega}\hat{\mathscr{H}}\right)^{-1}\hat{\mathscr{P}} \tag{3.25}$$

$$= \hat{\mathscr{P}}\hat{\mathscr{H}}\hat{\mathscr{P}} + \hat{\mathscr{P}}\hat{\mathscr{H}}\frac{\hat{\mathscr{Q}}}{\epsilon_\alpha + \hat{\mathscr{M}}\omega}\hat{\mathscr{H}}\hat{\mathscr{P}} + \hat{\mathscr{P}}\hat{\mathscr{H}}\frac{\hat{\mathscr{Q}}}{\epsilon_\alpha + \hat{\mathscr{M}}\omega}\hat{\mathscr{H}}\frac{\hat{\mathscr{Q}}}{\epsilon_\alpha + \hat{\mathscr{M}}\omega}\hat{\mathscr{H}}\hat{\mathscr{P}} + \dots, \tag{3.26}$$

$$\hat{F}_{\mathrm{BW}}(\epsilon_\alpha) = [\hat{\mathscr{F}}_{\mathrm{BW}}(\epsilon_\alpha)]_{0,0} = \hat{H}_{0,0} + \sum_{n=1}^{\infty}\sum_{m_1,\dots,m_n\neq 0}\frac{\hat{H}_{0,m_1}(\prod_{j=1}^{n-1}\hat{H}_{m_j,m_{j+1}})\hat{H}_{m_n,0}}{\prod_{j=1}^{n}(\epsilon_\alpha + m_j\omega)}. \tag{3.27}$$

Since these operators depend on their eigenvalue, the eigenvalue equation has to be solved self-consistently. This structure enables the effective Hamiltonian to host a larger number of eigenstates than its dimension.

3.2.4 Multi-root formalism

So far, we have formulated the single-root formalism, in which the wave operator only maps a given single eigenvector. Here we consider the multi-root wave operator $\hat{\Omega}$, which maps rank$\hat{\Omega}$ eigenstates simultaneously. The key idea is that one can replace ϵ_α with an operator via

$$\hat{\mathscr{P}}\hat{\mathscr{H}}\hat{\Omega}_\alpha\hat{\mathscr{P}}|\boldsymbol{u}_\alpha\rangle = \epsilon_\alpha\hat{\mathscr{P}}|\boldsymbol{u}_\alpha\rangle, \tag{3.28}$$

thus one can expect to derive a self-consistent equation for $\hat{\Omega}_\alpha$ without explicit dependence on ϵ_α. To this end, first let us deform Eq. (3.23) into

$$\hat{\Omega}_\alpha = \hat{\mathscr{P}} + \frac{\hat{\mathscr{Q}}}{\hat{\mathscr{M}}\omega}\hat{\mathscr{H}}\hat{\Omega}_\alpha - \frac{\hat{\mathscr{Q}}}{\hat{\mathscr{M}}\omega}\hat{\Omega}_\alpha\epsilon_\alpha. \tag{3.29}$$

Then we can define the multi-root wave operator as a solution of the self-consistency equation,

$$\hat{\Omega} = \hat{\mathscr{P}} + \frac{\hat{\mathscr{Q}}}{\hat{\mathscr{M}}\omega}\hat{\mathscr{H}}\hat{\Omega} - \frac{\hat{\mathscr{Q}}}{\hat{\mathscr{M}}\omega}\hat{\Omega}\hat{\mathscr{P}}\hat{\mathscr{H}}\hat{\Omega}. \tag{3.30}$$

The solution of this equation is indeed the wave operator: If one diagonalizes the corresponding Brillouin-Wigner Hamiltonian as

$$\hat{\mathscr{P}}\hat{\mathscr{H}}\hat{\Omega}|v_\alpha\rangle = \epsilon_\alpha|v_\alpha\rangle, \tag{3.31}$$

Eq. (3.30) applied on $|v_\alpha\rangle$ reads

$$(\hat{\mathscr{H}} - \hat{\mathscr{M}}\omega)\hat{\Omega}|v_\alpha\rangle = \epsilon_\alpha\hat{\Omega}|v_\alpha\rangle, \tag{3.32}$$

namely $\hat{\Omega}|v_\alpha\rangle$ is the original eigenstate.

We should remark on the potential nonhermiticity in the Brillouin-Wigner Hamiltonian. Since $\hat{\Omega}|v_\alpha\rangle$'s constitute an orthogonal basis[3], one can rewrite $\hat{\mathscr{F}}_{\mathrm{BW}}$ as

$$\hat{\mathscr{F}}_{\mathrm{BW}} = \sum_\alpha \epsilon_\alpha \frac{|v_\alpha\rangle\langle v_\alpha|}{\langle v_\alpha|\hat{\Omega}^\dagger\hat{\Omega}|v_\alpha\rangle}\hat{\Omega}^\dagger\hat{\Omega}. \tag{3.33}$$

Namely, the Brillouin-Wigner Hamiltonian is in general not hermitian ($\hat{\mathscr{F}}_{\mathrm{BW}}^\dagger \neq \hat{\mathscr{F}}_{\mathrm{BW}}$)

[3]Here we choose $|v_\alpha\rangle$'s as unit vectors. Then $\hat{\Omega}|v_\alpha\rangle$'s are the original eigenstates, but their norm is not necessarily unity.

unless $[|v_\alpha\rangle\langle v_\alpha|, \hat{\Omega}^\dagger\hat{\Omega}] = 0$, although its eigenvalues are real. This is a manifestation of the fact that, while the original eigenstates are orthogonal with each other, their projections are not necessarily so[4]. We note that, by contrast, the single-root Hamiltonian Eq. (3.25) is hermitian.

As we have noted, since $\dim\hat{\mathscr{F}}_{\mathrm{BW}} = \mathrm{rank}\hat{\Omega} < \dim\hat{\mathscr{H}}$, the multi-root wave operator cannot satisfy Eq. (3.16) for all the eigenstates of the original Hamiltonian simultaneously. This implies that the solution of Eq. (3.30) is not unique; all the combinations of a set of $\dim\hat{\mathscr{F}}_{\mathrm{BW}}$ eigenstates can satisfy Eq. (3.30). However, since the eigenstates are redundant due to the indefiniteness, the number of the inequivalent eigenstates is exactly $\dim\hat{\mathscr{F}}_{\mathrm{BW}}$, and the solution must be unique if one imposes, for instance, $\epsilon_\alpha \in [-\omega/2, \omega/2)$ (called the first Floquet Brillouin zone).

3.2.5 High-frequency expansion

We have derived the self-consistent equation for the multi-root wave operator Eq. (3.30), and discuss the uniqueness of the solution in the first Floquet Brillouin zone. In this section we discuss an explicit solution for this equation in a form of $1/\omega$ series.

By comparing the both sides of Eq. (3.30) order by order in $1/\omega$, we obtain a recurrence equation

$$\hat{\Omega} = \sum_{n=0}^{\infty} \hat{\Omega}^{(n)}, \quad \hat{\Omega}^{(0)} = \hat{\mathscr{P}}, \quad \hat{\Omega}^{(1)} = \frac{\hat{\mathscr{Q}}}{\hat{\mathscr{M}}\omega}\hat{\mathscr{H}}\hat{\mathscr{P}},$$
$$\hat{\Omega}^{(n+1)} = \frac{\hat{\mathscr{Q}}}{\hat{\mathscr{M}}\omega}\hat{\mathscr{H}}\hat{\Omega}^{(n)} - \sum_{m=1}^{n} \frac{\hat{\mathscr{Q}}}{\hat{\mathscr{M}}\omega}\hat{\Omega}^{(m)}\hat{\mathscr{P}}\hat{\mathscr{H}}\hat{\Omega}^{(n-m)} (n \geq 1). \tag{3.34}$$

[4]Indeed, $[|v_\alpha\rangle\langle v_\alpha|, \hat{\Omega}^\dagger\hat{\Omega}] = 0$ is equivalent to $\langle v_\alpha|v_\beta\rangle = \delta_{\alpha\beta}$ and $\sum_\alpha |v_\alpha\rangle\langle v_\alpha| = \hat{\mathscr{P}}$.

Here, we should notice that the wave operator is determined uniquely as a $1/\omega$ series. Then we can write down an explicit formula,

$$\hat{\Omega}^{(0)}_{m_1,0} = \delta_{m_1,0}, \quad \hat{\Omega}^{(1)}_{m_1\neq 0,0} = \frac{\hat{H}_{m_1,0}}{m_1\omega}, \quad \hat{\Omega}^{(2)}_{m_1\neq 0,0} = \sum_{m_2\neq 0} \frac{\hat{H}_{m_1,m_2}\hat{H}_{m_2,0}}{m_1 m_2 \omega^2} - \frac{\hat{H}_{m_1,0}\hat{H}_{0,0}}{m_1^2\omega^2},$$

$$\begin{aligned}\hat{\Omega}^{(3)}_{m_1\neq 0,0} = &\sum_{m_2,m_3\neq 0} \frac{\hat{H}_{m_1,m_2}\hat{H}_{m_2,m_3}\hat{H}_{m_3,0}}{m_1 m_2 m_3 \omega^3} - \sum_{m_2\neq 0} \frac{\hat{H}_{m_1,m_2}\hat{H}_{m_2,0}\hat{H}_{0,0}}{m_1 m_2 \omega^3}\left(\frac{1}{m_1}+\frac{1}{m_2}\right) \\ &- \sum_{m_2\neq 0} \frac{\hat{H}_{m_1,0}\hat{H}_{0,m_2}\hat{H}_{m_2,0}}{m_1^2 m_2 \omega^3} + \frac{\hat{H}_{m_1,0}\hat{H}_{0,0}\hat{H}_{0,0}}{m_1^3\omega^3},\end{aligned}$$

$$\begin{aligned}\hat{\Omega}^{(4)}_{m_1\neq 0,0} = \sum_{\{m_{j\neq 1}\}\neq 0} \Bigg[&\frac{\hat{H}_{m_1,m_2}\hat{H}_{m_2,m_3}\hat{H}_{m_3,m_4}\hat{H}_{m_4,0}}{m_1 m_2 m_3 m_4 \omega^4} \\ &- \frac{\hat{H}_{m_1,m_2}\hat{H}_{m_2,m_3}\hat{H}_{m_3,0}\hat{H}_{0,0}}{m_1 m_2 m_3 \omega^4}\left(\frac{1}{m_1}+\frac{1}{m_2}+\frac{1}{m_3}\right) \\ &- \frac{\hat{H}_{m_1,m_2}\hat{H}_{m_2,0}\hat{H}_{0,m_3}\hat{H}_{m_3,0}}{m_1 m_2 m_3 \omega^4}\left(\frac{1}{m_1}+\frac{1}{m_2}\right) \\ &+ \frac{\hat{H}_{m_1,m_2}\hat{H}_{m_2,0}\hat{H}_{0,0}\hat{H}_{0,0}}{m_1 m_2 \omega^4}\left(\frac{1}{m_1^2}+\frac{1}{m_1 m_2}+\frac{1}{m_2^2}\right) \\ &- \frac{\hat{H}_{m_1,0}\hat{H}_{0,m_2}\hat{H}_{m_2,m_3}\hat{H}_{m_3,0}}{m_1^2 m_2 m_3 \omega^4} + \frac{\hat{H}_{m_1,0}\hat{H}_{0,m_2}\hat{H}_{m_2,0}\hat{H}_{0,0}}{m_1^2 m_2 \omega^4}\left(\frac{1}{m_1}+\frac{1}{m_2}\right) \\ &+ \frac{\hat{H}_{m_1,0}\hat{H}_{0,0}\hat{H}_{0,m_2}\hat{H}_{m_2,0}}{m_1^3 m_2 \omega^4} - \frac{\hat{H}_{m_1,0}\hat{H}_{0,0}\hat{H}_{0,0}\hat{H}_{0,0}}{m_1^4\omega^4}\Bigg],\end{aligned} \tag{3.35}$$

$$
\begin{aligned}
\hat{F}_{\mathrm{BW}} &= \sum_{n=0}^{\infty} \hat{F}_{\mathrm{BW}}^{(n)}, \\
\hat{F}_{\mathrm{BW}}^{(0)} &= \hat{H}_{0,0}, \\
\hat{F}_{\mathrm{BW}}^{(1)} &= \sum_{m_1 \neq 0} \frac{\hat{H}_{0,m_1}\hat{H}_{m_1,0}}{m_1\omega}, \\
\hat{F}_{\mathrm{BW}}^{(2)} &= \sum_{\{m_j\}\neq 0} \left(\frac{\hat{H}_{0,m_1}\hat{H}_{m_1,m_2}\hat{H}_{m_2,0}}{m_1 m_2 \omega^2} - \frac{\hat{H}_{0,m_1}\hat{H}_{m_1,0}\hat{H}_{0,0}}{m_1^2\omega^2} \right), \\
\hat{F}_{\mathrm{BW}}^{(3)} &= \sum_{\{m_j\}\neq 0} \left[\frac{\hat{H}_{0,m_1}\hat{H}_{m_1,m_2}\hat{H}_{m_2,m_3}\hat{H}_{m_3,0}}{m_1 m_2 m_3 \omega^3} - \frac{\hat{H}_{0,m_1}\hat{H}_{m_1,m_2}\hat{H}_{m_2,0}\hat{H}_{0,0}}{m_1 m_2 \omega^3} \left(\frac{1}{m_1} + \frac{1}{m_2} \right) \right. \\
&\quad \left. - \frac{\hat{H}_{0,m_1}\hat{H}_{m_1,0}\hat{H}_{0,m_2}\hat{H}_{m_2,0}}{m_1^2 m_2 \omega^3} + \frac{\hat{H}_{0,m_1}\hat{H}_{m_1,0}\hat{H}_{0,0}\hat{H}_{0,0}}{m_1^3\omega^3} \right], \\
\hat{F}_{\mathrm{BW}}^{(4)} &= \sum_{\{m_j\}\neq 0} \left[\frac{\hat{H}_{0,m_1}\hat{H}_{m_1,m_2}\hat{H}_{m_2,m_3}\hat{H}_{m_3,m_4}\hat{H}_{m_4,0}}{m_1 m_2 m_3 m_4 \omega^4} \right. \\
&\quad - \frac{\hat{H}_{0,m_1}\hat{H}_{m_1,m_2}\hat{H}_{m_2,m_3}\hat{H}_{m_3,0}\hat{H}_{0,0}}{m_1 m_2 m_3 \omega^4} \left(\frac{1}{m_1} + \frac{1}{m_2} + \frac{1}{m_3} \right) \\
&\quad - \frac{\hat{H}_{0,m_1}\hat{H}_{m_1,m_2}\hat{H}_{m_2,0}\hat{H}_{0,m_3}\hat{H}_{m_3,0}}{m_1 m_2 m_3 \omega^4} \left(\frac{1}{m_1} + \frac{1}{m_2} \right) - \frac{\hat{H}_{0,m_1}\hat{H}_{m_1,0}\hat{H}_{0,m_2}\hat{H}_{m_2,m_3}\hat{H}_{m_3,0}}{m_1^2 m_2 m_3 \omega^4} \\
&\quad + \frac{\hat{H}_{0,m_1}\hat{H}_{m_1,m_2}\hat{H}_{m_2,0}\hat{H}_{0,0}\hat{H}_{0,0}}{m_1 m_2 \omega^4} \left(\frac{1}{m_1^2} + \frac{1}{m_1 m_2} + \frac{1}{m_2^2} \right) \\
&\quad + \frac{\hat{H}_{0,m_1}\hat{H}_{m_1,0}\hat{H}_{0,m_2}\hat{H}_{m_2,0}\hat{H}_{0,0}}{m_1^2 m_2 \omega^4} \left(\frac{1}{m_1} + \frac{1}{m_2} \right) \\
&\quad \left. + \frac{\hat{H}_{0,m_1}\hat{H}_{m_1,0}\hat{H}_{0,0}\hat{H}_{0,m_2}\hat{H}_{m_2,0}}{m_1^3 m_2 \omega^4} - \frac{\hat{H}_{0,m_1}\hat{H}_{m_1,0}\hat{H}_{0,0}\hat{H}_{0,0}\hat{H}_{0,0}}{m_1^4\omega^4} \right].
\end{aligned}
\tag{3.36}
$$

Here, we note that these expressions are invariant under $\hat{H}_m \to \hat{H}_m e^{-im\omega t_0}$ and $\hat{\Omega}_{m,0} \to \hat{\Omega}_{m,0} e^{-im\omega t_0}$ unlike in the Floquet-Magnus Hamiltonian. The same expression can also be obtained by replacing ϵ_α in Eq. (3.27) with $\hat{F}_{\mathrm{BW}}$ in the rightmost position, although with this procedure one cannot obtain the wave operator.

3.2.6 Relation with other frameworks

Now, let us clarify the relation of the present formalism with the high-frequency expansion for the Floquet-Magnus Hamiltonian (and the van Vleck expansion). As we have seen in Eq. (2.28), we can relate these expansions by comparing the expression for the time evolution operator.

To this end, we first denote the wave operator in the time domain as

$$\hat{\Xi}(t) = \sum_{m=-\infty}^{\infty} \hat{\Omega}_{m,0} e^{-im\omega t}, \tag{3.37}$$

namely, the quasienergy eigenstate $|\psi_\alpha(t)\rangle$ is expressed as[5]

$$|\psi_\alpha(t)\rangle = |u_\alpha(t)\rangle e^{-i\epsilon_\alpha t} = \frac{\hat{\Xi}(t)|v_\alpha\rangle e^{-i\epsilon_\alpha t}}{\sqrt{\langle v_\alpha|\hat{\Omega}^\dagger\hat{\Omega}|v_\alpha\rangle}}. \tag{3.38}$$

Then, with Eq. (2.1), the time evolution operator is expressed as

$$\hat{U}(t,t_0) = \hat{\Xi}(t) e^{-i\hat{F}_{\mathrm{BW}}(t-t_0)} \sum_\alpha \frac{|v_\alpha\rangle\langle v_\alpha|}{\langle v_\alpha|\hat{\Omega}^\dagger\hat{\Omega}|v_\alpha\rangle} \hat{\Xi}^\dagger(t_0) \tag{3.39}$$

$$= \hat{\Xi}(t) e^{-i\hat{F}_{\mathrm{BW}}(t-t_0)} \hat{\Xi}^{-1}(t_0). \tag{3.40}$$

Here we have introduced

$$\hat{\Xi}^{-1}(t) = \sum_\alpha \frac{|v_\alpha\rangle\langle v_\alpha|}{\langle v_\alpha|\hat{\Omega}^\dagger\hat{\Omega}|v_\alpha\rangle} \hat{\Xi}^\dagger(t), \tag{3.41}$$

which is indeed the inverse of $\hat{\Xi}(t)$, since

$$\hat{\Xi}(t)\hat{\Xi}^{-1}(t) = \sum_\alpha |u_\alpha(t)\rangle\langle u_\alpha(t)| = 1. \tag{3.42}$$

We note that $\hat{\Omega}$ is not invertible in the extended Hilbert space since $\mathrm{rank}\hat{\Omega} \leq \dim\hat{\mathscr{H}}$, while $\hat{\Xi}(t)$ is defined on the original Hilbert space and thus invertible.

With this, we can relate the quantities in the Brillouin-Wigner theory and those in the Floquet-Magnus basis as

$$\hat{F}_{\mathrm{FM}}(t_0) = \hat{\Xi}(t_0)\hat{F}_{\mathrm{BW}}\hat{\Xi}^{-1}(t_0), \tag{3.43}$$

$$e^{-i\hat{\Lambda}(t,t_0)} = \hat{\Xi}(t)\hat{\Xi}(t_0)^{-1}, \tag{3.44}$$

$$\hat{\Xi}^{-1}(t) = T^{-1}\int_0^T dt' e^{-i\hat{\Lambda}(t',t_0)} e^{i\hat{\Lambda}(t,t_0)}. \tag{3.45}$$

[5]Here, $\langle v_\alpha|\hat{\Xi}^\dagger(t)\hat{\Xi}(t)|v_\alpha\rangle$ is time-independent and equals to $\langle v_\alpha|\hat{\Omega}^\dagger\hat{\Omega}|v_\alpha\rangle$, due to the orthogonality among the redundant solutions $\sum_m \langle u_{\alpha,m+n}|u_{\alpha,m}\rangle = \delta_{n0}$.

3.3 Application to Floquet topological insulators

3.3.1 Amplitude expansion and divergent spectra

As we have seen, an advantage of the Brillouin-Wigner expansion lies in deriving higher-order terms. In particular, in the single-root formalism, we can have an explicit expression even in the infinite order, so that one can take an infinite summation of designated forms. This can also be done by changing the way in which we separate the whole Hamiltonian $\hat{\mathscr{H}} - \hat{\mathscr{M}}\omega$ into an unperturbed and perturbative parts.

To derive the high-frequency expansion, we have chosen $-\hat{\mathscr{M}}\omega$ and $\hat{\mathscr{H}}$ as the unperturbed and perturbative part, respectively. Here let us introduce another choice, where the perturbation part is given as $\hat{\mathscr{H}}_0 - \hat{\mathscr{M}}\omega$ with $[\hat{\mathscr{H}}_0]_{m,n} = \hat{H}_0\delta_{m,n}$, i.e., the diagonal part of the extended Hamiltonian. By denoting the off-diagonal part as $\hat{\mathscr{H}}_p = \hat{\mathscr{H}} - \hat{\mathscr{H}}_0$, we can rewrite the wave operator and Brillouin-Wigner Hamiltonian as

$$\hat{\Omega}_\alpha = \left(1 - \frac{\hat{\mathscr{Q}}}{\epsilon_\alpha + \hat{\mathscr{M}}\omega - \hat{\mathscr{H}}_0}\hat{\mathscr{H}}_p\right)^{-1}\hat{\mathscr{P}}, \tag{3.46}$$

$$\hat{\mathscr{F}}_{\mathrm{BW}}(\epsilon_\alpha) = \hat{\mathscr{P}}(\hat{\mathscr{H}} - \hat{\mathscr{M}}\omega)\left(1 - \frac{\hat{\mathscr{Q}}}{\epsilon_\alpha + \hat{\mathscr{M}}\omega - \hat{\mathscr{H}}_0}\hat{\mathscr{H}}_p\right)^{-1}\hat{\mathscr{P}} \tag{3.47}$$

$$\begin{aligned} &= \hat{\mathscr{P}}(\hat{\mathscr{H}} - \hat{\mathscr{M}}\omega)\hat{\mathscr{P}} + \hat{\mathscr{P}}\hat{\mathscr{H}}_p\frac{\hat{\mathscr{Q}}}{\epsilon_\alpha + \hat{\mathscr{M}}\omega - \hat{\mathscr{H}}_0}\hat{\mathscr{H}}_p\hat{\mathscr{P}} \\ &+ \hat{\mathscr{P}}\hat{\mathscr{H}}_p\frac{\hat{\mathscr{Q}}}{\epsilon_\alpha + \hat{\mathscr{M}}\omega - \hat{\mathscr{H}}_0}\hat{\mathscr{H}}_p\frac{\hat{\mathscr{Q}}}{\epsilon_\alpha + \hat{\mathscr{M}}\omega - \hat{\mathscr{H}}_0}\hat{\mathscr{H}}_p\hat{\mathscr{P}} + \dots. \end{aligned} \tag{3.48}$$

Here, in the absence of external fields, i.e., when the amplitude of the external field A goes to zero, the off-diagonal part should vanish, so that $\hat{\mathscr{H}}_0 = \mathscr{O}(1)$ and $\hat{\mathscr{H}}_p = \mathscr{O}(A)$. Hence this expansion assures that a truncation at n terms has an $\mathscr{O}(A^n)$ error. In general $\hat{\mathscr{H}}_p$ is not necessarily linear in A, so that the n-th term may also include $\mathscr{O}(A^n)$ contributions.

Since the expansion is controlled not by the frequency but by the amplitude, it is expected to be accurate even for low-frequency driving if the amplitude is sufficiently small. However, as we shall see below, the radius of convergence can be finite, and the topological property is not captured in the effective Hamiltonian.

To see this, here we consider the setup for the Floquet topological insulator, i.e.,

a two-dimensional Dirac system driven by a circularly-polarized laser, i.e.,

$$\hat{H}(t) = \Gamma \begin{pmatrix} 0 & ke^{-i\phi} + Ae^{-i\omega t} \\ ke^{i\phi} + Ae^{i\omega t} & 0 \end{pmatrix}, \tag{3.49}$$

where $ke^{i\phi} = k_1 + ik_2$, and $\Gamma = \pm 1$ is the chirality [32].

Here we again consider the projection onto the zero-photon sector. By using Eq. (3.48) for this Hamiltonian, we obtain

$$\begin{aligned} \hat{F}_{\mathrm{BW}}(\epsilon) = \Gamma k \begin{pmatrix} 0 & e^{-i\phi} \\ e^{i\phi} & 0 \end{pmatrix} + A^2 \frac{\epsilon - \omega}{(\epsilon-\omega)^2 - k^2} \begin{pmatrix} 1 & 0 \\ 0 & 0 \end{pmatrix} + A^2 \frac{\epsilon + \omega}{(\epsilon+\omega)^2 - k^2} \begin{pmatrix} 0 & 0 \\ 0 & 1 \end{pmatrix} \\ + A^4 \begin{pmatrix} \frac{\epsilon - 2\omega}{(\epsilon-2\omega)^2 - k^2} \left(\frac{k}{(\epsilon-\omega)^2 - k^2} \right)^2 & 0 \\ 0 & \frac{\epsilon + 2\omega}{(\epsilon+2\omega)^2 - k^2} \left(\frac{k}{(\epsilon+\omega)^2 - k^2} \right)^2 \end{pmatrix} + \mathcal{O}(A^6). \end{aligned} \tag{3.50}$$

By replacing ϵ with $\hat{F}_{\mathrm{BW}}$ as a rightmost operator, we finally obtain the multi-root Brillouin-Wigner Hamiltonian as

$$\begin{aligned} \hat{F}_{\mathrm{BW}} = \Gamma k \begin{pmatrix} 0 & e^{-i\phi} \\ e^{i\phi} & 0 \end{pmatrix} - \frac{A^2(\omega^2 - 2k^2)}{\omega(\omega^2 - 4k^2)} \begin{pmatrix} 1 & 0 \\ 0 & -1 \end{pmatrix} - \frac{\Gamma A^2 k}{(\omega^2 - 4k^2)} \begin{pmatrix} 0 & e^{-i\phi} \\ e^{i\phi} & 0 \end{pmatrix} \\ + \frac{A^4 k^2 (\omega^2 + 8k^2)}{4\omega^2(\omega^2 - k^2)(\omega^2 - 4k^2)^2} \left[\omega \begin{pmatrix} 1 & 0 \\ 0 & -1 \end{pmatrix} + \Gamma k \begin{pmatrix} 0 & e^{-i\phi} \\ e^{i\phi} & 0 \end{pmatrix} \right] + \frac{A^4 \omega(\omega^2 - 2k^2)}{(\omega^2 - 4k^2)^3} \begin{pmatrix} 1 & 0 \\ 0 & -1 \end{pmatrix} \\ + \frac{A^4 k^2 (7\omega^2 - 4k^2)}{4\omega^3(\omega^2 - 4k^2)^2} \begin{pmatrix} 1 & 0 \\ 0 & -1 \end{pmatrix} + \frac{\Gamma A^4 \omega^2 k}{(\omega^2 - 4k^2)^3} \begin{pmatrix} 0 & e^{-i\phi} \\ e^{i\phi} & 0 \end{pmatrix} + \mathcal{O}(A^6). \end{aligned} \tag{3.51}$$

If $k \ll \omega$, this formula recovers the result of the high-frequency expansion [28],

$$\begin{aligned} \hat{F}_{\mathrm{BW}} = \Gamma k \begin{pmatrix} 0 & e^{-i\phi} \\ e^{i\phi} & 0 \end{pmatrix} - \frac{A^2}{\omega} \begin{pmatrix} 1 & 0 \\ 0 & -1 \end{pmatrix} - \frac{A^2}{\omega^2} \Gamma k \begin{pmatrix} 0 & e^{-i\phi} \\ e^{i\phi} & 0 \end{pmatrix} \\ + \frac{A^2(A^2 - 2k^2)}{\omega^3} \begin{pmatrix} 1 & 0 \\ 0 & -1 \end{pmatrix} + \frac{A^2(A^2 - 4k^2)}{\omega^4} \Gamma k \begin{pmatrix} 0 & e^{-i\phi} \\ e^{i\phi} & 0 \end{pmatrix} + \mathcal{O}(\omega^{-5}). \end{aligned} \tag{3.52}$$

We show the quasienergy spectra obtained with the amplitude expansion and the high-frequency expansion in Fig. 3.5, along with the numerically exact one. While both expansions reproduce the exact solution well for small k/ω, the amplitude expansion diverges at $|k/\omega| = 1/2, 1$. This implies that the radius of convergence is at most $1/\omega = 1/2k$. Since we choose the zero-photon sector as the model space, the ex-

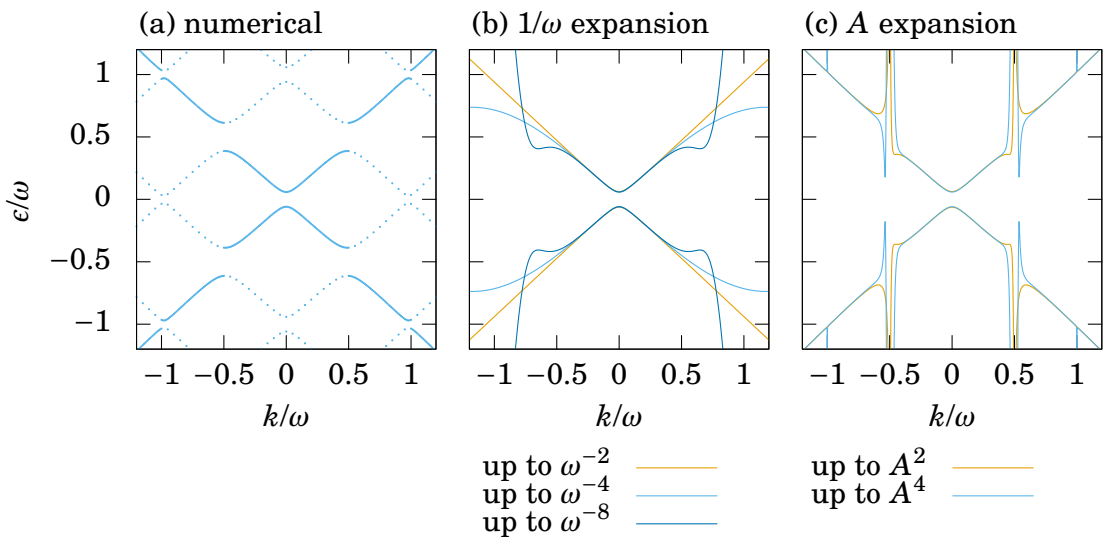

Figure 3.5: Comparison of quasienergy spectra calculated with (a) the exact numerical diagonalization, (b) high-frequency expansion, and (c) amplitude expansion. Here we set $A = 0.25$. While solid and dotted lines in (a) are equivalent in quasienergy, the projection on the zero-photon sector should reproduce the solid ones.

act Brillouin-Wigner Hamiltonian should reproduce the numerically exact spectrum drawn with solid lines in Fig. 3.5(a). They are discontinuous and cannot be described analytically, which is why the expansion seems not converge at $|k/\omega| = 1/2, 1, \ldots$.

3.3.2 Effective Hamiltonian for doubled subspaces

We have seen that the zero-photon projection exhibits divergent spectra at the avoided crossing between the Floquet sidebands except at Γ point ($k/\omega \sim 0$). This implies that one cannot evaluate the topological number derived from those energy gaps using the zero-photon projection. On the other hand, since there is no restriction on the choice of the model space, let us here change the model space from the zero-photon subspace to a doubled one, i.e., the zero- and N-photon subspaces. We can apply Eq. (3.48) to such a choice, just by changing the definition of $\hat{\mathscr{P}}$ to $\hat{P}_{m,n} = \delta_{m,0} + \delta_{m,N}$.

Here we again consider the Floquet topological insulator, Eq. (3.49), and try to capture the level repulsion occurring at $k = N\omega/2$. For simplicity, here we start with the case of $N \geq 2$. Since the present problem has a tridiagonal form with $\hat{H}_0$ and $\hat{H}_{\pm 1}$,

the effective Hamiltonian in the extended space reads

$$
\begin{aligned}
\hat{F}_{\mathrm{BW}}(\epsilon) = &\begin{pmatrix} \hat{H}_{0,0} & 0 \\ 0 & \hat{H}_{N,N} - N\omega \end{pmatrix} \\
&+ \begin{pmatrix} \hat{H}_{0,-1}(\epsilon - \omega - \hat{H}_{-1,-1})^{-1}\hat{H}_{-1,0} & 0 \\ 0 & \hat{H}_{N,N+1}(\epsilon + (N+1)\omega - \hat{H}_{N+1,N+1})^{-1}\hat{H}_{N+1,N} \end{pmatrix} \\
&+ \begin{pmatrix} \hat{H}_{0,1}(\epsilon + \omega - \hat{H}_{1,1})^{-1}\hat{H}_{1,0} & 0 \\ 0 & \hat{H}_{N,N-1}(\epsilon + (N-1)\omega - \hat{H}_{N-1,N-1})^{-1}\hat{H}_{N-1,N} \end{pmatrix} \\
&+ \begin{pmatrix} 0 & \hat{H}_{0,1}\prod_{j=1}^{N-1}(\epsilon + j\omega - \hat{H}_{j,j})^{-1}\hat{H}_{j,j+1}) \\ \text{h.c.} & 0 \end{pmatrix}.
\end{aligned}
\tag{3.53}
$$

Here we neglect $\mathcal{O}(A^3)$ contributions for the intra-(photon-)sector terms, while we include the leading-order term for the inter-sector terms. By transforming the Hamiltonian with

$$
\hat{U} = \frac{1}{\sqrt{2}} \begin{pmatrix} 1 & -e^{-i\phi} & 0 & 0 \\ e^{i\phi} & 1 & 0 & 0 \\ 0 & 0 & 1 & -e^{-i\phi} \\ 0 & 0 & e^{i\phi} & 1 \end{pmatrix}
\tag{3.54}
$$

so as to make $\hat{H}_{0,0}$ diagonal[6], we arrive at

$$\hat{U}^\dagger \hat{F}_{\mathrm{BW}} \hat{U} = \begin{pmatrix} \Gamma k & 0 & 0 & 0 \\ 0 & -\Gamma k & 0 & 0 \\ 0 & 0 & \Gamma k - N\omega & 0 \\ 0 & 0 & 0 & -\Gamma k - N\omega \end{pmatrix}$$
$$+ \frac{A^2(\omega^2 - 2k^2)}{\omega(\omega^2 - 4k^2)} \begin{pmatrix} 0 & e^{-i\phi} & 0 & 0 \\ e^{i\phi} & 0 & 0 & 0 \\ 0 & 0 & 0 & e^{-i\phi} \\ 0 & 0 & e^{i\phi} & 0 \end{pmatrix} - \frac{\Gamma A^2 k}{\omega^2 - 4k^2} \begin{pmatrix} 1 & 0 & 0 & 0 \\ 0 & -1 & 0 & 0 \\ 0 & 0 & 1 & 0 \\ 0 & 0 & 0 & -1 \end{pmatrix}$$
$$+ \frac{\Gamma^{N-1} A^N k^{N-1}}{2 \prod_{j=1}^{N-1} ((\epsilon + j\omega)^2 - k^2)} \begin{pmatrix} 0 & 0 & e^{-iN\phi} & -e^{-i(N+1)\phi} \\ 0 & 0 & e^{-i(N-1)\phi} & -e^{-iN\phi} \\ e^{iN\phi} & e^{i(N-1)\phi} & 0 & 0 \\ -e^{i(N+1)\phi} & -e^{iN\phi} & 0 & 0 \end{pmatrix}. \quad (3.55)$$

Now we are interested in the case $k \sim N\omega/2$, where the states with $\epsilon \sim -k, k - N\omega$ have much lower energy than those with $\epsilon \sim k, -k - N\omega$. By projecting out higher-energy states further, we finally obtain

$$\hat{F}_{\mathrm{eff}}^{\Gamma=\pm 1} = -\frac{N\omega}{2} - \left(k - \frac{N\omega}{2} + \frac{A^2 k}{4k^2 - \omega^2}\right) \begin{pmatrix} 1 & 0 \\ 0 & -1 \end{pmatrix}$$
$$- \frac{\Gamma^{N-1} A^N k^{N-1}}{2(N-1)! \omega^{N-1} \prod_{j=1}^{N-1} (j\omega - 2k)} \begin{pmatrix} 0 & e^{-i(N-\Gamma)\phi} \\ e^{i(N-\Gamma)\phi} & 0 \end{pmatrix}. \quad (3.56)$$

Similarly we can obtain the effective Hamiltonian for $N = 1$ as

$$\hat{F}_{\mathrm{eff}}^{\Gamma=\pm 1} = -\frac{\omega}{2} - \left(k - \frac{\omega}{2} + \frac{A^2}{4(2k + \omega)}\right) \begin{pmatrix} 1 & 0 \\ 0 & -1 \end{pmatrix} + \frac{\Gamma A}{2} \begin{pmatrix} 0 & e^{-i(1-\Gamma)\phi} \\ e^{i(1-\Gamma)\phi} & 0 \end{pmatrix}. \quad (3.57)$$

We show the quasienergy spectra in Fig. 3.6, which agree well with the numerical result in the vicinity of $k \sim N\omega/2$.

[6]Note that this transformation is multi-valued at $k = 0$, so that it degrades the gauge invariance of the Berry curvature at $k = 0$. Hence we cannot use this transformation for discussing the Berry curvature and associated Chern number near $k = 0$, which we have discussed with the high-frequency expansion. Here we consider $k \sim N\omega/2$ ($N \neq 0$), where the Berry curvature is invariant under the transformation.

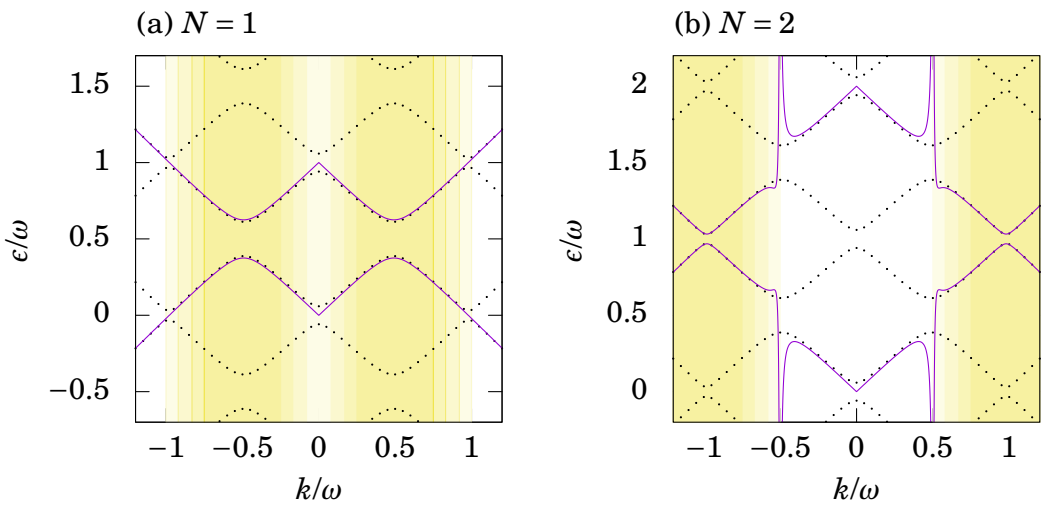

Figure 3.6: Quasienergy spectra calculated using the sideband effective Hamiltonians for (a) $N = 1$ and (b) $N = 2$, with $A = 0.25$. The exact solution calculated numerically is shown with dotted lines for comparison. Colored regions indicate the relevant ($k/\omega \sim N/2$) avoided crossing between the Floquet sidebands.

The energy gaps open at

$$|k| = \begin{cases} \dfrac{\omega}{2} - \dfrac{A^2}{8\omega} & (N = 1) \\ \dfrac{N\omega}{2} - \dfrac{NA^2}{2(N^2-1)\omega} & (N \geq 2) \end{cases}, \tag{3.58}$$

with the topological gap given, in the leading order, as

$$2\Delta = \frac{A}{((N-1)!)^2}\left(\frac{NA}{2\omega}\right)^{N-1} \sim \frac{\omega}{\pi}\left(\frac{e^2 A}{2N\omega}\right)^N. \tag{3.59}$$

We also show the texture of $\hat{\boldsymbol{R}} = \boldsymbol{R}/|\boldsymbol{R}|$ with $\boldsymbol{R} = \mathrm{Tr}[\hat{F}_{\mathrm{BW}}\hat{\boldsymbol{\sigma}}/2]$ in Fig. 3.7. Along the minimum, Eq. (3.58), of each topological gap. the texture has a topological pattern that contributes to the Chern number $C_\pm$ as $\pm(N - \Gamma)$. Note that here $\pm$ denotes upper (+) and lower (−) bands of the effective Hamiltonian, but not those in the first Floquet Brillouin zone $(-\omega/2, \omega/2]$. If one folds the spectrum into the first Floquet Brillouin zone, the lower and upper bands for odd N are reversed.

Here, while the quasienergy dispersion is the same for $\Gamma = +1$ and $\Gamma = -1$, the texture and associated Chern number are obtained in different forms[7], as a result of

[7]Ref. [80] reports a symmetric result $C_\pm = \pm N$ as opposed to the present result, which is due to an incorrect definition of the Hamiltonian [Eq. (4), overall factor s is dropped]. The absolute value of the

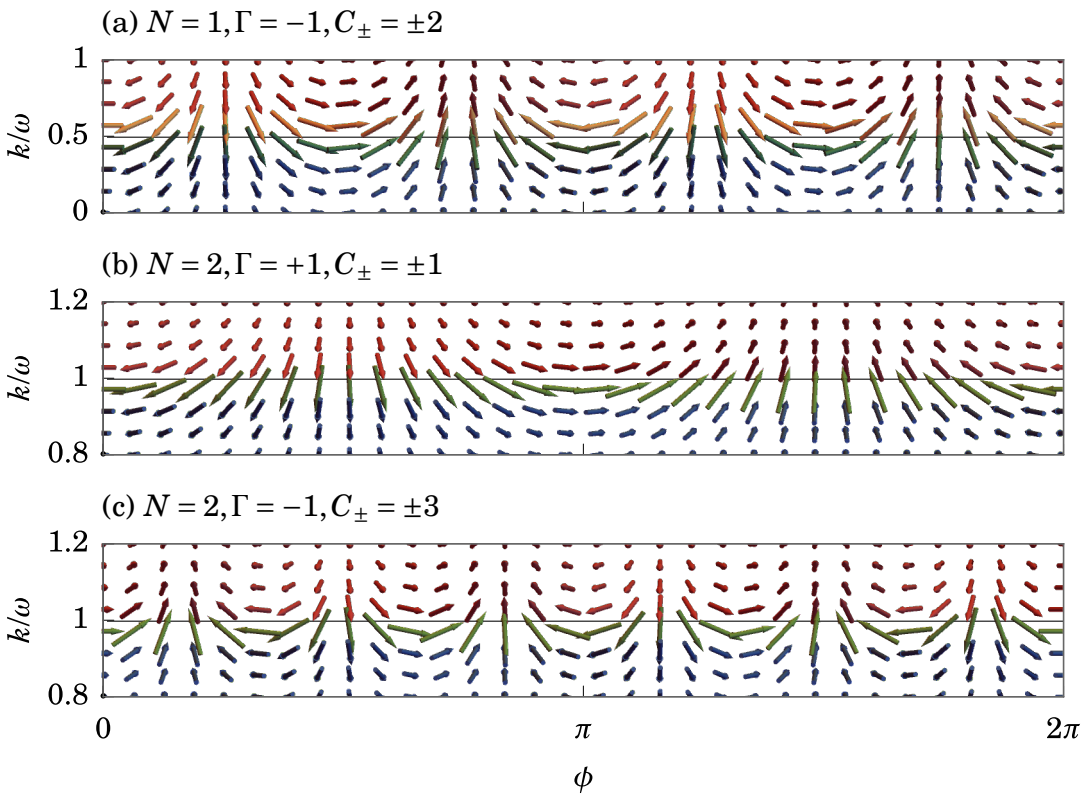

Figure 3.7: The texture of $\hat{\boldsymbol{R}} = \boldsymbol{R}/|\boldsymbol{R}|$ with $\boldsymbol{R} = \mathrm{Tr}[\hat{F}_{\mathrm{BW}}\hat{\boldsymbol{\sigma}}/2]$, for $A = 0.25$. The value of R_z is represented by the color of arrows, where red (blue) is assigned to $R_z = +1$ (-1). Horizontal lines indicate the respective positions of the topological gaps. (a) $N = 1$, $\Gamma = -1$, (b) $N = 2$, $\Gamma = +1$, and (c) $N = 2$, $\Gamma = -1$.

the broken time-reversal symmetry due to the circularly-polarized laser.

We also note that, while results obtained here are leading-order expressions, the obtained Chern numbers are essentially valid even in the infinite order, as a consequence of the continuous rotational symmetry for the present Hamiltonian Eq. (3.49). Due to the rotational symmetry, the Hamiltonian for general ϕ is related to that of $\phi = 0$ as

$$\hat{H}(t;\phi) = \begin{pmatrix} 1 & 0 \\ 0 & e^{i\phi} \end{pmatrix} \hat{H}(t - \phi/\omega; \phi = 0) \begin{pmatrix} 1 & 0 \\ 0 & e^{-i\phi} \end{pmatrix}. \tag{3.60}$$

Namely, the time-periodic part of the quasienergy eigenstate $|u(t)\rangle$ can be expressed as

$$|u(t;\phi)\rangle = \begin{pmatrix} 1 & 0 \\ 0 & e^{i\phi} \end{pmatrix} |u(t - \phi/\omega; \phi = 0)\rangle, \tag{3.61}$$

obtained Chern number is also incorrect due to an inappropriate treatment [Eq. (A.2), λ should not be zero but θ_k].

or, in the extended Hilbert space,

$$|\boldsymbol{u}(\phi)\rangle = \begin{pmatrix} e^{i\hat{\mathcal{M}}\phi} & 0 \\ 0 & e^{i(\hat{\mathcal{M}}+1)\phi} \end{pmatrix} |\boldsymbol{u}(\phi=0)\rangle. \tag{3.62}$$

This relation ensures that the ϕ-dependence of the Brillouin-Wigner Hamiltonian is given as

$$\hat{\mathscr{F}}_{\mathrm{BW}}(\phi) = \begin{pmatrix} e^{i\hat{\mathcal{M}}\phi} & 0 \\ 0 & e^{i(\hat{\mathcal{M}}+1)\phi} \end{pmatrix} \hat{\mathscr{F}}_{\mathrm{BW}}(\phi=0) \begin{pmatrix} e^{-i\hat{\mathcal{M}}\phi} & 0 \\ 0 & e^{-i(\hat{\mathcal{M}}+1)\phi} \end{pmatrix}, \tag{3.63}$$

which also holds for the truncated Hamiltonian Eq. (3.56). Namely, Eq. (3.56) has a form of

$$\hat{F}_{\mathrm{eff}}^{\Gamma=\pm1} = -\frac{N\omega}{2} - f_{\mathrm{D}}(k,\omega,A)\begin{pmatrix} 1 & 0 \\ 0 & -1 \end{pmatrix} - f_{\mathrm{OD}}(k,\omega,A)\begin{pmatrix} 0 & e^{-i(N-\Gamma)\phi} \\ e^{i(N-\Gamma)\phi} & 0 \end{pmatrix} \tag{3.64}$$

even in the infinite order in A, so that the Chern number does not change unless $f_{\mathrm{D}}(k,\omega,A)$ has a sign change at a finite A.

3.3.3 Effects of a nonlinear dispersion on the topological structure

We found in the previous section that two Dirac cones with opposite chiralities have a series of topological gaps at $|\boldsymbol{k}| = \omega/2, \omega, 3\omega/2\ldots$ due to a weak circularly-polarized laser, and contribute to the Chern number as $2, -4, 6, -8, \ldots$ for the lower band in the first Floquet Briilouin zone[8]. Namely, if we do not consider a cutoff momentum, the Chern number for the driven Dirac system is divergent. However, these gaps are nonlinear and small depending on the driving amplitude A as $A, A^2, A^3, \ldots$, so that a perturbation larger than the energy scale of those gaps may spoil this topological structure. Indeed, to realize the Dirac dispersion in condensed-matter systems, e.g., on a honeycomb lattice, the energy dispersion becomes nonlinear as we go away from the Dirac point, which acts as the perturbation to destruct the topological structure.

While the cutoff momentum for the discussion of the Chern number should be determined as the momentum where the nonlinear dispersion affects the Chern number, we cannot reproduce the entire Chern number just by summing up contributions within the cutoff momentum; As ω is increased, the number of topological gaps

[8]If one folds the quasienergy spectrum into the first Floquet Brillouin zone $(-\omega/2,\omega/2]$, the upper band of Eq. (3.56) for $|\boldsymbol{k}| = \omega/2, 3\omega/2, \ldots$ turns into the lower band, so that the signs in the sequence appear in an alternating way.

within the cutoff momentum increases and the Chern number should also increase monotonically. However, such a monotonicity is in fact not observed in Fig. 3.3. This implies that the perturbation derived from the nonlinear dispersion can not only make the energy gap trivial, but also nontrivial with a different Chern number. Since the way in which the nonlinear dispersion is introduced depends on details of models, such contributions to the Chern number are not universal.

3.4 Application to Floquet Weyl semimetals

3.4.1 Weyl nodes in the zero-photon sector

In this section, we shall discuss another type of topological systems induced by periodic driving, i.e., the Floquet Weyl semimetals. The Floquet Weyl semimetal emerges when the three-dimensional Dirac semimetal is irradiated by a circularly-polarized laser. The low-energy Hamiltonian (in terms of the $\boldsymbol{k}\cdot\boldsymbol{p}$ theory) for the driven Dirac semimetal is expressed as[9]

$$\hat{H}(\boldsymbol{k},t) = \Gamma \begin{pmatrix} k\cos\theta & k\sin\theta e^{-i\phi} - Ae^{-i\omega t} \\ k\sin\theta e^{i\phi} - Ae^{i\omega t} & -k\cos\theta \end{pmatrix}. \tag{3.65}$$

Here, $\Gamma = \pm 1$ denotes the chirality while $\boldsymbol{k} = (k_1, k_2, k_3) = k(\sin\theta\cos\phi, \sin\theta\sin\phi, \cos\theta)$, and we set the Fermi velocity as unity. In the absence of the external field A, the energy spectrum is given by a linear dispersion $\epsilon(\boldsymbol{k}) = \pm k$, which is doubly degenerated for $\Gamma = \pm 1$.

As Ref. [90] has shown, the periodic driving induces a splitting of Weyl nodes from $\boldsymbol{k} = 0$, which is understood in terms of the high-frequency expansion. Let us start with grasping this phenomenon with the Brillouin-Wigner expansion for the zero-photon sector with respect to the amplitude. By applying Eq. (3.48) for the zero-photon sector, one obtains the Brillouin-Wigner Hamiltonian as

$$\begin{aligned} \hat{F}_{\mathrm{BW}}(\boldsymbol{k}) = &\left(\Gamma k\cos\theta - A^2 \frac{\omega^2 - 2k^2\sin^2\theta + 2\Gamma\omega k\cos\theta}{\omega(\omega^2 - 4k^2)}\right)\begin{pmatrix} 1 & 0 \\ 0 & -1 \end{pmatrix} \\ &+ \Gamma k\sin\theta\left(1 - A^2\frac{\omega + 2\Gamma k\cos\theta}{\omega(\omega^2 - 4k^2)}\right)\begin{pmatrix} 0 & e^{-i\phi} \\ e^{i\phi} & 0 \end{pmatrix} + \mathcal{O}(A^4). \end{aligned} \tag{3.66}$$

This expansion can be seen as a k/ω correction up to infinite order in a leading-

[9] While originally the Dirac semimetal is represented as a 4×4 matrix, here we choose the chiral representation, with which the Hamiltonian is block diagonal in the chirality if the mass term is absent.

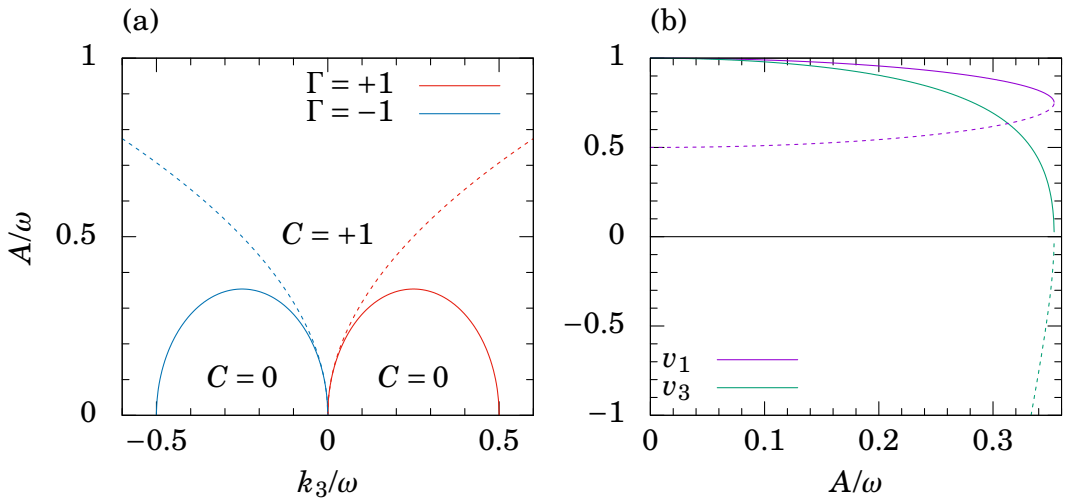

Figure 3.8: (a) Trajectories of Weyl nodes $\boldsymbol{k}_{\text{weyl}}^{0,\Gamma,\pm} = k_3 \boldsymbol{e}_z$ against A in the zero-photon sector. Solid lines are obtained from the Brillouin-Wigner amplitude expansion, while dashed lines the high-frequency expansion. C denotes the Chern number for the lower band with a fixed k_3, i.e., the number of surface Fermi arcs. (b) Fermi velocity of the Weyl nodes along the x, y direction and the z direction. Dashed lines are those for the spurious Weyl nodes $\boldsymbol{k}_{\text{Weyl}}^{0,\Gamma,-}$, whose velocity diverges ($v_3 \to -\infty$) as $A \to 0$.

order expression for the high-frequency expansion, so that one can expect that locations of the Weyl node is more accurate than in the high-frequency expansion. The locations are obtained by imposing vanishing matrix elements in Eq. (3.66) as

$$\boldsymbol{k}_{\text{Weyl}}^{0,\Gamma,\pm} = \Gamma \frac{\omega \mp \sqrt{\omega^2 - 8A^2}}{4} \boldsymbol{e}_z, \tag{3.67}$$

which are plotted in Fig. 3.8(a) along with the result of the high-frequency expansion.

The emergence of the Weyl semimetal due to the periodic driving is seen around $k_3 = 0$. We can note a significant deviation from the high-frequency expansion as an annihilation of the Weyl nodes at $A = \omega/\sqrt{8} \sim 0.35\omega$. Since the Weyl node is a topological object (having a monopole charge), it cannot annihilate alone but only as a pair with another Weyl node having an opposite monopole charge. Such additional Weyl nodes for the pair annihilation emerge from $\boldsymbol{k} = \pm(\omega/2)\boldsymbol{e}_z$ in the present case (as $\boldsymbol{k}_{\text{Weyl}}^{0,\Gamma,-}$). However, as in the case of the Floquet topological insulators in the previous section, the present Hamiltonian has a divergent spectra at these points ($k = \omega/2$), which implies a finite radius of convergence. Hence the additional Weyl nodes $\boldsymbol{k}_{\text{Weyl}}^{0,\Gamma,-}$ should be spurious, but this evokes the presence of emergent Weyl nodes in the Floquet sidebands. Indeed, we shall show that there exist infinite numbers of

Weyl nodes in the Floquet sidebands in the next subsection, which are subject to pair annihilation with each other.

Before going to the sidebands, here we discuss properties of the Weyl nodes in the zero-photon sector. Expanding Eq. (3.66) around $\boldsymbol{k}_{\mathrm{Weyl}}^{0,\Gamma,+}$ reveals the linear dispersion,

$$\hat{F}_{\mathrm{BW}}(\boldsymbol{k}_{\mathrm{Weyl}}^{0,\Gamma,+}+\boldsymbol{k}) = \Gamma v_3 k\cos\theta \begin{pmatrix} 1 & 0 \\ 0 & -1 \end{pmatrix} + \Gamma v_1 k \sin\theta \begin{pmatrix} 0 & e^{-i\phi} \\ e^{i\phi} & 0 \end{pmatrix} + \mathcal{O}(k^2), \tag{3.68}$$

where

$$v_1 = \frac{3\omega+\sqrt{\omega^2-8A^2}}{4\omega}, v_3 = \frac{2\sqrt{\omega^2-8A^2}}{\omega+\sqrt{\omega^2-8A^2}}. \tag{3.69}$$

We show v_1 and v_3 against A in Fig. 3.8(b), with those for the spurious Weyl nodes $\boldsymbol{k}_{\mathrm{Weyl}}^{0,\Gamma,-}$ indicated by the dashed lines.

This expression clarifies the number of surface Fermi arcs. Let us consider the Chern number for the lower band with a fixed k_3, whose absolute value coincides with the number of Fermi arcs. Equation (3.7) leads to the contribution from each Weyl node, $C = -\frac{\Gamma}{2}\mathrm{sgn}\, k_3$ (note that k_3 denotes the relative coordinate from the Weyl node). Namely, when one crosses the Weyl node from $k_3 < 0$ to $k_3 > 0$, the Chern number changes by $-\Gamma$. With this, the number of Fermi arcs C is determined as shown in Fig. 3.8(a).

3.4.2 Hierarchy of the Weyl nodes in Floquet sidebands

Now, we discuss the Weyl nodes in Floquet sidebands. Since we are interested in the number of Fermi arcs at the zero (quasi)energy, we consider the doubled subspace with $\pm N$-photon sectors here ($N \geq 1$). While the hybridization between $(N+1)$- and $(-N)$-photon sectors also creates surface states as can be seen by a straightforward application, they cross the edge of the Floquet Brillouin zone at $\epsilon = \omega/2$.

As in the application of the Floquet topological insulator, the amplitude expansion

Eq. (3.48) for the doubled subspace yields

$$
\begin{aligned}
\hat{V}^\dagger \hat{\mathscr{F}}_{\mathrm{BW}} \hat{V} = &\begin{pmatrix} \Gamma g k - N\omega & 0 & 0 & 0 \\ 0 & -\Gamma g k - N\omega & 0 & 0 \\ 0 & 0 & \Gamma g k + N\omega & 0 \\ 0 & 0 & 0 & -\Gamma g k + N\omega \end{pmatrix} \\
&+ g A^2 k \frac{\Gamma\omega + 2k_3}{\omega(4k^2 - \omega^2)} \begin{pmatrix} 1 & 0 & 0 & 0 \\ 0 & -1 & 0 & 0 \\ 0 & 0 & 1 & 0 \\ 0 & 0 & 0 & -1 \end{pmatrix} \\
&- g A^2 \frac{(2k^2 - \omega^2 - \Gamma\omega k_3)}{\omega(4k^2 - \omega^2)} \begin{pmatrix} \cos\theta & -e^{-i\phi}\sin\theta & 0 & 0 \\ -e^{i\phi}\sin\theta & -\cos\theta & 0 & 0 \\ 0 & 0 & \cos\theta & -e^{-i\phi}\sin\theta \\ 0 & 0 & -e^{i\phi}\sin\theta & -\cos\theta \end{pmatrix} \\
&- \frac{g A^{2N} (k + |k_3|)^{N+1/2} (k - |k_3|)^{N-1/2}}{2k(2N-1)!\,\omega^{2N-1} \prod_{j=1}^{2N-1} (2k - \Gamma g j \omega)} \begin{pmatrix} 0 & 0 & 0 & e^{i(2N-1)\phi} \\ 0 & 0 & 0 & 0 \\ 0 & 0 & 0 & 0 \\ e^{-i(2N-1)\phi} & 0 & 0 & 0 \end{pmatrix} \\
&- \frac{g A^{2N} (k + |k_3|)^{N-1/2} (k - |k_3|)^{N+1/2}}{2k(2N-1)!\,\omega^{2N-1} \prod_{j=1}^{2N-1} (2k + \Gamma g j \omega)} \begin{pmatrix} 0 & 0 & 0 & 0 \\ 0 & 0 & e^{i(2N+1)\phi} & 0 \\ 0 & e^{-i(2N+1)\phi} & 0 & 0 \\ 0 & 0 & 0 & 0 \end{pmatrix} \\
&+ \frac{g \Gamma A^{2N} (k^2 - k_3^2)^N}{2k \prod_{j=1}^{2N-1} \{(\epsilon_\alpha + (N-j)\omega)^2 - k^2\}} \begin{pmatrix} 0 & 0 & e^{i2N\phi} & 0 \\ 0 & 0 & 0 & -e^{i2N\phi} \\ e^{-i2N\phi} & 0 & 0 & 0 \\ 0 & -e^{-i2N\phi} & 0 & 0 \end{pmatrix},
\end{aligned}
\tag{3.70}
$$

where $g = \mathrm{sgn}\, k_3$ and we have used the unitary transformation to diagonalize $\hat{H}_0$,

$$
\hat{V} = \begin{cases} \begin{pmatrix} \cos\dfrac{\theta}{2} & -e^{-i\phi}\sin\dfrac{\theta}{2} \\ e^{i\phi}\sin\dfrac{\theta}{2} & \cos\dfrac{\theta}{2} \end{pmatrix} & (\cos\theta > 0) \\ \begin{pmatrix} -\sin\dfrac{\theta}{2} & -e^{-i\phi}\cos\dfrac{\theta}{2} \\ e^{i\phi}\cos\dfrac{\theta}{2} & -\sin\dfrac{\theta}{2} \end{pmatrix} & (\cos\theta < 0) \end{cases},
\tag{3.71}
$$

which is assured to be single-valued. While this Hamiltonian includes eigenstates

with quasienergies $\pm(k - N\omega)$ and $\pm(k + N\omega)$ in the leading order in A, the latter is irrelevant to the present discussion, so that we project them out. Then we obtain a 2×2 effective Hamiltonian for low-energy states as

$$\hat{F}^{N,\Gamma}_{\text{eff}}(\boldsymbol{k}) = \left(k - N\omega + A^2 \frac{k^2 + k_3^2 + \omega\Gamma k_3}{k(4k^2 - \omega^2)}\right)\begin{pmatrix} 1 & 0 \\ 0 & -1 \end{pmatrix} - g\frac{A^{2N}(k + |k_3|)^{N+\Gamma g/2}(k - |k_3|)^{N-\Gamma g/2}}{2k(2N-1)!\omega^{2N-1}\prod_{j=1}^{2N-1}(2k - j\omega)}\begin{pmatrix} 0 & e^{i(2N-\Gamma g)\phi} \\ e^{-i(2N-\Gamma g)\phi} & 0 \end{pmatrix}. \tag{3.72}$$

Let us observe how the Weyl nodes emerge in the Floquet sidebands. In the absence of the driving field, the quasienergy spectrum has zero quasienergy degenerated points on spheres $k = N\omega$. Once the field is turned on, these points are gapped out, except for

$$\boldsymbol{k}^{+N,\Gamma,\pm}_{\text{Weyl}} = \frac{(2N + \Gamma)\omega \pm \sqrt{(2N - \Gamma)^2\omega^2 - 8A^2}}{4}\boldsymbol{e}_z, \tag{3.73}$$

$$\boldsymbol{k}^{-N,\Gamma,\pm}_{\text{Weyl}} = \frac{-(2N - \Gamma)\omega \mp \sqrt{(2N + \Gamma)^2\omega^2 - 8A^2}}{4}\boldsymbol{e}_z. \tag{3.74}$$

Here, since they behave in small A as

$$\boldsymbol{k}^{\pm N,\Gamma,+}_{\text{Weyl}} \sim \pm\left(N\omega - \frac{A^2}{(2N \mp \Gamma)\omega}\right)\boldsymbol{e}_z,\ \boldsymbol{k}^{\pm N,\Gamma,-}_{\text{Weyl}} = \left(\frac{\Gamma\omega}{2} \pm \frac{A^2}{(2N \mp \Gamma)\omega}\right)\boldsymbol{e}_z, \tag{3.75}$$

$\boldsymbol{k}^{\pm N,\Gamma,-}_{\text{Weyl}}$ is again spurious. Namely, the spherical degenerated points at $k = N\omega$ turn into four Weyl nodes ($\boldsymbol{k}^{\pm N,\pm 1,+}_{\text{Weyl}}$ and $\boldsymbol{k}^{\pm N,\mp 1,+}_{\text{Weyl}}$) along k_3-axis by the periodic driving.

Let us expand the effective Hamiltonian around the Weyl nodes. Within the leading order in A/ω, one obtains

$$\hat{F}^{N,\Gamma}_{\text{eff}}(\boldsymbol{k}^{\pm N,\Gamma,+}_{\text{Weyl}} + \boldsymbol{k}) = \pm k_3\begin{pmatrix} 1 & 0 \\ 0 & -1 \end{pmatrix} \mp \frac{A^{2N}(2N\omega)^{\pm\Gamma-1}(k_1^2 + k_2^2)^{N\mp\Gamma/2}}{((2N-1)!\omega^{2N-1})^2}\begin{pmatrix} 0 & e^{i(2N\mp\Gamma)\phi} \\ e^{-i(2N\mp\Gamma)\phi} & 0 \end{pmatrix}. \tag{3.76}$$

Here, while the dispersion along k_3-axis is again linear, that along k_1 and k_2 is no longer linear but has an odd power $(2N \mp \Gamma)$. Also, the change in the Chern number for each value of k_3 as we change k_3 reads that the monopole charge for $\boldsymbol{k}^{\pm N,\Gamma,+}_{\text{Weyl}}$ is given as $(\pm 2N - \Gamma)$.

We display the trajectories and the monopole charge of these Weyl nodes $\boldsymbol{k}^{\pm N,\Gamma,+}_{\text{weyl}}$ in Fig. 3.9. While the trajectories are terminated at the places where the pair-annihilation with the spurious Weyl nodes $\boldsymbol{k}^{\pm N,\Gamma,-}_{\text{weyl}}$ occur, we can estimate from the

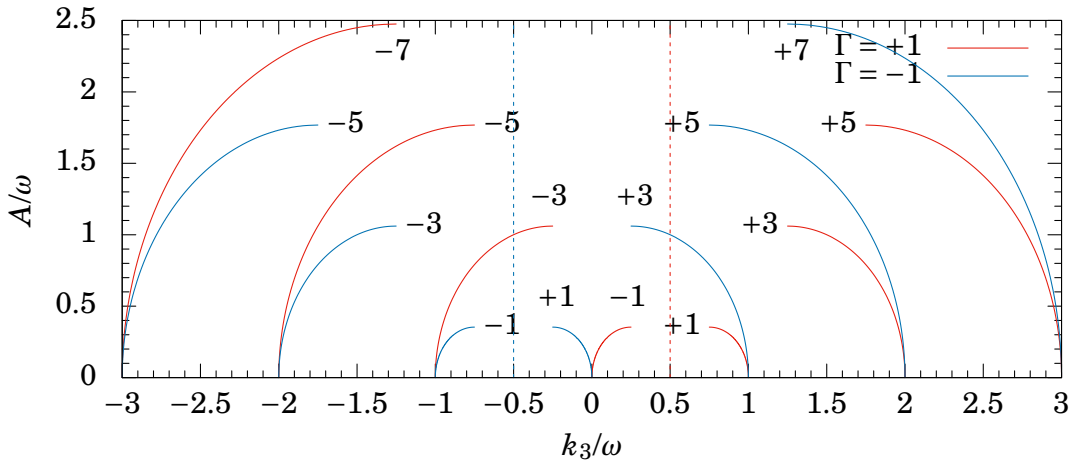

Figure 3.9: Trajectories of Weyl nodes in Floquet sidebands $\boldsymbol{k}_{\text{weyl}}^{\pm N,\Gamma,+} = k_3 \boldsymbol{e}_z$ against A. The numbers attached to the lines are the monopole charge for each Weyl node (i.e., the change in the Chern number for a fixed k_3 when we pass through from left to right). Dashed lines indicate where the energy spectrum is divergent.

plot that the pair-annihilation should occur between $\boldsymbol{k}_{\text{weyl}}^{+N,+1,+}$ and $\boldsymbol{k}_{\text{weyl}}^{-N+1,+1,+}$, or, $\boldsymbol{k}_{\text{weyl}}^{+N,-1,+}$ and $\boldsymbol{k}_{\text{weyl}}^{-N-1,-1,+}$, as they have the same chirality and opposite monopole charges. Indeed, the numerical calculation of the quasienergy spectrum shows that this conjecture holds [66]. The correct behavior of the pair annihilation should be captured in the effective Hamiltonian projected on the quadrupled subspace [e.g., $\pm N$- and $\pm(N+1)$- photon sectors], but analytical discussions given here might be difficult, since the Hamiltonian will then be a 4×4 matrix.

We note that the pair annihilation occurs between Weyl nodes distant in the momentum space. Namely, unless a strong perturbation inducing a large shift of the Weyl nodes is imposed, the presence of the Weyl nodes and accompanying Fermi arcs should be robust. In fact, as we see in the next subsection, it is the case when the nonlinear dispersion in lattice systems is introduced as a perturbation.

3.4.3 Branched Weyl nodes derived from a nonlinear dispersion

As in the case of Floquet topological insulators, when the Dirac cone is introduced on lattice systems, nonlinear dispersions appear in the Hamiltonian, which may have significant effects on the sideband Weyl nodes with large N. While such effect is not universal and depends on the details of Hamiltonian, here, we discuss how the structure of the Weyl nodes in the $N = \pm 1$ sector is affected by the nonlinear dispersion

employing a particular example. We consider a periodically-driven lattice model,

$$\hat{H}(\boldsymbol{k},t) = \Gamma \begin{pmatrix} \sin k_3 & \sin(k_1 - A\cos\omega t) - i\sin(k_2 - A\sin\omega t) \\ \text{c.c.} & -\sin k_3 \end{pmatrix}, \tag{3.77}$$

which coincides with Eq. (3.65) in the continuous limit ($A, k, \omega \ll 1$). This model has a square-shaped Brillouin zone and has the C_4-rotational symmetry. While the Dirac cone appears at $\boldsymbol{k} = (0,0,0)$ as well as at $\boldsymbol{k} = (\pi,\pi,\pi)$, they do not interfere for a small amplitude driving, so that here we concentrate on the former. To include the correction to Eq. (3.65), here we expand the lattice Hamiltonian up to the second order in A and the third order in $\boldsymbol{k}$;

$$\begin{aligned} \hat{H}_0 = \Gamma \begin{pmatrix} k_3 & k_1 - ik_2 \\ k_1 + ik_2 & -k_3 \end{pmatrix} - \frac{\Gamma}{6} \begin{pmatrix} k_3^3 & k_1^3 - ik_2^3 \\ k_1^3 + ik_2^3 & -k_3^3 \end{pmatrix} \\ - \frac{\Gamma A^2}{4} \begin{pmatrix} 0 & k_1 - ik_2 \\ k_1 + ik_2 & 0 \end{pmatrix} + \frac{\Gamma A^2}{24} \begin{pmatrix} 0 & k_1^3 - ik_2^3 \\ k_1^3 + ik_2^3 & 0 \end{pmatrix}, \end{aligned} \tag{3.78}$$

$$\hat{H}_{+1} = -\Gamma A \begin{pmatrix} 0 & 1 \\ 0 & 0 \end{pmatrix} + \frac{\Gamma A}{4} \begin{pmatrix} 0 & k_1^2 + k_2^2 \\ k_1^2 - k_2^2 & 0 \end{pmatrix}, \tag{3.79}$$

$$\hat{H}_{-1} = -\Gamma A \begin{pmatrix} 0 & 0 \\ 1 & 0 \end{pmatrix} + \frac{\Gamma A}{4} \begin{pmatrix} 0 & k_1^2 - k_2^2 \\ k_1^2 + k_2^2 & 0 \end{pmatrix}, \tag{3.80}$$

$$\hat{H}_{\pm 2} = -\frac{\Gamma A^2}{8} \begin{pmatrix} 0 & k_1 + ik_2 \\ k_1 - ik_2 & 0 \end{pmatrix} + \frac{\Gamma A^2}{48} \begin{pmatrix} k_3^3 & k_1^3 + ik_2^3 \\ k_1^3 - ik_2^3 & -k_3^3 \end{pmatrix}. \tag{3.81}$$

With these Floquet components, we can derive the 2×2 effective Hamiltonian up to A^2 and ω following the procedure in the previous subsection as

$$\begin{aligned} \hat{F}_{\text{eff}} = (R - \omega)\sigma_3 - A^2 \frac{k_1^2 + k_2^2 - (2Rk + \omega\Gamma k_3)}{k(4R^2 - \omega^2)} \hat{\sigma}_3 \\ - \frac{A^2}{k} \left(\frac{(2Rk + \omega\Gamma k_3)(k_1^2 + k_2^2)}{2(4R^2 - \omega^2)} + \frac{k_1^2 + k_2^2}{4} - \frac{7(k_1^4 + k_2^4)}{6(4R^2 - \omega^2)} \right) \hat{\sigma}_3 \\ + gA^2 \frac{(k_1^2 + k_2^2)^{1/2}}{k} \left(-\frac{k + \Gamma k_3}{2\omega(2R - \omega)} - \frac{k + \Gamma k_3}{16} + \frac{(k_1^2 + k_2^2)(5k + 7\Gamma k_3)}{16\omega(2R - \omega)} \right) e^{i(2 - \Gamma g)\phi} \hat{\sigma}_+ + \text{h.c.} \\ + gA^2 \frac{(k_1^2 + k_2^2)^{1/2}}{k} \left(\frac{k - \Gamma k_3}{16} + \frac{(k_1^2 + k_2^2)(k + 7\Gamma k_3)}{48\omega(2R - \omega)} \right) e^{-i(2 + \Gamma g)\phi} \hat{\sigma}_+ + \text{h.c.} \end{aligned} \tag{3.82}$$

with

$$R = k - \frac{k_1^4 + k_2^4 + k_3^4}{6k}, \tag{3.83}$$

and $g = \mathrm{sgn}\, k_3$. We note that one can confirm that the Hamiltonian in the previous section corresponds to $\omega \sim k \to 0$ limit.

A significant consequence of the nonlinear dispersion can be seen in the dispersion around $\boldsymbol{k}_{\mathrm{Weyl}}^{\pm 1,\Gamma,+}$ in Eqs. (3.73), (3.74). The original forms of the Hamiltonian Eq. (3.76) are, as we show again here,

$$\hat{F}_{\mathrm{eff}}(\boldsymbol{k}_{\mathrm{Weyl}}^{\pm 1,\pm 1,+} + \boldsymbol{k}) = \pm k_3 \begin{pmatrix} 1 & 0 \\ 0 & -1 \end{pmatrix} \mp \frac{A^2}{\omega^2}(k_1^2 + k_2^2)^{1/2} \begin{pmatrix} 0 & e^{i\phi} \\ e^{-i\phi} & 0 \end{pmatrix}, \tag{3.84}$$

$$\hat{F}_{\mathrm{eff}}(\boldsymbol{k}_{\mathrm{Weyl}}^{\pm 1,\mp 1,+} + \boldsymbol{k}) = \pm k_3 \begin{pmatrix} 1 & 0 \\ 0 & -1 \end{pmatrix} \mp \frac{A^2}{4\omega^4}(k_1^2 + k_2^2)^{3/2} \begin{pmatrix} 0 & e^{i3\phi} \\ e^{-i3\phi} & 0 \end{pmatrix}. \tag{3.85}$$

While the modified locations are given as

$$\boldsymbol{k}_{\mathrm{Weyl}}^{\pm 1,\pm 1,+} = \pm\left(\omega + \frac{\omega^3}{6} - \frac{A^2}{\omega} - \frac{A^2\omega}{2}\right)\boldsymbol{e}_z,\ \boldsymbol{k}_{\mathrm{Weyl}}^{\pm 1,\mp 1,+} = \pm\left(\omega + \frac{\omega^3}{6} - \frac{A^2}{3\omega} - \frac{A^2\omega}{6}\right)\boldsymbol{e}_z, \tag{3.86}$$

the expanded Hamiltonian around these nodes is, respectively,

$$\hat{F}_{\mathrm{eff}}(\boldsymbol{k}_{\mathrm{Weyl}}^{\pm 1,\pm 1,+} + \boldsymbol{k}) = \pm k_3 \begin{pmatrix} 1 & 0 \\ 0 & -1 \end{pmatrix} \mp \left(1 + \frac{\omega^2}{8}\right)\frac{A^2}{\omega^2}(k_1^2 + k_2^2)^{1/2} \begin{pmatrix} 0 & e^{i\phi} \\ e^{-i\phi} & 0 \end{pmatrix}, \tag{3.87}$$

$$\hat{F}_{\mathrm{eff}}(\boldsymbol{k}_{\mathrm{Weyl}}^{\pm 1,\mp 1,+} + \boldsymbol{k}) = \pm k_3 \begin{pmatrix} 1 & 0 \\ 0 & -1 \end{pmatrix} \pm \frac{A^2}{8}(k_1^2 + k_2^2)^{1/2} \begin{pmatrix} 0 & e^{-i\phi} \\ e^{i\phi} & 0 \end{pmatrix}. \tag{3.88}$$

Namely, a linear term emerges from the perturbation and dominates the cubic dispersion in the Hamiltonian for $\boldsymbol{k}_{\mathrm{Weyl}}^{\pm 1,\mp 1,+}$ here. As a result, the monopole charge of this Weyl node changes from ± 3 to ∓ 1.

It may sound strange that the monopole charge changes discontinuously by a perturbation. Actually, this change is compensated by emergent four C_4-rotational-symmetric Weyl nodes with the charge ± 1; they are branched from the Weyl node on the k_3-axis to $\pm k_1$- and $\pm k_2$- directions as a consequence of breaking of the continuous rotational symmetry around the k_3-axis due to the nonlinear correction terms.

For a vanishing off-diagonal term, which is a necessary condition for Weyl nodes, $\sin\theta = 0$ is required for the linear model Eq. (3.65). Now there are two exponential $e^{i(2\pm\Gamma g)\phi}$ in the off-diagonal term due to the nonlinear correction, the vanishing off-diagonal term can also be achieved when $\sin\theta \neq 0$ but $\phi = 0, \pm\pi/2, \pi$. For simplicity,

here we drop the irrelevant terms from Eq. (3.82) as

$$\hat{F}_{\text{eff}} = \left(k - \omega - A^2 \frac{k_1^2 + k_2^2 - (2k^2 + \omega\Gamma k_3)}{k(4k^2 - \omega^2)}\right)\begin{pmatrix}1 & 0\\ 0 & -1\end{pmatrix}$$
$$+ gA^2 \frac{(k_1^2 + k_2^2)^{1/2}}{k}\left(\frac{k - \Gamma k_3}{16} e^{-i(2+\Gamma g)\phi} - \frac{k + \Gamma k_3}{2\omega(2k - \omega)} e^{i(2-\Gamma g)\phi}\right)\hat{\sigma}_+ + \text{h.c.}. \tag{3.89}$$

Then the locations of the additional C_4-symmetric Weyl nodes are given as

$$\boldsymbol{k}_{\text{Weyl},C_4}^{-\Gamma,\Gamma,\alpha} = \left[\frac{4\sqrt{2}}{8+\omega^2}\omega^2 + \frac{A^2}{3\sqrt{2}}\right]\boldsymbol{a}_\alpha + \left[-\Gamma\frac{8-\omega^2}{8+\omega^2}\omega - \Gamma\frac{A^2}{3\omega}\right]\boldsymbol{e}_z, \tag{3.90}$$

with $\boldsymbol{a}_\alpha = \pm\boldsymbol{e}_x, \pm\boldsymbol{e}_y$ for $\alpha = \pm x, \pm y$. Here we have neglected $\mathcal{O}(A^4)$ and taken the leading order in ω in the $\mathcal{O}(A^2)$ term. The expanded Hamiltonian around these nodes are given as

$$\hat{F}_{\text{eff}}(\boldsymbol{k}_{\text{Weyl},C_4}^{\pm1,\mp1,+x} + \boldsymbol{k}) = \hat{F}_{\text{eff}}(\boldsymbol{k}_{\text{Weyl},C_4}^{\pm1,\mp1,-x} + \boldsymbol{k}) = \pm k_3\begin{pmatrix}1 & 0\\ 0 & -1\end{pmatrix} \mp \frac{A^2}{4}\begin{pmatrix}0 & k_1 + i2k_2\\ k_1 - i2k_2 & 0\end{pmatrix}, \tag{3.91}$$

$$\hat{F}_{\text{eff}}(\boldsymbol{k}_{\text{Weyl},C_4}^{\pm1,\mp1,+y} + \boldsymbol{k}) = \hat{F}_{\text{eff}}(\boldsymbol{k}_{\text{Weyl},C_4}^{\pm1,\mp1,-y} + \boldsymbol{k}) = \pm k_3\begin{pmatrix}1 & 0\\ 0 & -1\end{pmatrix} \pm \frac{A^2}{4}\begin{pmatrix}0 & 2k_1 + ik_2\\ 2k_1 - ik_2 & 0\end{pmatrix}, \tag{3.92}$$

which indeed have the ±1 monopole charges. The trajectory of the Weyl nodes against ω with higher-order corrections is shown in Fig. 3.10. As the trajectory shows, five Weyl nodes in the lattice model become closer when ω is decreased, where the description of the continuous model Eq. (3.65) is recovered, and finally merge to one node with the monopole charge $+3$, composed of four $+1$ and one -1.

This clearly demonstrates the robustness of the sideband Weyl nodes against perturbations in contrast to the two-dimensional case, where the contribution of the Floquet sidebands to the Chern number is significantly affected by the nonlinear dispersion.

3.5 Summary of Chapter 3

In this chapter, we have developed a Brillouin-Wigner theory for periodically-driven systems, and performed the high-frequency expansion and amplitude expansion. These frameworks have been applied to the two- and three-dimensional Dirac systems driven by a circularly-polarized laser. These systems are respectively known to

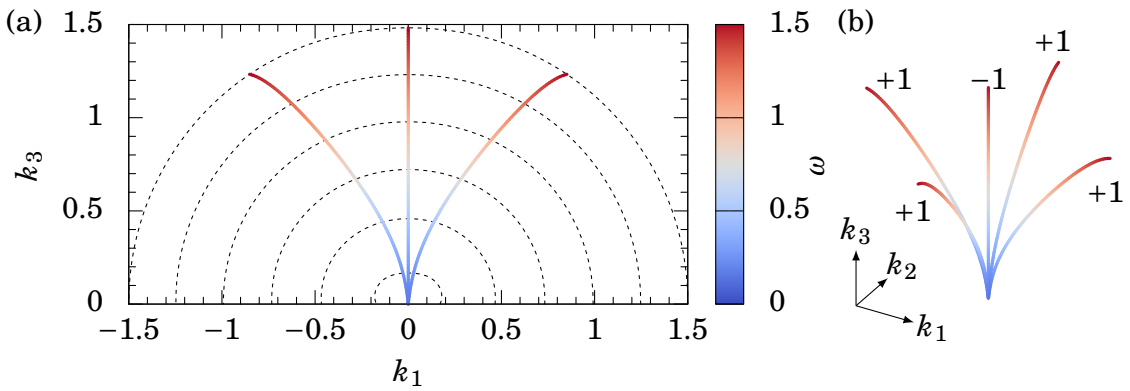

Figure 3.10: Trajectory of the location of Weyl nodes for $A = 0.25$, when ω is varied. (a) Trajectory on the k_1-k_3 plane. The colored solid lines represent the Weyl nodes, while dashed lines show energy minima in the radial direction for $\omega = 0.25, 0.5, \ldots, 1.5$. (b) A three-dimensional view. The numbers show the monopole charges.

have the topological gap and the Weyl nodes derived from the periodic driving. We have clarified the hierarchical structure in the topological gap and Weyl nodes, in a unified manner for both high-frequency and low-frequency driving. We have also discussed the distinction from the prediction here with numerical calculations for lattice systems, which arises from the nonlinear dispersion relation.

The topological structure emerging in the low-frequency driving would be relevant experimentally, since, e.g., for graphene the hopping amplitude is estimated as ~ 3 eV, which is larger than the driving frequency used in experiments.

The two-dimensional Dirac system is shown here to exhibit larger topological numbers as the driving frequency is lowered, although it would be degraded by the nonlinearity. This may give a possibility to realize large Hall responses, while the present study only discuss the mathematical aspect of the bulk Hamiltonian and the quasienergy distribution is not considered. How to understand the quasienergy distribution and to exploit this source of large Hall responses efficiently remain future problems.

The three-dimensional system also has large topological numbers, and they are shown to robust against perturbations. A number of the surface Fermi arcs should appear, and are expected to be observed experimentally by using the time-resolved ARPES. The Floquet replicas in Bi_2Se_3 have been observed experimentally [7, 8, 10] via the time-resolved ARPES with a mid-infrared pump laser $\omega \sim 0.2$ eV. $A \sim 0.5$, where the pair-annihilation occurs, can be achieved at $E \sim 0.2$ MeV/cm with this pump laser. Candidate materials are, for instance, Na_3Bi and Cd_3As_2, which have

stable Dirac cones due to a crystallographic symmetry [96, 97].

Chapter 4

Periodically-driven strong-coupling Hubbard model

So far, we have investigated properties of noninteracting systems under the periodic driving. In this chapter, we shall discuss the interplay between periodic driving and many-body interaction. In order to introduce the electron correlation in a simplest manner, here we consider the Hubbard model which is driven periodically.

A fundamental consequence of the electron correlation is magnetism, for which the Hubbard model is originally introduced. In this chapter we concentrate on the strong-coupling regime and consider the influence of the laser electric field to the spin degree of freedom via the electron correlation.

To this end, we shall develop the strong-coupling expansion to derive the effective spin Hamiltonian under the periodic driving in a systematic manner. As an interesting example, we propose here to apply the formalism to induce the chiral spin liquid. This indeed is one of consequences from the interplay between topology and correlation, which is expected to emerge under a circularly-polarized laser. We shall also find how the circularly-polarized laser can be used as a probe of exotic spin orders.

4.1 Background

Many-body interactions play a crucial role in various condensed-matter systems, including the spontaneous symmetry breaking and the Mott transition. In particular, for periodically-driven systems, the effect of many-body interactions can be significant even if the interaction is weak: This becomes relevant especially in lattice systems, since a phenomenon called the dynamical localization [26–28, 30] occurs.

In the periodically-driven lattice systems, their hopping amplitude becomes time-

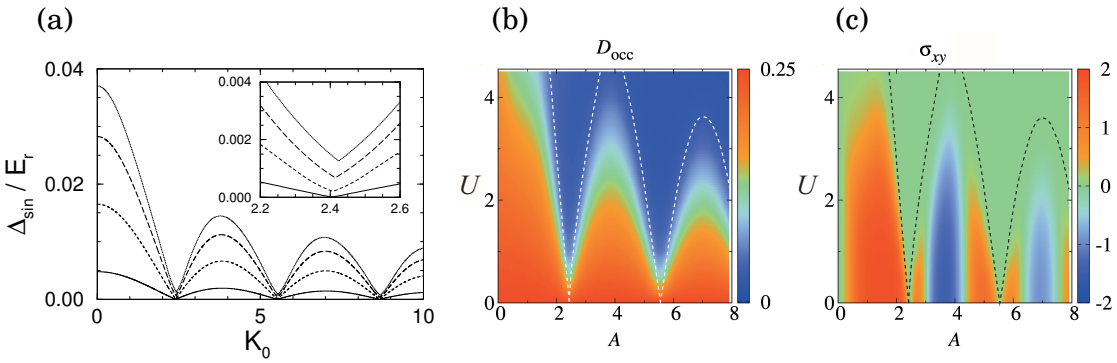

Figure 4.1: Signatures of the dynamical localization in (a) bosonic and (b, c) fermionic many-body systems. (a) Band width $\Delta_{\sin}$ of an optical lattice system under sinusoidal driving for various potential depths V_0 as a function of amplitude K_0. Cited from Ref. [30]. Energy is scaled by the recoil energy E_r. The dotted, long dashed, short dashed, and full lines correspond to $V_0/E_r = 2$, 3, 5, and 10, respectively. The inset zooms around the first zero of the zeroth Bessel function $j_{0,1} = 2.405$. (b) Expectation value of the double occupancy D_{occ} of the honeycomb Hubbard model driven by circularly-polarized laser, as a function of the amplitude A and onsite repulsion U. Cited from Ref. [28]. Hopping amplitude is taken as unity and the driving frequency as $\omega = 10$. The dashed line indicates the rescaled critical value $U = U_c \mathscr{J}_0(A)$, where U_c is the critical value for the Mott transition in equilibrium. (c) Hall conductivity σ_{xy} for the case of (b). Cited from Ref. [28].

dependent due to the additional Peierls phase factor,

$$t_{i,j} \to t_{i,j} e^{-i\boldsymbol{A}(t)\cdot(\boldsymbol{R}_i - \boldsymbol{R}_j)}, \tag{4.1}$$

where $t_{i,j}$ denotes hopping amplitude from site $\boldsymbol{R}_i$ to $\boldsymbol{R}_j$, and $\boldsymbol{A}(t)$ is the vector potential of the laser field. In this situation, due to the Jacobi-Anger identity,

$$e^{-iA\sin\omega t} = \sum_{n=-\infty}^{\infty} \mathscr{J}_n(A) e^{-in\omega t}, \tag{4.2}$$

with $\mathscr{J}_n(A)$ being the n-th Bessel function, a periodic electric field[1] $A(t) = A\sin\omega t$ renormalizes the hopping amplitude from t_{ij} to $\mathscr{J}_0(A)t_{ij}$ upon time average. Namely, the band width of the system effectively shrinks as a function of the field amplitude A. It is remarkable that one can realize an arbitrary narrow band by tuning the amplitude to zeros of the Bessel function. Hence the effect of the interaction can be dominant when the external field is turned on, even in weakly-coupled systems.

[1]Here we illustrate a one-dimensional case for simplicity.

This phenomenon is first proposed for a one-body system on a one-dimensional lattice [26], and applied to many-body phenomena such as the phase transition from a superfluid to a Mott insulator in a bosonic optical lattice system [27, 30], and the transition from topological to Mott insulators in fermionic honeycomb lattice systems driven by a circularly-polarized laser [28]. Characteristic features inherited from the Bessel function show up in such systems as shown in Fig. 4.1.

Strong correlation eventually induces a freezing of the charge degree of freedom. This leads to diverse physical phenomena, among which is an emergence of magnetism. This is captured minimally in the Hubbard model with an onsite interaction U,

$$\hat{H}_{\mathrm{Hub}} = -\sum_{ij\sigma} t_{i,j}\hat{c}^{\dagger}_{i\sigma}\hat{c}_{j\sigma} + \frac{1}{2}U\sum_{i}\hat{n}_i(\hat{n}_i - 1), \tag{4.3}$$

whose effective low-energy Hamiltonian at half filling up to the second-order perturbation in $t_{i,j}$ is the antiferromagnetic Heisenberg model,

$$\hat{H}_{\mathrm{Heis}} = -\sum_{\langle ij\rangle} J_{i,j}\left(\hat{\boldsymbol{S}}_i \cdot \hat{\boldsymbol{S}}_j - \frac{1}{4}\right), \tag{4.4}$$

with an exchange interaction $J_{i,j} = -4|t^2_{i,j}|/U$, where $\hat{\boldsymbol{S}}_i$ is the spin of an electron at site i. Here the coupling between neighboring spins emerges from charge fluctuations in Mott insulators.

This observation implies that the oscillating electric field can influence the spin degree of freedom via the electron correlation. Indeed, Ref. [98] shows that the exchange interaction $J_{i,j}$ is modulated, and even inverts its sign under strong periodic electric fields. This effect is also examined experimentally [99], by observing the dynamics of canted spin configurations due to the Dzyaloshinskii-Moriya interaction. As this exemplifies, periodic driving has crucial influences on both charge and spin degrees of freedom.

On the other hand, we have seen that the circularly-polarized laser induces topologically nontrivial phases in Chapter 3. In equilibrium, introducing correlation into the topological systems evokes us the fractional quantum Hall effect. While Ref. [28] already discusses the Hubbard model under a circularly-polarized laser, the absence of magnetic orders is assumed there. In the interplay of the topology and correlation, influence of the periodic driving on the spin degree of freedom is expected to play an crucial role.

Indeed, when the electron correlation is introduced to topologically-nontrivial models such as the Haldane model, the system can be a fractional Chern insulator in the intermediate coupling regime (in the vicinity of the Mott transition). This phase is also referred to as the chiral spin liquid phase, and closely related to that

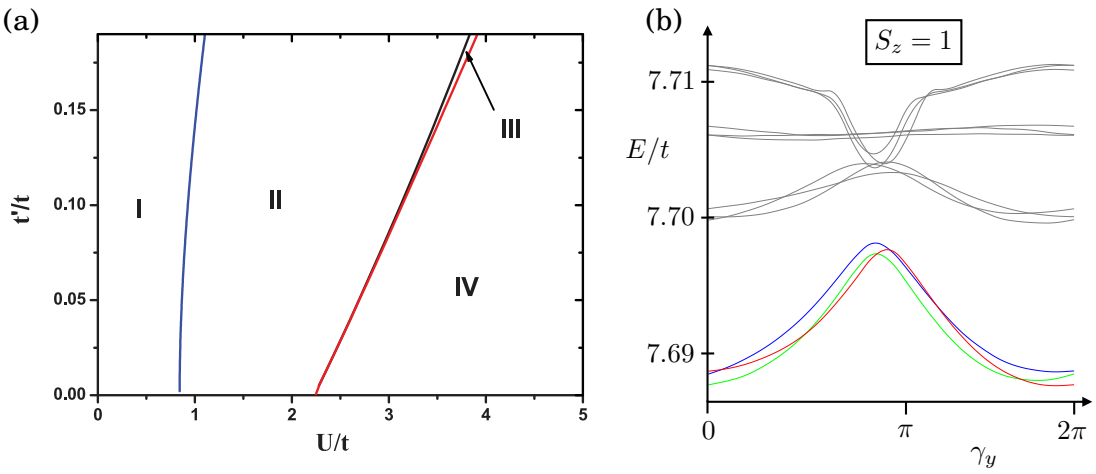

Figure 4.2: (a) Phase diagram of the Haldane Hubbard model determined with the slave-rotor mean-field theory, after Ref. [100]. t and t' are respectively the real nearest-neighbor and pure imaginary next-nearest-neighbor hopping, while U the onsite interaction. The four regions are respectively I: topological insulator, II: chiral spin liquid, III: spin density wave order with quantum anomalous Hall effect, and IV: trivial spin density wave order. (b) Evolution of the quasienergy spectrum (for the $S_z = 1$ sector) of the Floquet fractional Chern insulator by inserting a flux γ_y via twisting the boundary condition, which signals the topological degeneracy and the fractionalization as an aperiodicity against 2π flux insertion. The model is defined on the honeycomb lattice with the nearest-neighbor hopping t, onsite interaction $U = 3t$, and nearest-neighbor density-density interaction $V = 2t$. The spectrum is calculated with the exact diagonalization of a 4×6 site cluster with 8 particles. Cited from Ref. [101].

phase in the spin model obtained below with the strong-coupling expansion.

The existence of the chiral spin liquid phase for the Haldane Hubbard model is suggested in the intermediate coupling regime [100] with the slave-rotor mean field theory [102], as shown in Fig. 4.2(a). If one expands the Haldane Hubbard model to derive the spin Hamiltonian, one obtains the spin scalar chirality term $J_\chi(\hat{S}_i \times \hat{S}_j)\cdot\hat{S}_k$ due to the complex hopping [103], on top of the Heisenberg exchange interaction. The scalar spin chirality is a three-body spin correlation with a finite solid angle, as shown in Figs. 4.3(a) and 4.3(b). This term can induce the chiral spin liquid phase, which is confirmed numerically with the density-matrix renormalization group or exact diagonalization studies for Kagomé and honeycomb lattices [104, 105].

As we introduced in the previous chapter, the Haldane model is realized as an effective Hamiltonian in the high-frequency limit of the honeycomb lattice under a circularly-polarized laser. Hence one can expect that the chiral spin liquid phase can

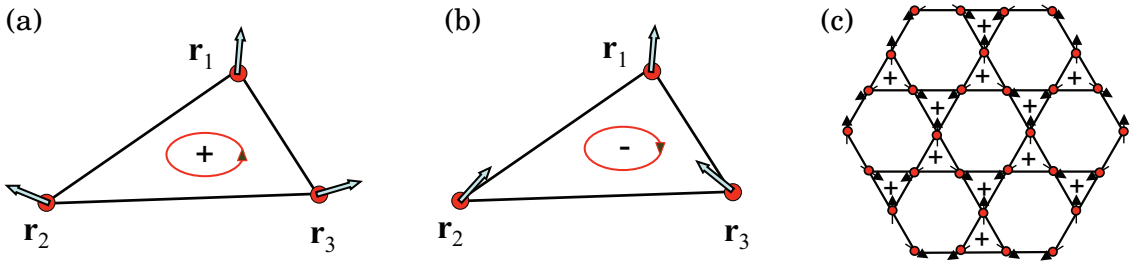

Figure 4.3: Schematic pictures of various spin chiralities, (a) positive scalar chirality, (a) negative scalar chirality, and (c) uniform vector chirality. After Ref. [106].

emerge by adding an onsite interaction to this driven system. Indeed, by numerical diagonalization of the model obtained from the high-frequency expansion with a small number of sites, some signatures for the emergence of the chiral spin liquid such as the fractional statistics are observed [101], as shown in Fig. 4.2(b). On the other hand, it is also reported that a renormalization of the interaction due to the higher-order terms in the expansion can make the fractional Hall states unstable [107]. Also, since there are only limited numbers of frameworks to describe the spin liquid phase, only the nature of the ground state of the effective Hamiltonian has been studied so far, and the dynamical aspect of this system has yet to be investigated.

At any rate, realization of the chiral state as a ground state of the effective Floquet Hamiltonian may be a feasible way for the chiral spin liquid. However, the theoretical implications with the high-frequency expansion are based on an assumption where the system is driven with a frequency much higher than the charge gap [schematically depicted in Fig. 4.4(b)]. Although one can assume such situations, for instance by exploiting the dynamical localization, one should focus on a more realistic situation where the Mott insulator is driven by a laser with a midgap frequency against the charge gap, as depicted schematically in Fig. 4.4(a). These backgrounds motivate us to study the spin degree of freedom in the periodically-driven Hubbard systems, especially how the spin scalar chirality term emerges in the effective spin Hamiltonian as driving the system.

First we eliminate the charge-excitation degree of freedom (upper Hubbard band) by performing the strong-coupling expansion in the presence of the periodic driving, and derive a time-dependent spin model. Then, since the energy scale for the spin degree of freedom (lower Hubbard band) is much smaller than that of the driving frequency ω, one can apply the high-frequency expansion on this spin system. By such a procedure, we derive a formula for the scalar spin chirality term valid even

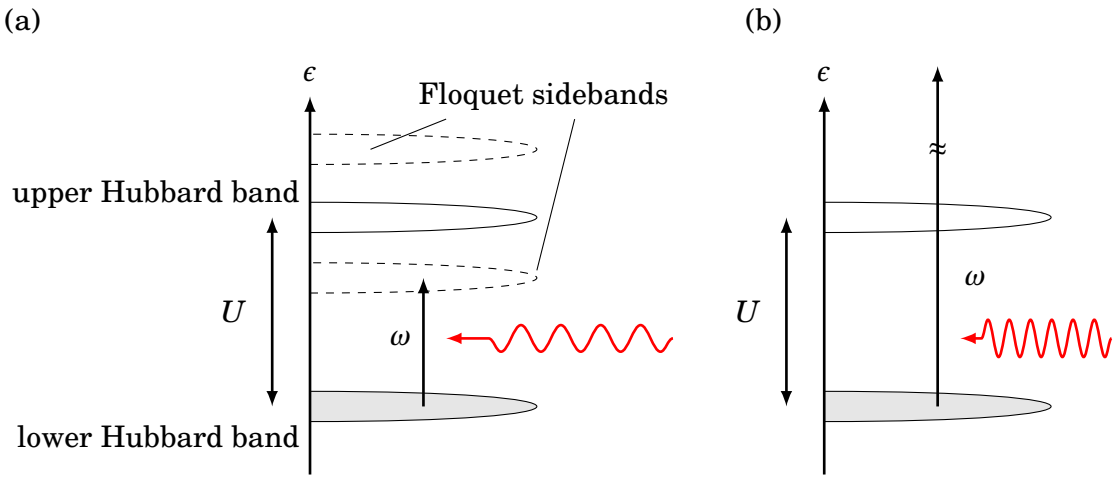

Figure 4.4: Schematic pictures for the relation between the charge gap U and driving frequency ω on an energy spectrum. (a) A central interest in the present study. (b) The case where the high-frequency expansion is applicable.

for $\omega < U$. After the derivation of the spin Hamiltonian, we shall observe how the chiral coupling J_χ behaves as a function of the driving frequency ω and amplitude A. We show that a significant enhancement of the chiral coupling in fact emerges in the intermediate regime $\omega \sim U$ as compared with the high-frequency regime.

On the other hand, the observation above implies that the optical response to the circularly-polarized laser can probe the chirality order in the strongly-correlated systems. We shall discuss how the dielectric function and the magnetization of the Mott insulator is influenced by the chirality order.

4.2 Strong-coupling expansion

4.2.1 General formulation

In the present chapter we consider the periodically-driven Hubbard model,

$$\hat{H}_{\mathrm{Hub}}(t) = -\sum_{ij\sigma} t_{i,j}(t)\hat{c}^\dagger_{i\sigma}\hat{c}_{j\sigma} + \frac{1}{2}U\sum_i \hat{n}_i(\hat{n}_i - 1), \tag{4.5}$$

at half filling in a two-dimensional geometry, with a time-dependent hopping amplitude

$$t_{i,j}(t) = t_{i,j}e^{-i\boldsymbol{A}(t)\cdot(\boldsymbol{R}_i - \boldsymbol{R}_j)} \tag{4.6}$$

obtained by the Peierls substitution of the vector potential for a monochromatic laser

$$\boldsymbol{A}(t) = \frac{1}{2}(\boldsymbol{A}e^{-i\omega t} + \boldsymbol{A}^* e^{i\omega t}). \tag{4.7}$$

Here $t_{i,j}$ denotes the bare real hopping amplitude from site $\boldsymbol{R}_j$ to $\boldsymbol{R}_i$. $\boldsymbol{A}$ is a time-independent complex amplitude; e.g., $\boldsymbol{A} = (1, i)$ for a circularly-polarized laser. Here, for simplicity, we assume that $|\boldsymbol{R}_i - \boldsymbol{R}_j| = 1$, and define θ_{ij} as $\boldsymbol{A}\cdot(\boldsymbol{R}_i - \boldsymbol{R}_j) = Ae^{i\theta_{ij}}$. General cases can be recovered by replacing $A \to A|\boldsymbol{R}_i - \boldsymbol{R}_j|$. Then the m-th Fourier component of the hopping amplitude $t_{i,j}^{(m)}$ is represented as

$$t_{i,j}^{(m)} = t_{i,j}\mathscr{J}_m(A)(-i)^m e^{im\theta_{ij}}. \tag{4.8}$$

Now, we are interested in the low-energy degree of freedom in the strong-coupling regime, namely the spin degree of freedom. To obtain the effective low-energy Hamiltonian, one can perform the strong-coupling expansion, i.e., the perturbative expansion from the atomic limit $t_{i,j} = 0$. In the atomic limit, the ground state is any state on the kernel of the double occupancy operator

$$\hat{D} = \frac{1}{2}\sum_i \hat{n}_i(\hat{n}_i - 1), \tag{4.9}$$

which can be labeled by the spin configuration. The huge degeneracy in the atomic limit is lifted by the perturbation with a finite amplitude t_{ij}.

In this section we newly develop a systematic procedure to derive the effective Hamiltonian as follows: we first take account of the charge degree of freedom as a perturbation to derive the time-dependent spin Hamiltonian, then perform the high-frequency expansion to derive the Floquet effective Hamiltonian describing the quasienergy spectrum of the driven Hubbard model[2].

Let us start with the first step. Here we denote the original Hamiltonian as $\hat{H}_{\mathrm{Hub}}(t) = \hat{T}(t) + U\hat{D}$ with the hopping operator $\hat{T}(t)$ and double occupancy $\hat{D}$ [Eq. (4.9)], and define the effective Hamiltonian in the strong-coupling expansion $\hat{H}_{\mathrm{SCE}}(t)$ as

$$\hat{H}_{\mathrm{SCE}}(t) = e^{i\hat{S}(t)}(\lambda\hat{T}(t) + U\hat{D} - i\partial_t)e^{-i\hat{S}(t)} - U\hat{D}, \tag{4.10}$$

[2]Note that these two steps in the expansion can also be performed simultaneously. With this formalism we can easily generalize the formalism to nonperiodic cases as discussed in the next chapter, and can also consider the dynamics of the spin system. The order of the block diagonalization of the photon sector and double occupancy can also be inverted in general, but, for perturbative approaches, the high-frequency expansion generates divergent terms coming from $(\omega - U)^{-1} \sim \sum_N U^N/\omega^{N+1}$, so that the strong-coupling expansion must be performed first in $\omega < U$ cases.

with a time-periodic unitary transformation $i\hat{S}(t)$. Here, we have subtracted $U\hat{D}$ for $\hat{H}_{\rm SCE}$ to vanish in the atomic limit, and $\lambda = 1$ is a bookkeeping constant. While this transformation is time-dependent, the Floquet quasienergy is invariant under the transformation due to the time periodicity.

By using Eqs. (2.40), (2.42) and (2.45), we can rewrite Eq. (4.10) in a convenient form for the present purpose,

$$\hat{H}_{\rm SCE}(t) + [U\hat{D}, i\hat{S}(t)] - i\partial_t i\hat{S}(t) = \lambda\hat{T}(t) + \sum_{n=1}^{\infty}\frac{B_n}{n!}{\rm ad}^n_{i\hat{S}}((-1)^n\lambda\hat{T}(t) - \hat{H}_{\rm SCE}(t)), \quad (4.11)$$

where B_n is the Bernoulli number and ${\rm ad}_X\bullet \equiv [X,\bullet]$. To obtain the perturbative series expansion, we consider a formal series in λ for $i\hat{S} = \sum_{n=1}^{\infty}\lambda^n i\hat{S}^{(n)}$ and $\hat{H}_{\rm SCE} = \sum_{n=1}^{\infty}\lambda^n\hat{H}^{(n)}_{\rm SCE}$. Here the zeroth order terms vanish for the atomic limit reproduced at $\lambda = 0$. Then, since $(-1)^n\lambda\hat{T}(t) - \hat{H}_{\rm SCE}(t)$ and $i\hat{S}(t)$ are at least first order in λ, N-th order terms on the right-hand side are composed of $i\hat{S}^{(n)}$ and $\hat{H}^{(n)}_{\rm SCE}$ with $n \le N-1$. Namely, one can determine the left-hand side [$i\hat{S}^{(N)}$ and $\hat{H}^{(N)}_{\rm SCE}$] order by order using this expression. For instance, first few orders for the right-hand side of Eq. (4.11), which we denote as $\hat{R}^{(N)}$ for the N-th order, is explicitly written as

$$\hat{R}^{(1)} = \hat{T}, \quad (4.12)$$

$$\hat{R}^{(2)} = \frac{1}{2}[i\hat{S}^{(1)}, \hat{T} + \hat{H}^{(1)}_{\rm SCE}], \quad (4.13)$$

$$\hat{R}^{(3)} = \frac{1}{2}[i\hat{S}^{(2)}, \hat{T} + \hat{H}^{(1)}_{\rm SCE}] + \frac{1}{2}[i\hat{S}^{(1)}, \hat{H}^{(2)}_{\rm SCE}] + \frac{1}{12}[i\hat{S}^{(1)}, [i\hat{S}^{(1)}, \hat{T} - \hat{H}^{(1)}_{\rm SCE}]], \quad (4.14)$$

$$\hat{R}^{(4)} = \frac{1}{2}[i\hat{S}^{(3)}, \hat{T} + \hat{H}^{(1)}_{\rm SCE}] + \frac{1}{2}[i\hat{S}^{(2)}, \hat{H}^{(2)}_{\rm SCE}] + \frac{1}{2}[i\hat{S}^{(1)}, \hat{H}^{(3)}_{\rm SCE}] - \frac{1}{12}[i\hat{S}^{(1)}, [i\hat{S}^{(1)}, \hat{H}^{(2)}_{\rm SCE}]]$$
$$+ \frac{1}{12}[i\hat{S}^{(1)}, [i\hat{S}^{(2)}, \hat{T} - \hat{H}^{(1)}_{\rm SCE}]] + \frac{1}{12}[i\hat{S}^{(2)}, [i\hat{S}^{(1)}, \hat{T} - \hat{H}^{(1)}_{\rm SCE}]]. \quad (4.15)$$

Note that, while we eventually consider the projection of $\hat{H}_{\rm SCE}$ onto $\hat{D} = 0$ subspace, $\hat{H}^{(n)}_{\rm SCE}$ appearing in the above formula should not be projected on this subspace since it also operates onto intermediate states ($\hat{D} \neq 0$).

To determine the detailed expressions for $\hat{H}_{\rm SCE}$ and $i\hat{S}$, it is convenient to decompose the unitary transformation in terms of the change in the double occupancy and the photon number as

$$i\hat{S}(t) = \sum_{d\neq 0}\sum_{m=-\infty}^{\infty} i\hat{S}_{d,m}e^{-im\omega t}. \quad (4.16)$$

Here $i\hat{S}_{d,m}$ changes the double occupancy by d and the photon number by m. One can always perform this decomposition since all the eigenvalue of $\hat{D}$ are integers.

The decomposition with respect to the double occupancy can be obtained explicitly as $i\hat{S}_d = \sum_{D=-\infty}^{\infty} \hat{P}_{D+d} i\hat{S}\hat{P}_D$ with a projection $\hat{P}_d = \prod_{D\neq d}[(\hat{D}-D)/(d-D)]$. Then

$$[U\hat{D}, i\hat{S}_{d,m}e^{-im\omega t}] - i\partial_t i\hat{S}_{d,m}e^{-im\omega t} = (dU - m\omega)i\hat{S}_{d,m}e^{-im\omega t} \tag{4.17}$$

holds, so that Eq. (4.11) can be solved order by order as

$$\hat{H}^{(N)}_{\mathrm{SCE}} = \left[\lambda\hat{T}(t) + \sum_{n=1}^{\infty}\frac{B_n}{n!}\mathrm{ad}^n_{i\hat{S}}((-1)^n\lambda\hat{T}(t) - \hat{H}_{\mathrm{SCE}}(t))\right]^{(N)}_{d=0}, \tag{4.18}$$

$$i\hat{S}^{(N)}_{d\neq 0,m} = T^{-1}\int_0^T dt e^{im\omega t}\frac{1}{dU - m\omega}\left[\sum_{n=0}^{\infty}\frac{B_n}{n!}\mathrm{ad}^n_{i\hat{S}}((-1)^n\lambda\hat{T}(t) - \hat{H}_{\mathrm{SCE}}(t))\right]^{(N)}_{d\neq 0}, \tag{4.19}$$

where

$$[\ldots]^{(N)}_d \equiv \frac{1}{N!}\sum_{D=-\infty}^{\infty}\hat{P}_{D+d}\frac{\partial^N[\ldots]}{\partial\lambda^N}\hat{P}_D. \tag{4.20}$$

4.2.2 Second-order perturbation

Now, let us obtain the expression for the effective Hamiltonian order by order. The first and second order terms in Eqs. (4.18, 4.19) are readlily given as

$$\hat{H}^{(1)}_{\mathrm{SCE}}(t) = \hat{T}_0(t), \tag{4.21}$$

$$i\hat{S}^{(1)}(t) = \sum_{m=-\infty}^{\infty}\sum_{d\neq 0}\frac{\hat{T}_{d,m}}{(dU - m\omega)}e^{-im\omega t}, \tag{4.22}$$

$$\hat{H}^{(2)}_{\mathrm{SCE}}(t) = \sum_{n,m=-\infty}^{\infty}\sum_{d\neq 0}\frac{[\hat{T}_{d,n}, \hat{T}_{-d,m-n}]}{2(dU - n\omega)}e^{-im\omega t}, \tag{4.23}$$

$$i\hat{S}^{(2)}(t) = \sum_{n,m=-\infty}^{\infty}\sum_{c,d\neq 0}\frac{[\hat{T}_{c,n}, \hat{T}_{d-c,m-n}]}{2(cU - n\omega)(dU - m\omega)}(1+\delta_{d-c})e^{-im\omega t}, \tag{4.24}$$

where $\hat{T}_{d,m} \equiv T^{-1}\int_0^T dt e^{im\omega t}\sum_{D=-\infty}^{\infty}\hat{P}_{D+d}i\hat{T}(t)\hat{P}_D$ is the hopping operator which changes the double occupancy by d and photon number by m.

Then we consider the projection of the effective Hamiltonian onto the $\hat{D} = 0$ subspace, where we have

$$\hat{H}^{(1)}_{\mathrm{SCE}}(t) = 0, \tag{4.25}$$

$$\hat{H}^{(2)}_{\mathrm{SCE}}(t) = -\sum_{n,m=-\infty}^{\infty}\frac{\hat{T}_{-1,m-n}\hat{T}_{+1,n}}{2(U - n\omega)}e^{-im\omega t} + \mathrm{h.c.}. \tag{4.26}$$

For the general time-dependent hopping amplitude $t_{ij}(t) = \sum_m t_{ij}^{(m)} e^{-im\omega t}$, the effective Hamiltonian can be written in terms of a cyclic permutation,

$$\begin{aligned}\hat{P}_{i_1 i_2 \ldots i_n} &= \sum_{\sigma_1,\sigma_2,\ldots,\sigma_n} |\sigma_n \sigma_1 \sigma_2 \ldots \sigma_{n-1}\rangle\langle \sigma_1 \sigma_2 \ldots \sigma_{n-1}\sigma_n| \\ &= \sum_{\sigma_1,\sigma_2,\ldots,\sigma_n} \hat{c}^\dagger_{i_1\sigma_n} \hat{c}_{i_1\sigma_1} \hat{c}^\dagger_{i_2\sigma_1} \hat{c}_{i_2\sigma_2} \ldots \hat{c}^\dagger_{i_n\sigma_{n-1}} \hat{c}_{i_n\sigma_n},\end{aligned} \tag{4.27}$$

as

$$\begin{aligned}\hat{H}^{(2)}_{\mathrm{SCE}}(t) &= -\sum_{n,m=-\infty}^{\infty} \sum_{ij} \frac{t_{i,j}^{(m-n)} t_{j,i}^{(n)}}{2(U-n\omega)} e^{-im\omega t} \sum_{\sigma_1,\sigma_2} \hat{c}^\dagger_{i\sigma_1} \hat{c}_{j\sigma_1} \hat{c}^\dagger_{j\sigma_2} \hat{c}_{i\sigma_2} + \mathrm{h.c.} \\ &= \sum_{n,m=-\infty}^{\infty} \sum_{ij} \mathrm{Re}\left[\frac{t_{i,j}^{(n)} t_{j,i}^{(m-n)}}{U-n\omega} e^{-im\omega t}\right] (\hat{P}_{ij} - 1),\end{aligned} \tag{4.28}$$

where we have used $\sum_\sigma \hat{c}^\dagger_{i\sigma} \hat{c}_{i\sigma} \equiv 1$. While the representation with a permutation operator is applicable to general SU(N) cases, in ordinary SU(2) case the two-spin permutation represents the exchange interaction

$$\hat{P}_{ij} - 1 = 2\left(\hat{\boldsymbol{S}}_i \cdot \hat{\boldsymbol{S}}_j - \frac{1}{4}\right), \tag{4.29}$$

where

$$\hat{\boldsymbol{S}}_i = \frac{1}{2} \sum_{\sigma_1\sigma_2} \hat{c}^\dagger_{i\sigma_1} \boldsymbol{\sigma}_{\sigma_1\sigma_2} \hat{c}_{i\sigma_2} \tag{4.30}$$

is the 1/2-spin operator on i-th site with the Pauli matrix $\boldsymbol{\sigma}$. With the explicit form of hopping amplitude, Eq. (4.8), we obtain the time-dependent Heisenberg interaction between i and j sites as

$$J_{i,j}(t) = \sum_{n,m=-\infty}^{\infty} (-1)^{m+1} \frac{4|t_{i,j}|^2 \mathscr{J}_{n+m}(A) \mathscr{J}_{n-m}(A)}{U-(n+m)\omega} \cos 2m(\omega t - \theta_{ij}), \tag{4.31}$$

and the spin Hamiltonian as

$$\hat{H}^{(2)}_{\mathrm{SCE}}(t) = -\sum_{\langle ij\rangle} J_{i,j}(t)\left(\hat{\boldsymbol{S}}_i \cdot \hat{\boldsymbol{S}}_j - \frac{1}{4}\right). \tag{4.32}$$

Then, if the driving frequency ω is much smaller than U, the high-frequency expansion for this time-dependent Heisenberg model should give a correction more important than the higher orders of the strong coupling expansion. By using an

identity,

$$[\hat{P}_{ij},\hat{P}_{jk}] = \hat{P}_{ijk} - \hat{P}^{\dagger}_{ijk}, \tag{4.33}$$

the Floquet effective Hamiltonian $\hat{F}$ for the spin degree of freedom is obtained as

$$\begin{aligned}\hat{F} &= \hat{H}^{(2)}_{\mathrm{SCE},0} - \sum_{m\neq 0} \frac{[\hat{H}^{(2)}_{\mathrm{SCE},m}, \hat{H}^{(2)}_{\mathrm{SCE},-m}]}{2m\omega} \\ &= -\frac{1}{4}\sum_{ij} J^{(0)}_{i,j}(\hat{P}_{ij}-1) - \sum_{m\neq 0}\sum_{ijk} \frac{J^{(m)}_{i,j} J^{(-m)}_{j,k}}{8m\omega}(\hat{P}_{ijk} - \hat{P}^{\dagger}_{ijk}).\end{aligned} \tag{4.34}$$

for the SU(2) case, the permutation can be expressed as a scalar chirality term as

$$\hat{P}_{ijk} - \hat{P}^{\dagger}_{ijk} = -4i(\hat{S}_i \times \hat{S}_j)\cdot \hat{S}_k. \tag{4.35}$$

Namely, the effective spin Hamiltonian,

$$\hat{F} = -\sum_{\langle ij\rangle} J^{(0)}_{i,j}\left(\hat{S}_i\cdot\hat{S}_j - \frac{1}{4}\right) + \sum_{\langle ijk\rangle} J^{(\mathrm{h})}_{\chi\langle i,j,k\rangle}(\hat{S}_i\times\hat{S}_j)\cdot\hat{S}_k, \tag{4.36}$$

is composed of the exchange interaction

$$J^{(0)}_{i,j} = -\sum_{m=-\infty}^{\infty} \frac{4|t_{i,j}|^2 \mathscr{J}^2_m(A)}{U - m\omega}, \tag{4.37}$$

and the chiral coupling $J^{(\mathrm{h})}_{\chi\langle i,j,k\rangle} = J^{(\mathrm{h})}_{\chi i,j,k} + J^{(\mathrm{h})}_{\chi k,i,j} + J^{(\mathrm{h})}_{\chi j,k,i}$ with

$$\begin{aligned}J^{(\mathrm{h})}_{\chi i,j,k} &= \sum_{m\neq 0} \frac{i J^{(m)}_{i,j} J^{(-m)}_{j,k}}{m\omega} \\ &= -\sum_{m=1}^{\infty} \frac{16}{m\omega}\left[\sum_{n=-\infty}^{\infty} \frac{U\mathscr{J}_{n+m}(A)\mathscr{J}_{n-m}(A)}{U^2-(n+m)^2\omega^2}\right]^2 |t_{i,j}|^2|t_{j,k}|^2 \sin 2m(\theta_{ij}-\theta_{jk}).\end{aligned} \tag{4.38}$$

Here, we note that the chiral coupling emerges as a nonlinear response; we can see that the term is nonlinear by expanding the expression in $A = E/\omega$ to obtain

$$J^{(\mathrm{h})}_{\chi i,j,k} = -\frac{|t_{i,j}|^2|t_{j,k}|^2(U^2+2\omega^2)^2}{\omega U^2(U^2-\omega^2)^2(U^2-4\omega^2)^2} E^4 \sin 2(\theta_{ij}-\theta_{jk}) + \mathscr{O}(E^6). \tag{4.39}$$

In contrast, the fourth order contribution of the strong-coupling expansion turns out to have a term proportional to E^2 as we shall see below.

4.2.3 Fourth-order perturbation

Let us move on to higher orders in the strong-coupling expansion to examine the cases where $\omega \ll U$ is not satisfied. Let us start with the third-order terms as

$$\hat{H}^{(3)}_{\mathrm{SCE}}(t) = \sum_{l,n,m=-\infty}^{\infty} \Big[\sum_{c,d\neq 0} \frac{[[\hat{T}_{c,l}, \hat{T}_{d-c,n-l}], \hat{T}_{-d,m-n}]}{4(cU - l\omega)(dU - n\omega)} (1+\delta_{d-c}) + \sum_{c\neq 0} \sum_{d\neq 0,-c} \frac{[\hat{T}_{c,l}, [\hat{T}_{d,n}, \hat{T}_{-c-d,m-n-l}]]}{12(cU - l\omega)(dU - n\omega)} \Big] e^{-im\omega t}, \tag{4.40}$$

$$i\hat{S}^{(3)}(t) = \sum_{l,n,m=-\infty}^{\infty} \sum_{b,c\neq 0} \Big[\sum_{d\neq 0,b+c} \frac{[\hat{T}_{b,l}, [\hat{T}_{c,n}, \hat{T}_{d-c-b,m-n-l}]]}{12(bU - l\omega)(cU - n\omega)(dU - m\omega)} (1+3\delta_{b-d}) + \sum_{d\neq 0} \frac{[[\hat{T}_{b,l}, \hat{T}_{c-b,n-l}], \hat{T}_{d-c,m-n}]}{4(bU - l\omega)(cU - n\omega)(dU - m\omega)} (1+\delta_{c-b})(1+\delta_{c-d}) \Big] e^{-im\omega t}, \tag{4.41}$$

The projection onto $\hat{D} = 0$ yields

$$\hat{H}^{(3)}_{\mathrm{SCE}}(t) = \sum_{l,n,m=-\infty}^{\infty} \frac{\hat{T}_{-1,m-n} \hat{T}_{0,n-l} \hat{T}_{+1,l}}{2(U - l\omega)(U - n\omega)} e^{-im\omega t} + \mathrm{h.c.}. \tag{4.42}$$

Here, a term $\hat{T}_{-1}\hat{T}_0\hat{T}_{+1}$ can be diagrammatically represented as Figs. 4.5(b) and 4.5(c), so that we have

$$\begin{aligned} \hat{H}^{(3)}_{\mathrm{SCE}}(t) = &- \sum_{l,n,m=-\infty}^{\infty} \sum_{ijk} \frac{t^{(m-n)}_{j,i} t^{(n-l)}_{i,k} t^{(l)}_{k,j}}{2(U - l\omega)(U - n\omega)} e^{-im\omega t} + \mathrm{h.c.} \\ &+ \sum_{l,n,m=-\infty}^{\infty} \sum_{ijk} \frac{t^{(m-n)}_{j,i} t^{(n-l)}_{i,k} t^{(l)}_{k,j}}{2(U - l\omega)(U - n\omega)} \left[\hat{P}_{jk} + \hat{P}_{ij} + (-1)^m \hat{P}_{ki} \right] e^{-im\omega t} + \mathrm{h.c.} \\ &- \sum_{l,n,m=-\infty}^{\infty} \sum_{ijk} \frac{t^{(m-n)}_{j,i} t^{(n-l)}_{i,k} t^{(l)}_{k,j}}{2(U - l\omega)(U - n\omega)} [\hat{P}_{ijk} + (-1)^m \hat{P}^{\dagger}_{ijk}] e^{-im\omega t} + \mathrm{h.c.} \end{aligned} \tag{4.43}$$

where we have used a relation $t^{(m)}_{j,i} = (-1)^m t^{(m)}_{i,j}$. This result shows that the scalar chirality term $\propto (\hat{P}_{ijk} - \hat{P}^{\dagger}_{ijk})$ vanishes in the time average.

On the other hand, if we turn to the fourth-order contribution, the time average

is given as

$$\overline{\hat{H}^{(4)}_{\mathrm{SCE}}(t)} = \sum_{l,n,m=-\infty}^{\infty} \sum_{b,c\neq 0} \Big[\sum_{d\neq 0,c} \frac{[[\hat{T}_{-b,-l},\hat{T}_{b-c,l-n}],[\hat{T}_{d,m},\hat{T}_{c-d,n-m}]]}{24(bU-l\omega)(cU-n\omega)(dU-m\omega)}(1+\delta_{c-b})$$
$$- \sum_{d\neq 0} \frac{[[[\hat{T}_{b,l},\hat{T}_{c-b,n-l}],\hat{T}_{-d-c,-m-n}],\hat{T}_{d,m}]}{12(bU-l\omega)(cU-n\omega)(dU-m\omega)}(1+\delta_{c-b})(2+\delta_{c+d})$$
$$- \sum_{d\neq 0} \frac{[[[\hat{T}_{b,l},\hat{T}_{d-c-b,m-n-l}],\hat{T}_{c,n}],\hat{T}_{-d,-m}]}{24(bU-l\omega)(cU-n\omega)(dU-m\omega)}(1-\delta_{d-c-b}+2\delta_{d-c})\Big], \tag{4.44}$$

and with its projection onto $\hat{D}=0$,

$$\overline{\hat{H}^{(4)}_{\mathrm{SCE}}(t)} = \sum_{l,n,m=-\infty}^{\infty} \Big[-\frac{\hat{T}_{-1,-l}\hat{T}_{0,l-n}\hat{T}_{0,n-m}\hat{T}_{+1,m}}{2(U-l\omega)(U-n\omega)(U-m\omega)} + \frac{\hat{T}_{-1,-l}\hat{T}_{+1,n}\hat{T}_{-1,-m}\hat{T}_{+1,l-n+m}}{8(U-l\omega)(U-n\omega)(U-m\omega)}$$
$$+ 3\frac{\hat{T}_{-1,-l}\hat{T}_{+1,n}\hat{T}_{-1,l-n-m}\hat{T}_{+1,m}}{8(U-l\omega)(U-n\omega)(U-m\omega)} \Big] + \mathrm{h.c.}. \tag{4.45}$$

Here, $\hat{T}_{-1}\hat{T}_0\hat{T}_0\hat{T}_{+1}$ and $\hat{T}_{-1}\hat{T}_{+1}\hat{T}_{-1}\hat{T}_{+1}$ are respectively decomposed diagrammatically as Figs. 4.5(d)-4.5(g) and doubled Fig. 4.5(a), and they contribute to the chiral coupling $J^{\chi(\mathrm{s})}_{\langle i,j,k\rangle} = J^{\chi(\mathrm{s})}_{i,j,k} + J^{\chi(\mathrm{s})}_{k,i,j} + J^{\chi(\mathrm{s})}_{j,k,i}$ as

$$J^{(\mathrm{s})}_{\chi i,j,k} = -8|t_{i,j}|^2|t_{j,k}|^2 \sum_{l,n,m=-\infty}^{\infty} \Big[\frac{\mathscr{J}_l(A)\mathscr{J}_n(A)\mathscr{J}_{l+m}(A)\mathscr{J}_{n+m}(A)}{(U-l\omega)(U-n\omega)(U-(l+n+m)\omega)} \sin m(\theta_{ij}-\theta_{jk})$$
$$+ \frac{\mathscr{J}_{l+m}(A)\mathscr{J}_{l-m}(A)\mathscr{J}_{n+m}(A)\mathscr{J}_{n-m}(A)}{(U-(l-m)\omega)(U-(l+m)\omega)(U-(n+m)\omega)} \sin 2m(\theta_{ij}-\theta_{jk})\Big]. \tag{4.46}$$

This contrasts with the result obtained in the high-frequency expansion, Eq. (4.38) $\sim \mathscr{O}(E^4)$, in the previous subsection, since the small amplitude expansion of this expression reads

$$J^{(\mathrm{s})}_{\chi i,j,k} = \frac{4|t_{i,j}|^2|t_{j,k}|^2\omega(7U^2-3\omega^2)}{U^2(U^2-\omega^2)^3}\sin(\theta_{ij}-\theta_{jk})E^2 + \mathscr{O}(E^4), \tag{4.47}$$

which is quadratic in the field strength E.

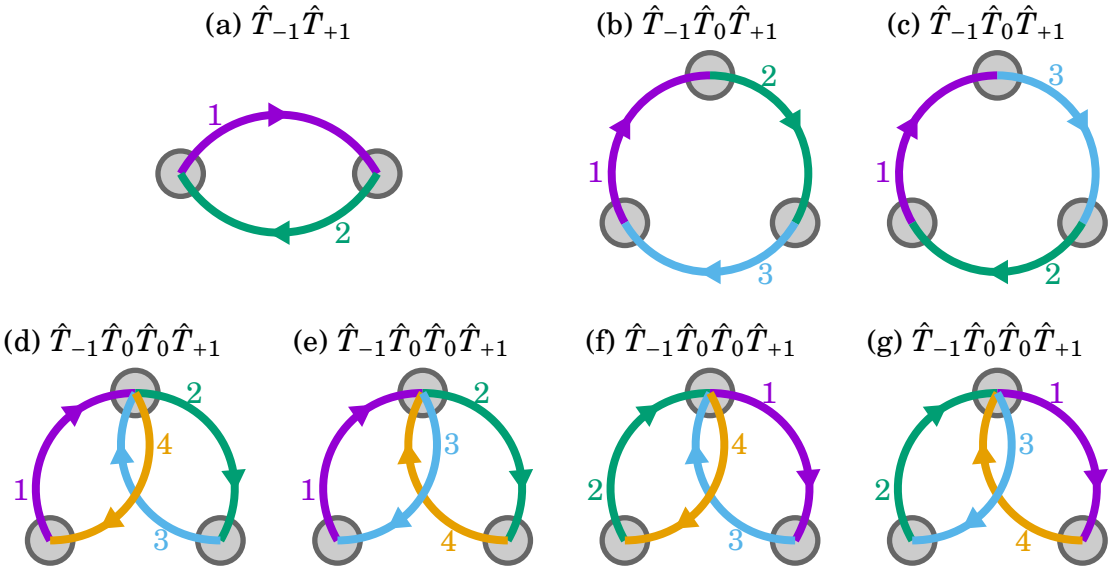

Figure 4.5: Diagrammatic representation of the virtual processes in the strong-coupling expansion. The gray circles represent sites, while arrows represent hopping of electrons. Numbers represent the order of the hopping process. These exhaust all the hopping patterns for $\hat{T}_{-1}\hat{T}_{+1}$, $\hat{T}_{-1}\hat{T}_{0}\hat{T}_{+1}$, and $\hat{T}_{-1}\hat{T}_{0}\hat{T}_{0}\hat{T}_{+1}$ up to diagrams obtained by site permutations.

Finally we obtain the Floquet effective Hamiltonian as[3]

$$\hat{F} = -\sum_{\langle ij\rangle} J^{(0)}_{i,j}\left(\hat{S}_i\cdot\hat{S}_j - \frac{1}{4}\right) + \sum_{\langle ijk\rangle}(J^{(\mathrm{h})}_{\chi\langle i,j,k\rangle} + J^{(\mathrm{s})}_{\chi\langle i,j,k\rangle})(\hat{S}_i\times\hat{S}_j)\cdot\hat{S}_k. \tag{4.48}$$

4.3 Discussions and applications

4.3.1 Validity of the expansion and behavior of the spin couplings

Let us discuss the validity of the strong-coupling expansion obtained in this subsection. The effective low-energy Hamiltonian is characterized by two parameters, the Heisenberg exchange interaction J and the chiral coupling J_χ. They scale, in the leading order, as $J \propto U^{-1}$ from Eq. (4.37) and $J_\chi \propto U^{-3}$ from Eqs. (4.38) and (4.46) for a fixed ω/U.

Here we consider three sites arranged as an equilateral triangle for simplicity,

[3]The same expression is also obtained for Heisenberg term in Ref. [98], and for the chiral term in Ref. [108] recently.

and compare the expansion for this system and the numerical values of J and J_χ determined from the numerical exact calculation for the driven three-site Hubbard model. The obtained values of parameters with rescaling UJ and $U^3 J_\chi$ for various values of ω/U are shown in Fig. 4.6. In all cases, one can see that the agreement between the numerical result and the perturbative calculation becomes better for stronger U, which confirms the correctness of the expansion.

A crucial interest is the behavior of the chiral coupling J_χ for different values of ω/U here. As we mentioned in Sec. 4.1, the periodically-driven Hubbard model on a honeycomb lattice approximates the Haldane-Hubbard model in the high-frequency regime $U \ll \omega$, and is studied numerically. However, as Figs. 4.6(g), 4.6(h) shows, the chiral coupling in this regime ($\omega = 2U$) is relatively small, while the region where ω and U are comparable [Fig. 4.6(a)-4.6(f)], the significant enhancement of the chiral coupling occurs. We note that the required U for the justification of the expansion depends on ω/U, so that we have to refer to different values of U if we want to compare converged results, where we have to take account of the rescaling. Indeed, the required U is larger in the intermediate regime: While $U = 10$ is sufficient for the $U \ll \omega$ case, this may not reproduce even qualitative results when U and ω are the comparable.

One can notice discontinuous jumps in the spin couplings in the $U = 10$ cases in Fig. 4.6, which implies a breakdown of the strong-coupling expansion. Indeed, the quasienergy spectra plotted in Fig. 4.7 show that the level crossing between $D = 0$ and $D = 1$ sectors occurs at $A \sim 1$ in the $U = 10$ case. Here, while for the effective Hamiltonian after the strong-coupling expansion D takes integers, Fig. 4.7 shows the time average of $\langle \hat{D}(t) \rangle$ for the Hubbard model calculated with Eq. (2.64).In these spectra, the chiral spin coupling exerts its effect as a splitting of lower energy levels around $\epsilon \simeq -0.6$ in Fig. 4.7(a) and $\epsilon \simeq -0.3$ in Fig. 4.7(b) in the $D = 0$ sector as A is increased from zero, which is remarkably large in the $U = 10$ case. However, the picture of atomic-limit-like electrons should be broken down when the perturbation breaks down, so that the result for a finite (three-site) system should deviate form those in bulk systems.

The adiabatic connection of the $D = 0$ and $D = 1$ sectors may give a lower bound for the region where the strong-coupling expansion describes qualitatively correct results. The boundary for the occurrence of this adiabatic connection in the three-site Hubbard model is plotted in Fig. 4.8.

4.3.2 Chiral spin liquid

The enhancement of the chiral coupling in the intermediate regime $\omega \sim U$ observed in the previous subsection urges us to ask ourselves whether we can realize the chiral

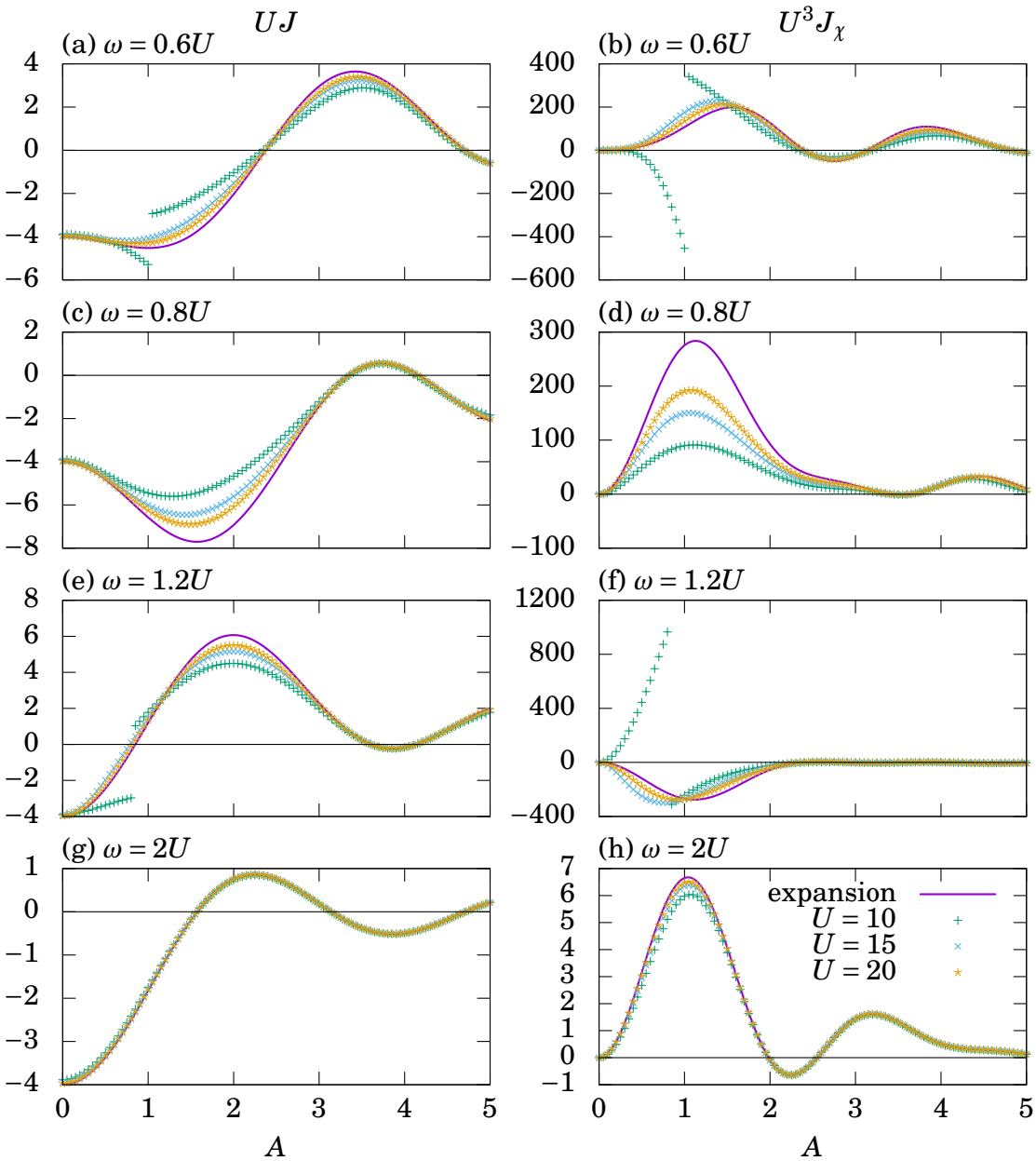

Figure 4.6: (a), (c), (e), (g) The Heisenberg exchange interaction J and (b), (d), (f), (h) the chiral coupling J_χ for various ω/U. Values are rescaled with U and U^3 for J and J_χ, respectively. The solid lines are the perturbative expression obtained in the text, and points are the exact numerical results for the three-site Hubbard model.

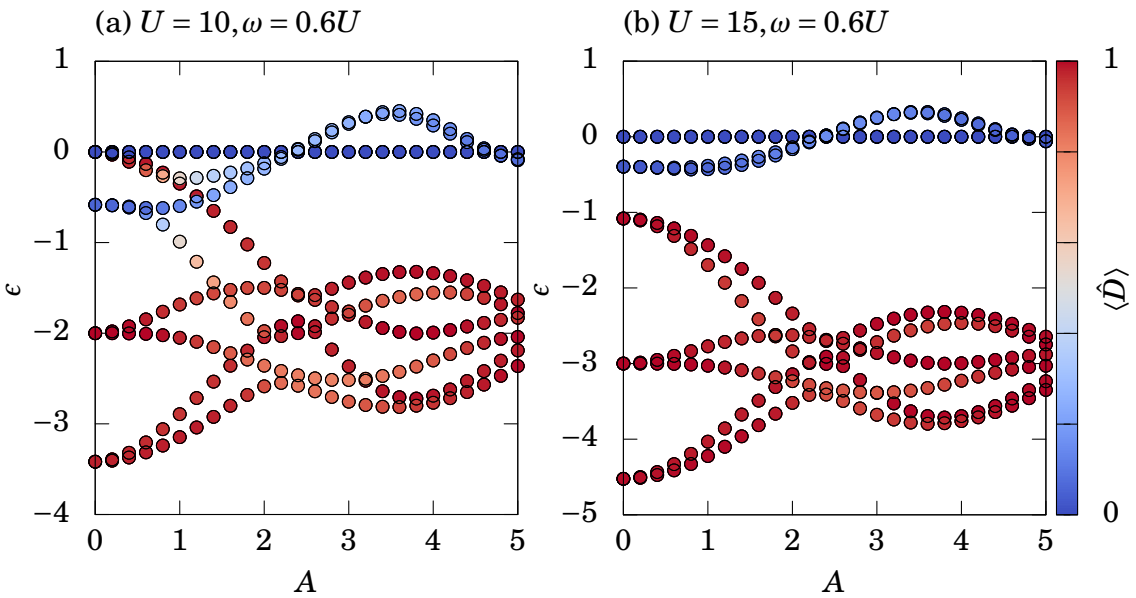

Figure 4.7: Quasienergy spectra against A for the three-site Hubbard model driven by a circularly-polarized laser for (a) $U = 10$, $\omega = 0.6U = 6$ and (b) $U = 15$, $\omega = 0.6U = 9$. Color represents the time average of the expectation value of the double occupancy $\hat{D}$ for each quasienergy eigenstate.

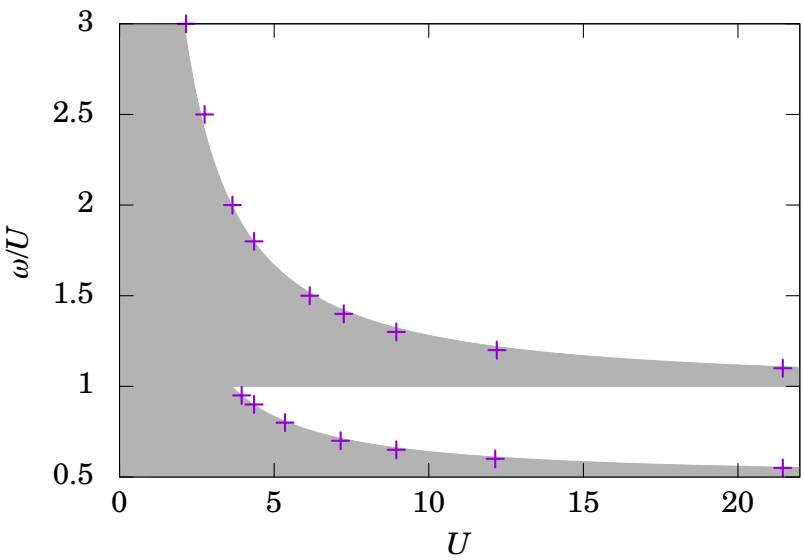

Figure 4.8: Region (shaded) where the adiabatic connection between $D = 0$ and $D = 1$ sectors emerges in the three-site Hubbard model (i.e., the strong-coupling expansion invalidated). Crosses represent the numerical result, while gray hatching delineates fitted form as $2\omega - U = 5U^{-1/4}$ and $\omega - U = 5U^{-1/4}$.

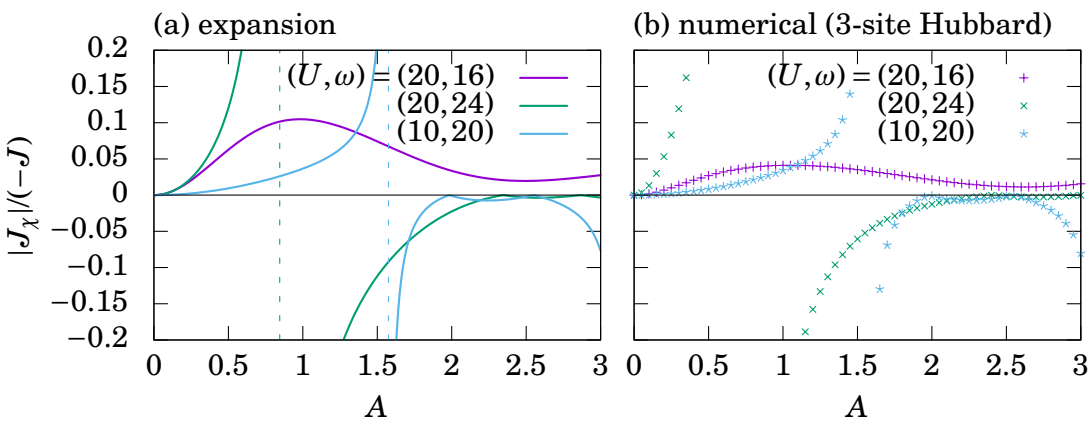

Figure 4.9: The ratio $|J_\chi|/(-J)$ between the chiral coupling and exchange interaction (a) calculated with the strong-coupling expansion, or (b) numerically for the three-site Hubbard model, for indicated values of (U,ω).

spin liquid. To explore this, we plot the ratio between the chiral coupling and the exchange interaction in Fig. 4.9. To simply magnify the value of the ratio, one can exploit the zeros of the exchange interaction as a function of A.

The critical ratio for the chiral spin liquid phase is estimated as $|J_\chi|/(-J) \gtrsim 0.16$ for the Kagomé lattice [104] for instance. While a fine tuning of A is necessary for the $(U,\omega) = (10,20)$ case, the critical ratio can be achieved in a broad region in the $(U,\omega) = (20,24)$ case.

Although the ratio for the $(U,\omega) = (20,16)$ case is much smaller than the critical value, a recent study [108] reports that the effective spin Hamiltonian for the Kagomé Hubbard model under a circularly-polarized laser for the values of parameters similar to $(U,\omega) = (20,16)$ has the chiral spin liquid as a ground state. While the chiral spin liquid (or the fractional Chern insulator) is characterized by the degeneracy of the ground state or the fractional statistics of excitations, how to characterize the nonequilibrium steady state realized for the effective Hamiltonian with such a ground state should be discussed carefully in future works, including how to detect the nonequilibrium chiral spin liquid experimentally.

4.3.3 Probe for scalar spin chirality

While the spin chirality provides nontrivial topological phenomena as we have mentioned, an important concept we obtained in the above is that the spin chirality directly couples with the circularly-polarized laser. This implies that, conversely, the existence of the chiral spin order in Mott insulators should be fingerprinted in the optical response for a circularly-polarized laser. Thus we propose here to discuss

influences of the spin degree of freedom on the optical response of Mott insulators.

To this end, let us evaluate the dielectric function of the present system [106]. The dielectric function is generally calculated as

$$\epsilon_{\mu\nu}(\omega) = \epsilon_0\delta_{\mu\nu} + \sum_{\alpha\alpha'} \frac{e^{-\beta E_\alpha} - e^{-\beta E_{\alpha'}}}{2Z} \frac{\langle\alpha|\hat{P}_\mu|\alpha'\rangle\langle\alpha'|\hat{P}_\nu|\alpha\rangle}{\omega + E_\alpha - E_{\alpha'} + i\delta} \tag{4.49}$$

with the Kubo formula. Here E_α and $|\alpha\rangle$ are respectively an eigenenergy and an eigenstate of the undriven Hubbard model, $Z = \sum_n e^{-\beta E_\alpha}$ the partition function, β the inverse temperature and $\hat{\boldsymbol{P}} = \sum_i \hat{n}_i \boldsymbol{R}_i$ the polarization. Here we denote undriven Hamiltonian as $\hat{H}_{\mathrm{u}} = \hat{H}(A = 0)$. Then we define

$$\hat{T} \equiv -\sum_{ij\sigma} t_{i,j}\hat{c}^\dagger_{i\sigma}\hat{c}_{j\sigma}, \tag{4.50}$$

$$\hat{T}^\mu \equiv [\hat{P}_\mu, \hat{H}_{\mathrm{u}}] = -\sum_{ij\sigma} t_{i,j}(R_{i\mu} - R_{j\mu})\hat{c}^\dagger_{i\sigma}\hat{c}_{j\sigma}, \tag{4.51}$$

$$\hat{T}^{\mu\nu} \equiv [\hat{P}_\mu, [\hat{P}_\nu, \hat{H}_{\mathrm{u}}]] = -\sum_{ij\sigma} t_{i,j}(R_{i\mu} - R_{j\mu})(R_{i\nu} - R_{j\nu})\hat{c}^\dagger_{i\sigma}\hat{c}_{j\sigma}, \tag{4.52}$$

and again consider the decomposition with respect to the double occupancy, such as $\hat{T} = \hat{T}_{+1} + \hat{T}_0 + \hat{T}_{-1}$, and perform the strong-coupling expansion with the transformation Eq. (4.10) at $A = 0$, which we denote $e^{i\hat{S}_0}$ here. The n-th eigenstates for the expanded Hamiltonian can be labeled with double occupancy d as $|n,d\rangle$, and satisfies $|n,d\rangle = e^{i\hat{S}_0}|\alpha\rangle$ and $E_\alpha = E'_{n,d} + dU$, where $E'_{n,d}$ is the eigenenergy of the effective Hamiltonian.

Then one can rewrite the dielectric function as

$$\begin{aligned}\epsilon_{\mu\nu}(\omega) = \epsilon_0\delta_{\mu\nu} &- \sum_n \frac{e^{-\beta E'_{n,0}}}{2Z\omega^2}\langle n,0|e^{i\hat{S}_0}\hat{T}^{\mu\nu}e^{-i\hat{S}_0}|n,0\rangle \\ &- \sum_{nn'd} \frac{e^{-\beta E'_{n,0}}}{2Z\omega^2}\Bigg[\frac{\langle n,0|e^{i\hat{S}_0}\hat{T}^\mu e^{-i\hat{S}_0}|n',d\rangle\langle n',d|e^{i\hat{S}_0}\hat{T}^\nu e^{-i\hat{S}_0}|n,0\rangle}{\omega - dU + E'_{n,0} - E'_{n',d} + i\delta} \\ &\qquad - \frac{\langle n,0|e^{i\hat{S}_0}\hat{T}^\nu e^{-i\hat{S}_0}|n',d\rangle\langle n',d|e^{i\hat{S}_0}\hat{T}^\mu e^{-i\hat{S}_0}|n,0\rangle}{\omega + dU - E'_{n,0} + E'_{n',d} + i\delta}\Bigg].\end{aligned} \tag{4.53}$$

Here we have assumed that $e^{-\beta U}$ is negligibly small. The lowest-order contribution

in the strong-coupling expansion yields

$$\begin{aligned}\epsilon^{(1)}_{\mu\nu}(\omega) &= \sum_n \frac{e^{-\beta E'_{n,0}}}{2Z\omega^2}\langle n,0|\left[\frac{\hat{T}_{-1}\hat{T}^{\mu\nu}_{+1}+\hat{T}^{\mu\nu}_{-1}\hat{T}_{+1}}{U}+\frac{\hat{T}^{\mu}_{-1}\hat{T}^{\nu}_{+1}}{U-\omega}+\frac{\hat{T}^{\nu}_{-1}\hat{T}^{\mu}_{+1}}{U+\omega}\right]|n,0\rangle \\ &= \sum_{ij}\frac{2|t_{i,j}|^2}{U(U^2-\omega^2)}(R_{i\mu}-R_{j\mu})(R_{i\nu}-R_{j\nu})\left(\langle\hat{\boldsymbol{S}}_i\cdot\hat{\boldsymbol{S}}_j\rangle_{\rm th}-\frac{1}{4}\right),\end{aligned} \tag{4.54}$$

where $\langle\bullet\rangle_{\rm th} = Z^{-1}\sum_n e^{-\beta E_{n,0}}\langle n,0|\bullet|n,0\rangle$. Similarly, the leading-order contribution from the scalar spin chirality is calculated as

$$\epsilon^{(\chi)}_{\mu\nu}(\omega) = \sum_{ijk}\frac{4i\epsilon_{\mu\nu}|t_{i,j}|^2|t_{j,k}|^2\omega(7U^2-3\omega^2)}{U^2(U^2-\omega^2)^3}\mathscr{A}_{ijk}\left\langle(\hat{\boldsymbol{S}}_i\times\hat{\boldsymbol{S}}_j)\cdot\hat{\boldsymbol{S}}_k\right\rangle_{\rm th}, \tag{4.55}$$

where $\mathscr{A}_{ijk}\equiv[(\boldsymbol{R}_i-\boldsymbol{R}_k)\times(\boldsymbol{R}_j-\boldsymbol{R}_k)]_z/2 = -\mathscr{A}_{jik}$ is the area of the triangle enclosed by sites i,j,k.

The sum of these contributions yields an expression for the dielectric function,

$$\begin{aligned}\epsilon(\omega) &= \begin{pmatrix}\epsilon_{xx} & \epsilon_{xy}\\ \epsilon_{yx} & \epsilon_{yy}\end{pmatrix} \\ &= \begin{pmatrix}\epsilon_0 & 0\\ 0 & \epsilon_0\end{pmatrix}+\sum_{ij}\frac{2|t_{i,j}|^2}{U(U^2-\omega^2)}\left(\langle\hat{\boldsymbol{S}}_i\cdot\hat{\boldsymbol{S}}_j\rangle_{\rm th}-\frac{1}{4}\right)\begin{pmatrix}(x_i-x_j)^2 & (x_i-x_j)(y_i-y_j)\\ (x_i-x_j)(y_i-y_j) & (y_i-y_j)^2\end{pmatrix} \\ &\quad -\sum_{ijk}\frac{4|t_{i,j}|^2|t_{j,k}|^2\omega(7U^2-3\omega^2)}{U^2(U^2-\omega^2)^3}\left\langle(\hat{\boldsymbol{S}}_i\times\hat{\boldsymbol{S}}_j)\cdot\hat{\boldsymbol{S}}_k\right\rangle_{\rm th}\begin{pmatrix}0 & -i\mathscr{A}_{ijk}\\ i\mathscr{A}_{ijk} & 0\end{pmatrix},\end{aligned} \tag{4.56}$$

and one can see the emergent imaginary off-diagonal part only in the presence of the spin chirality order. This should result in a circular dichroism, namely a difference in the reflectivity emerges in right- and left- circularly-polarized lasers (i.e., for different spin angular momenta for photons). This is a key observation in this subsection. Here we note that the coefficient of the chiral contribution to the dielectric function coincide with that of Eq. (4.47).

4.3.4 Probe for vector spin chirality

While the circularly-polarized laser couples with the scalar chirality, systems having no scalar chirality can respond to laser due to cooperative effects involving other magnetic orders. Specifically, we can show that in the presence of uniform vector chirality [see Figs. 4.3(c)], the circularly-polarized laser induces a magnetization, i.e., the inverse Faraday effect: In the presence of the vector chirality, $\boldsymbol{S}_i\times\boldsymbol{S}_j$ has a finite expectation value, so that $J_\chi(\boldsymbol{S}_i\times\boldsymbol{S}_j)\cdot\boldsymbol{S}_k$ can be seen as a Zeeman field in a

mean-field sense.

However, we remark that here we have neglected the in-plane oscillating magnetic field due to the laser. This magnetic field is shown to act as a Zeeman field along z-axis in the Floquet effective Hamiltonian [109, 110]. While these contributions are expected to be distinguished by, e.g., a frequency or temperature dependence, this should be elaborated in future works.

4.4 Summary of Chapter 4

In this chapter, we have first formulated the strong-coupling expansion for the Hubbard model in the presence of periodic driving. We have then applied the formalism to reveal that the scalar spin chirality term emerges driven by a circularly-polarized laser[4]. While the chiral coupling emerges in the high-frequency regime via complex hopping induced by the periodic driving, we found that a significant enhancement of the coupling occurs in the intermediate regime $\omega \sim U$ as well. This can make the Floquet effective Hamiltonian possess a nontrivial ground state, the chiral spin liquid, as numerically shown in a recent study [108].

A candidate material for a possible application of the present discussion is, e.g., the herbertsmithite $ZnCu_3(OH)_6Cl_2$ [111], which is a mineral known as a Kagomé antiferromagnet. Ref. [112] estimates properties of the Ga-substituted compound $GaCu_3(OH)_6Cl_2$, which read $t_{ij} \sim 0.3$ eV and $U \sim 5$-7 eV. These yield $U/t \sim 17$-23, which is suitable for the present discussion. We note that the required driving frequency is high in an experimental sense, while it is lower than that required for the conventional high-frequency expansion [sketched in Fig. 4.4(b)].

We have also proposed that one can use the circularly-polarized laser as a probe of the spin chirality via the chiral coupling revealed here, which implies that the uniform scalar and vector chiralities can be detected from the reflectivity and magnetization, respectively.

There remain diverse directions for future works. Various spin systems with an additional chiral coupling term may be one interesting direction, which should be feasible using periodic driving. Another is to improve the feasibility of the chiral spin liquid. While the chiral coupling can reach the critical value for the chiral spin liquid phase in some cases, it is still small and may be washed out due to various obstacles not considered here; such as temperature or heating effects, and the magnetic component of the laser field. Applying the discussion on the SU(N) Hubbard model is one of the interesting route for a future work in this context, since the scalar chirality becomes more relevant for larger N, and eventually the chiral spin liquid

[4]The same expression for the chiral coupling has been independently been obtained in Ref. [108].

should emerge spontaneously as shown in Ref. [113]. The strong-coupling expansion formulated above, which is represented with permutation operators, can be directly applicable to the SU(N) case. Also, the $N \to \infty$ limit can be solved exactly using the slave-rotor mean-field theory [102], so that its extension to periodically-driven systems would be useful. The SU(N) Hubbard model can actually be implemented in cold-atom systems with e.g., Ytterbium atoms for $N = 6$ [114]. While how to detect the chiral spin liquid in this system should be discussed, it is one of strong candidates for experimental systems.

Chapter 5

Floquet η-pairing superconductivity

In this chapter, we extend our study for periodically-driven interacting systems to an attractively-interacting systems, where we show that an interplay with a driving field can produce novel states even for an ordinary s-wave superconductivity [115]. Namely, here the central interest is the fate of a system that is already superconducting when a periodic driving is turned on. In particular we focus on a strong attractive interaction, and reveal an emergence under the periodic driving of the exotic η-pairing superconductivity, which is long sought-after but eluded realization. We also discuss how we can make the system evolve toward a desired effective ground state when the dissipation is absent as in cold-atom systems, where we analyze a stability of the equation of motion for the condensate and exploit the dynamical instability.

5.1 Motivation

A nontrivial consequence of attractive interactions is the superconductivity, where electrons form Cooper pairs and show superfluidity, as the Bardeen-Cooper-Schrieffer theory has revealed [116–118]. Since originally electrons interact repulsively, some mechanisms to induce an effective attraction between electrons are required for an emergence of superconductivity. While superconductors discovered in earlier days have an effective interaction mediated by phonons as an origin of the superconductivity, high-T_c superconductors such as the cuprates are considered to have spin fluctuations as an origin. Such an origin of the attractive interaction is reflected in the nature of superconductors, especially on the pairing symmetry. There are a variety of forms of pairing symmetry, such as the relative orbital angular momen-

tum, spin state, and the total momentum. The strength of the attractive interaction also affects the properties of pairing; while the pairing occurs in momentum space for weak attractions, it changes to a real-space pairing as molecular bosons when the interaction is increased, which is known as the BCS-BEC crossover [119, 120] and observed experimentally in ultracold atom systems [121, 122].

From a viewpoint of the present thesis, we are interested in the superconducting phenomena peculiar to nonequilibrium conditions. In this context, it is a most important question to ask whether we can induce a superconducting order by driving the system. Seminal experimental works [4–6] report some evidences of superconductivity above the equilibrium critical temperature by driving phonon modes in a coherent manner, both in s- and d-wave superconductors. While these results attract much interest, whether the reported phenomena are really derived from superconductivity is not established, and a microscopic theory for these phenomena is also lacking at present. A possibility of the photo-induced superconductivity is also discussed in theoretical works. One of proposals [123] shows that the periodic driving which flips the effective band structure turns out to invert repulsive interactions into attractive ones in isolated lattice systems.

Behaviors of superconductors themselves under external fields are also an interesting problem. A significant contribution to the dynamics of superconductors can be provided by the Higgs mode, a collective excitation as an amplitude mode of the superconducting order parameter. While the Higgs mode does not couple with electromagnetic fields within a linear response, a resonant excitation of the Higgs mode as a nonlinear effect is observed experimentally and analyzed theoretically [124].

While the periodic driving can be exploited to excite systems coherently, as we have discussed above in the present thesis, it also has a possibility for realizing nonequilibrium steady states distinct from the equilibrium ones. There are a variety of interests on influences of the periodic driving on superconducting states. For example, superconductivity mediated by spin fluctuations would also be modified significantly, since the spin degree of freedom is also strongly affected by the driving electric field as we have seen in the previous chapter. On the other hand, under the periodic driving, whether attractively-interacting electrons form Cooper pairs in an ordinary way or not should be examined afresh as a nonequilibrium problem, especially for the pairing symmetries. Hence here we pose questions such as,

- Are there any pairing mechanisms or symmetries peculiar to nonequilibrium phenomena?

- Are there any nonequilibrium phenomena arising from attractive interactions that are in principle absent in repulsive systems?

As answers to these questions, in this chapter, we shall reveal an emergence of the so-called η-pairing superconductivity [125] under a periodic driving. The η pairing states are originally proposed by Yang as a series of exact eigenstates of the Hubbard model [125], which is a high-energy superconducting state with a maximal (Brillouin-zone corner) total momentum of a Cooper pair. While the exotic pairing has eluded realization so far, here we seek a nonequilibrium possibility of realizing this pairing within the attractive Hubbard model,

$$\hat{H}_{\mathrm{att}}(t) = -\sum_{ij\sigma} t_{i,j}(t)\hat{c}^{\dagger}_{i\sigma}\hat{c}_{j\sigma} - U\sum_{i}\left(\hat{n}_{i\uparrow} - \frac{1}{2}\right)\left(\hat{n}_{i\downarrow} - \frac{1}{2}\right). \tag{5.1}$$

Namely, here we focus on the influence of the periodic field on a formation of Cooper pairs, rather than the mechanism for inducing an attractive interaction to electrons.

From a symmetry viewpoint, the Hubbard model has, on top of the ordinary spin-SU(2) symmetry, a hidden η-SU(2) symmetry at half filling [126], which is especially important in considering an attractive case. Due to this symmetry, one can map the attractive model to a repulsive one as far as equilibrium states are concerned. While this may seems to exclude an existence of physics peculiar to attractive systems even in nonequilibrium, the periodic driving turns out to destruct this symmetry and make the behavior of attractive systems totally different from the repulsive ones, as we shall see in Sec. 5.2. This difference is particularly reflected in the low-energy degree of freedom in the strong-coupling regime, so that we shall apply the strong-coupling expansion we have formulated in Chapter 4 to the attractive case, and discuss the effective Hamiltonian and accompanying ground states in Sec. 5.3. As a consequence, a band flip for the band structure as molecular bosons occurs, which actually turns the ground state from ordinary s-wave superconductivity into the η-pairing one.

On the other hand, for the realization of the η-pairing state, it is insufficient to show the change of the ground state, especially for isolated systems. The best candidate for realizing the strong-coupling regime of the attractive Hubbard model is cold atoms on an optical lattice, which behaves as an isolated system without energy dissipation, so that this becomes an important point for the present proposal. In isolated systems, systems do not relax to the ground state due to the energy conservation. This is indeed a cause for nontrivial phenomena like the conversion of the repulsive interaction into attraction [123]. Thus we first discuss the stability of an s-wave conducting initial state under the effective Hamiltonian in Sec. 5.4, by employing an analogy with the Gross-Pitaevskii equation for Bose-Einstein condensates [127].

The stability analysis reveals that, due to the broken η-SU(2) symmetry, an instability not accompanied by the dissipation, called dynamical instability, does emerge even in isolated systems. While this instability for the s-wave superconductivity

does not directly lead to the η pairing but to a charge-ordered state, one can actually induce the η-pairing superconductivity via a transition to a charge-ordered state by changing the driving amplitude in designated ways.. We examine this idea in Sec. 5.5, by computing a time evolution numerically for two different protocols for the variation of the driving amplitude.

5.2 η-SU(2) symmetry and η-pairing

Before analyzing the attractive Hubbard model, here we notice an important symmetry inherent in this model; due to this symmetry the attractive Hubbard model is actually known to be mathematically equivalent to the repulsive one. Namely, the Shiba transformation [128, 129],

$$\hat{c}^{\dagger}_{j\uparrow} \leftrightarrow (-1)^{j}\hat{c}_{j\uparrow}, \tag{5.2}$$

transforms them each other, where we make an electron-hole transformation for one spin direction with a phase factor that discriminates A and B sublattices for a bipartite lattice. Under this transformation, the onsite interaction changes its sign as

$$\left(\hat{n}_{i\uparrow}-\frac{1}{2}\right)\left(\hat{n}_{i\downarrow}-\frac{1}{2}\right) \leftrightarrow -\left(\hat{n}_{i\uparrow}-\frac{1}{2}\right)\left(\hat{n}_{i\downarrow}-\frac{1}{2}\right). \tag{5.3}$$

On the other hand, the nearest-neighbor hopping term transform as

$$\sum_{ij} t_{i,j}\hat{c}^{\dagger}_{i\uparrow}\hat{c}_{j\uparrow} \leftrightarrow \sum_{ij} t^{*}_{j,i}\hat{c}^{\dagger}_{j\uparrow}\hat{c}_{i\uparrow} = \sum_{ij} t^{*}_{i,j}\hat{c}^{\dagger}_{i\uparrow}\hat{c}_{j\uparrow}, \tag{5.4}$$

since $t_{i,j} = t^{*}_{j,i}$, so that the hopping term is invariant for ordinary real hopping amplitudes. Hence the repulsive and attractive Hubbard model are converted with each other by this transformation.

However, we should notice that the particle number operator converts as

$$\hat{n}_i \leftrightarrow -\hat{S}^{z}_{i}, \tag{5.5}$$

where $\hat{S}^{z}_{i}$ is the z component of the spin at site i. Namely, if one considers a grand-canonical ensemble for systems attached to a particle reservoir with a chemical potential term, the equivalence is lost, since the particle number changes in this transformation between the attractive and repulsive cases, unless the system is at half filling (electron-hole symmetric point).

An important consequence of the Shiba transformation is that the spin operator,

$\hat{\boldsymbol{S}}_j$, at site j converts to a pseudospin $\hat{\boldsymbol{\eta}}_j$,

$$\hat{\boldsymbol{S}}_j \leftrightarrow \hat{\boldsymbol{\eta}}_j. \tag{5.6}$$

Here $\hat{\boldsymbol{\eta}}_j$ is a hermitian operator defined as

$$\hat{\eta}_j^x + i\hat{\eta}_j^y = (-1)^j \hat{c}_{j\uparrow}\hat{c}_{j\downarrow}, \tag{5.7}$$

$$\hat{\eta}_j^z = \frac{1}{2}(1 - \hat{n}_{j\uparrow} - \hat{n}_{j\downarrow}). \tag{5.8}$$

The Shiba transformation converts the ordinary spin-SU(2) symmetry on the repulsive side into η-SU(2) symmetry on the attractive side, which implies that the Hubbard model has, in addition to the ordinary spin-SU(2) symmetry with respect to $\hat{\boldsymbol{S}} = \sum_i \hat{\boldsymbol{S}}_i$, the η-SU(2) symmetry with respect to $\hat{\boldsymbol{\eta}} = \sum_i \hat{\boldsymbol{\eta}}_i$.

Then, we can ask ourselves: when the attractive and repulsive cases are equivalent, can any difference emerge between them when the system is put out of equilibrium? Indeed, we can see that the η-SU(2) symmetry is immediately broken when an external field is turned on . While the hopping term is invariant under the Shiba transformation as long as the amplitude is real as we have seen above, so that in the presence of an external field that produces a Peierls phase, the hopping term acquires spin-dependent phase factor as

$$\sum_{ij} t_{ij} e^{-i\boldsymbol{A}(t)\cdot(\boldsymbol{R}_i - \boldsymbol{R}_j)} \hat{c}_{i\sigma}^\dagger \hat{c}_{j\sigma} \leftrightarrow \sum_{ij} t_{ij}^* e^{i\sigma\boldsymbol{A}(t)\cdot(\boldsymbol{R}_i - \boldsymbol{R}_j)} \hat{c}_{i\sigma}^\dagger \hat{c}_{j\sigma} \tag{5.9}$$

by the transformation. Namely, the system no longer has the η-SU(2) symmetry under an external field even at half filling.

From this observation, the behavior of the η-spin in nonequilibrium in the attractive case should be crucially different from the real spin in the repulsive case even though the η-spin is transformed into the real spin, and physics peculiar to the periodically-driven attractive Hubbard model is expected to arise. This motivates us to investigate here the driven attractive Hubbard model. There, we concentrate on the strong-coupling regime, since the low-energy degree of freedom in that regime is described by the Heisenberg model for the η-spins, so that breaking of the η-SU(2) symmetry by the external field should significantly affect the low-energy structure.

5.3 Strong-coupling expansion

Since we consider the strong-coupling regime of the attractive Hubbard model, we can directly apply the framework for the strong-coupling expansion developed in the

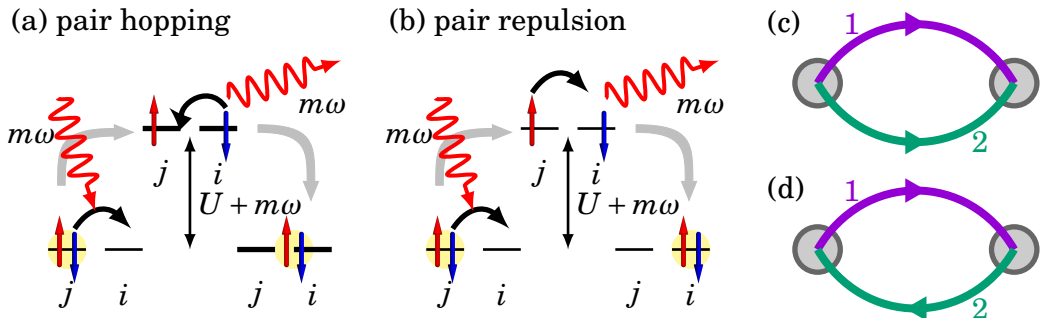

Figure 5.1: Schematic representation of the virtual processes in the strong-coupling expansion: (a) the pair-hopping process, (b) the pair-repulsion process. Red and blue arrows represent up and down spins, gray arrows virtual transitions, black arrows fermion hopping, and wave lines the coupling to photons. (c) and (d) represent diagrams corresponding, respectively, to (a), (b) in Fig. 4.5.

previous chapter. A significant difference from the repulsive case is that here we consider the sector with a maximal double occupancy, rather than the zero sector. Hereafter we consider a three-dimensional cubic geometry and a laser linearly polarized along [1,1,1] direction with a vector potential[1]

$$\boldsymbol{A}(t) = A(1,1,1)\cos\omega t. \tag{5.10}$$

The low-energy effective Hamiltonian $\hat{H}_{\text{pair}}$ described by the η-spin is expressed, in the leading order, as

$$\hat{H}_{\text{pair}} = J_0 \sum_{ij}^{\text{n.n.}} (\hat{\eta}_i^x \hat{\eta}_j^x + \hat{\eta}_i^y \hat{\eta}_j^y) + V_0 \sum_{ij}^{\text{n.n.}} \hat{\eta}_i^z \hat{\eta}_j^z \tag{5.11}$$

$$= -J_0 \sum_{ij}^{\text{n.n.}} \hat{c}_{i\uparrow}^\dagger \hat{c}_{i\downarrow}^\dagger \hat{c}_{j\downarrow} \hat{c}_{j\uparrow} + V_0 \sum_{ij}^{\text{n.n.}} \frac{\hat{n}_i}{2} \frac{\hat{n}_j}{2}, \tag{5.12}$$

with a nearest-neighbor pair hopping J_0 and a nearest-neighbor repulsion V_0. In the absence of external fields, J_0 and V_0 have same value $J_0 = V_0 = 2/U$, due to the η-SU(2) symmetry.

When a periodic driving is turned on, the hopping amplitude is decomposed into Fourier components as $t_{ij}^{(m)} = i^m \mathscr{J}_m(\boldsymbol{A} \cdot \boldsymbol{R}_{ji})$ as we have seen in Sec. 4.2. With this, one can apply Eq. (4.23) projected onto the sector with the maximal double occupancy. The lowest-order virtual processes in the strong-coupling expansion are schemati-

[1]For optical lattice systems, the spatially-uniform vector potential introduced via the Peierls phase can be emulated by shaking the lattice.

cally shown in Fig. 5.1. Here we can explicitly observe the breaking of the η-SU(2) symmetry derived form the external field: While the virtual process for the pair repulsion in Eq. (5.12) consists of the hopping from j-th to i-th and then back from i-th to j-th, that for the pair hopping consists of the hopping from j-th to i-th site twice. Thus they have different phase factors, respectively $|t_{ij}^{(m)}|^2$ and $(t_{ij}^{(m)})^2$, so that the pair hopping J_{eff} and repulsion V_{eff} in the effective Hamiltonian,

$$\hat{F} = -J_{\text{eff}} \sum_{ij}^{\text{n.n.}} \hat{c}_{i\uparrow}^{\dagger} \hat{c}_{i\downarrow}^{\dagger} \hat{c}_{j\downarrow} \hat{c}_{j\uparrow} + V_{\text{eff}} \sum_{ij}^{\text{n.n.}} \frac{\hat{n}_i}{2} \frac{\hat{n}_j}{2} \tag{5.13}$$

are no longer the same. They are expressed as

$$J_{\text{eff}} = \sum_{m=-\infty}^{\infty} (-1)^m \frac{2\mathscr{J}_m(A)^2}{U + m\omega}, \tag{5.14}$$

$$V_{\text{eff}} = \sum_{m=-\infty}^{\infty} \frac{2\mathscr{J}_m(A)^2}{U + m\omega} \tag{5.15}$$

in time average. As we have mentioned, this difference is peculiar to the attractive case with the broken η-SU(2) symmetry, as opposed to the repulsive case with the intact spin-SU(2) symmetry even in the periodic driving.

Let us first see how the ground state changes for the broken invariance between J_{eff} and V_{eff}. Figure 5.2(a) shows a mean-field result for the phase diagram against J_{eff}, V_{eff} and the electron filling n. In the absence of the periodic driving ($J_{\text{eff}} = V_{\text{eff}}$), the ground state is the conventional s-wave superconductivity as the dashed line represents. Only at exact half filling, the charge-density wave (CDW) state degenerates due to the η-SU(2) symmetry. If the pair repulsion dominates the pair hoping, ground state changes into the charge-density wave, with the phase boundary given as

$$V_{\text{eff}} = |J_{\text{eff}}| \left(1 + \frac{2(n-1)^2}{(2-n)n}\right). \tag{5.16}$$

If one considers the pair attraction rather than repulsion, the phase separation of occupied sites and empty sites occur with a phase boundary,

$$V_{\text{eff}} = -|J_{\text{eff}}|. \tag{5.17}$$

Furthermore, in the case of dominant negative hopping amplitudes, the η-pairing superconductivity emerges as the ground state: As schematically shown in Fig. 5.3, the conventional superconductivity in the strong-coupling regime can be regarded as a Bose-Einstein condensate of bosons (fermion pairs) at the band bottom (usually

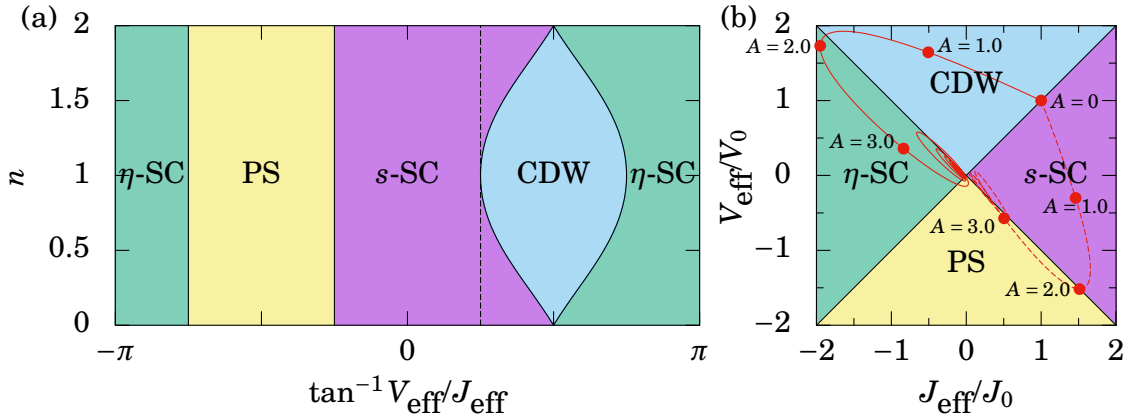

Figure 5.2: The phase diagram for the periodically-driven Hubbard model in the strong-coupling regime. s-SC, η-SC, CDW, and PS respectively represent s-wave superconductivity, η-pairing superconductivity, charge-density wave, and phase separation. (a) The phase diagram against the electron filling n and $\tan^{-1} V_{\rm eff}/J_{\rm eff}$. A dashed line indicates the undriven situation. Here $\tan^{-1} V_{\rm eff}/J_{\rm eff}$ is defined as the angle in the $J_{\rm eff}, V_{\rm eff}$-plane with $|\tan^{-1} V_{\rm eff}/J_{\rm eff}| \lesseqgtr \pi/2$ for $J_{\rm eff} \gtreqless 0$. (b) The phase diagram against $J_{\rm eff}$ and $V_{\rm eff}$ for $n = 1$. Red solid (dashed) curve represents the trajectory of $(J_{\rm eff}(A), V_{\rm eff}(A))$ for $\omega = 0.8U$ ($\omega = 1.2U$).

at the Γ point), so that the sign inversion of the hopping amplitude flip the band structure for the bosons with its bottom changing from $\boldsymbol{k} = 0$ to $\boldsymbol{k} = \boldsymbol{Q} = (\pi, \pi, \pi)$. In such a situation the Cooper pair has a finite (in fact maximal) total momentum at the Brillouin zone corner, which is nothing but the η-pairing superconductivity. Such an exotic condition has not been realized in real systems so far, but here we find that this can indeed be realized for an effective Floquet Hamiltonian of the periodically-driven attractive Hubbard model.

To see this, here we examine the behavior of the parameters $J_{\rm eff}$ and $V_{\rm eff}$ in Eqs. (5.14) and (5.15) and a resultant change in the ground state. Figure 5.4 shows the behavior of the parameters as a function of A for various values of ω. Let us start with the $\omega \gg U$ limit shown in Fig. 5.4(a), where the $m \neq 0$ components in Eqs. (5.14) and (5.15) vanish. As a result, just a rescaling of the energy as $J_{\rm eff} = V_{\rm eff} = \mathscr{J}_0^2(A)V_0$ occurs and the η-SU(2) symmetry is intact. This situation can be interpreted as a dynamical localization of individual electrons.

The breaking of the η-SU(2) symmetry is induced by $m \neq 0$ components, so that the breaking should be significant if they have a large contribution. This feature is captured in the case of $\omega = 1.2U$ and $\omega = 0.8U$ respectively shown in Fig. 5.4(b) and 5.4(c). In these cases, $J_{\rm eff}$, $V_{\rm eff}$ have drastic dependence on the field, where the signs

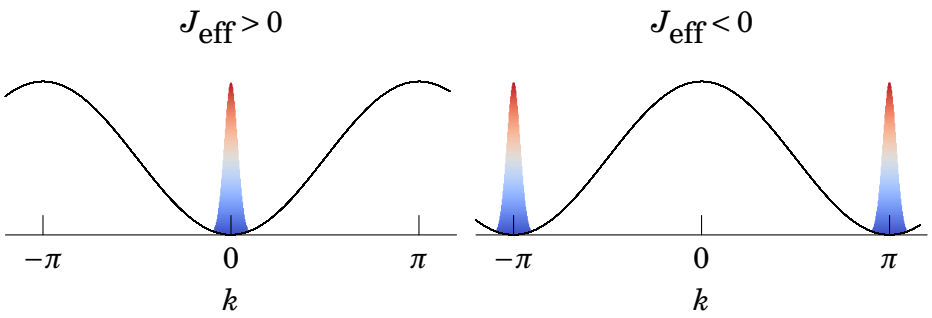

Figure 5.3: A schematic picture of the conventional s-wave superconductivity in $J_{\rm eff} > 0$ and the η-pairing superconductivity in $J_{\rm eff} < 0$ in the strong coupling regime, with the fermion pairs regarded as molecular bosons. The sinusoidal curve represents the band dispersion for each case, while the colored peak represents the momentum distribution.

can even be inverted. Their approximate forms are

$$J_{\rm eff} \sim -\frac{2\mathscr{J}_1(A)^2}{U-\omega}, V_{\rm eff} \sim \frac{2\mathscr{J}_1(A)^2}{U-\omega}, \tag{5.18}$$

since the $m = -1$ component has a dominant contribution due to the small denominator. We also note that $J_{\rm eff}$ and $V_{\rm eff}$ have opposite behaviors between the $\omega = 0.8U$ and $\omega = 1.2U$ cases, which is due to the sign inversion of the denominators.

This drastic difference between the pair hopping and pair repulsion leads to a change of the ground state. A small amplitude driving stabilizes the s-wave superconductivity or the CDW according to the sign of $U - \omega$. Remarkably, for larger amplitude $A \gtrsim 1$, the pair hopping and pair repulsion can even invert their signs, which should lead to new ground states, the η-pairing superconductivity and phase separation mentioned above. We represent this as a trajectory of $J_{\rm eff}$ and $V_{\rm eff}$ as A is increased on the phase diagram at half filling in Fig. 5.2(b). We can see that for $A \gtrsim 2$ we can realize the effective Hamiltonian with the η-pairing ground state for $\omega = 0.8U$. We can decrease the necessary amplitude by destabilizing the CDW phase with doping, since the CDW phase shrinks as we go away from the half filling [see Fig. 5.2(a)].

If we consider smaller values of ω, the $m = -2, -3, \ldots$ components begin to have large contributions in the vicinity of $\omega = U/2, U/3, \ldots$, respectively. Since the m-th Bessel function can be expanded as

$$\mathscr{J}_m(A) = \frac{A^m}{2^m m!} + \mathscr{O}(A^{m+2}), \tag{5.19}$$

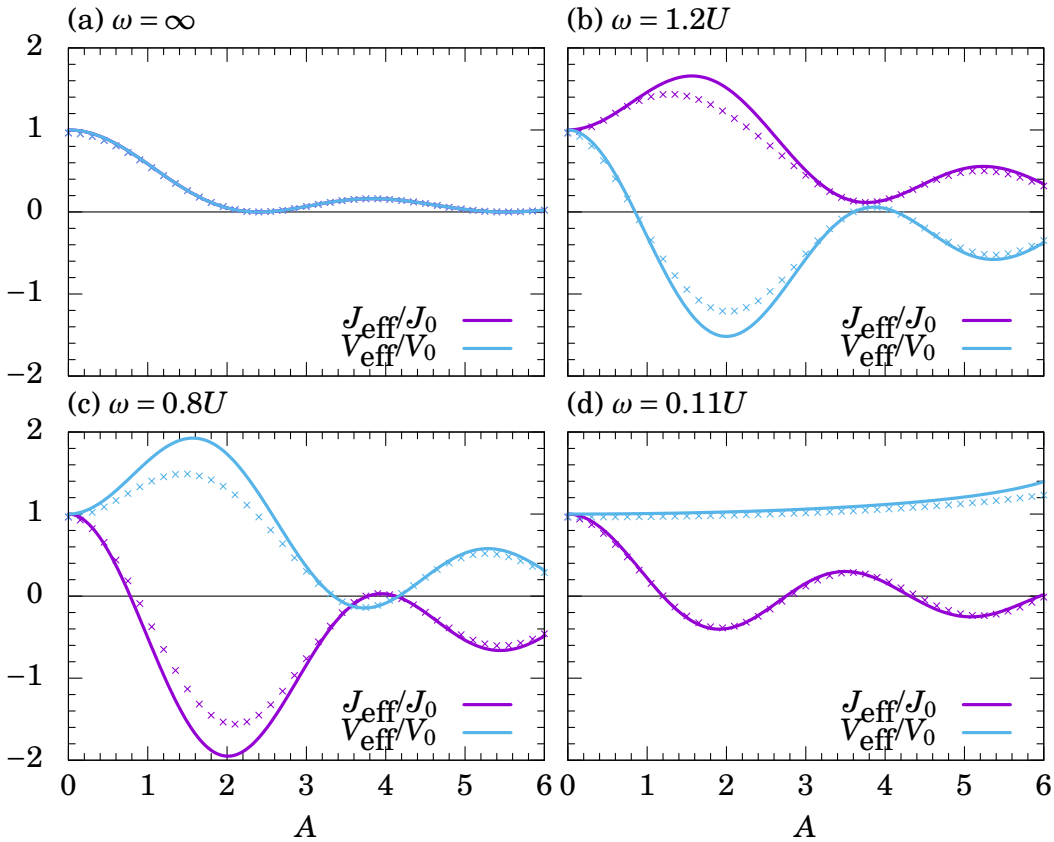

Figure 5.4: The pair-hopping amplitude $J_{\rm eff}$ and pair repulsion $V_{\rm eff}$ against A. (a) $\omega = \infty$, (b) $\omega = 1.2U$, (c) $\omega = 0.8U$, and (d) $\omega = 0.11U$. Solid lines represent the perturbative form, Eqs. (5.14) and (5.15), while the crosses the numerical results for a two-site system with $U = 10$.

the m-th component contribution appears in a larger A regime for larger $|m|$. In the small A regime where the $|m| \sim U/\omega$ contribution is small, the parameters asymptotically approaches to

$$J_{\text{eff}} \sim J_0 \mathscr{J}_m(2A), V_{\text{eff}} \sim V_0, \tag{5.20}$$

which is obtained from the $\omega/U \to 0$ limit in Eqs. (5.14) and (5.15) with the Gegenbauer addition formula,

$$\sum_{n=-\infty}^{\infty} \mathscr{J}_n(x)\mathscr{J}_n(y)e^{-in\theta} = \mathscr{J}_0(\sqrt{x^2+y^2-2xy\cos\theta}). \tag{5.21}$$

This behavior is captured in the $\omega = 0.11U$ case shown in Fig. 5.4(d). This is nothing but the dynamical localization of charge 2 particles, which is indeed consistent with the fact that ω there is too small to destruct pairs with binding energy U. In this situation the CDW phase is stable although the inversion of the hopping amplitude can occur.

In addition to the perturbative form Eqs. (5.14) and (5.15), we also plot the numerically exact value for the two-site model with $U = 10$ in Fig. 5.4 with crosses. The perturbative and numerical results agree well with each other, which indicates that the strong-coupling expansion (truncated at the leading order) is rather accurate. The agreement is especially good in the large amplitude regime, due to the dynamical localization.

To summarize, while each fermion is subject to the dynamical localization in the high-frequency regime, fermion pairs (bosons) are subject to the dynamical localization in the low-frequency (but higher than the energy scale of the pair hopping) regime. While no new ground states emerge in these regimes, they do not crossover to one another continuously: In the intermediate regime the electron pairing can be broken with Floquet photon absorption and emission as depicted in Fig. 5.1, and an exotic Hamiltonian with the η-pairing ground state can be realized when such virtual processes are intense.

5.4 Stability analysis

5.4.1 Instability in elementary excitations

While we have observed the ground state of the effective Hamiltonian so far, steady states realized in periodically-driven systems can in general be nontrivial and different from the ground state as we have mentioned in Chapter 2. Since we are interested in the realization of the exotic η-pairing superconductivity, hereafter we investigate whether we can actually induce a dynamical phase transition from the

ordinary s-wave to η-pairing.

To this end, an examination of the stability of the s-wave superconductivity under the effective Hamiltonian gives a crucial hint. In fact, as we shall see below, the collapse of the s-wave superconductivity toward the η pairing is classified as a Landau instability in the presence of an energy dissipation, while that toward the CDW as the dynamical instability [130], which can emerge even in isolated systems and thus play an important role in the periodically-driven systems.

To discuss the stability of the system, let us formulate the dynamics of the system under the effective Hamiltonian with the mean-field approximation here. To describe the time evolution of the superconductor, we employ a time-dependent ansatz for the wave function

$$|\Psi\rangle = \exp\left[\sum_j \Psi_j(t)\hat{c}^\dagger_{j\uparrow}\hat{c}^\dagger_{j\downarrow}\right]|0\rangle. \tag{5.22}$$

We can derive the equation of motion for this wave function by introducing an action functional,

$$\mathscr{S} = \int dt\, \frac{\langle\Psi|(\hat{F} - i\partial_t)|\Psi\rangle}{\langle\Psi|\Psi\rangle}, \tag{5.23}$$

for the effective Hamiltonian Eq. (5.13) to obtain stationary points. We then have

$$i\frac{\partial\Psi_i}{\partial t} = \sum_j^{\text{n.n.}} \frac{1}{1+|\Psi_j|^2}\left[-J_{\text{eff}}\Psi_j + J_{\text{eff}}\Psi_j^*\Psi_i^2 + 2V_{\text{eff}}|\Psi_j|^2\Psi_i\right], \tag{5.24}$$

which is analogous to the time-dependent Gross-Pitaevskii equation. The s-wave superconductor is represented as a spatially-uniform Ψ_i, which is in fact a stationary solution of Eq. (5.24) as

$$\Psi_0(t) = \sqrt{\frac{n}{2-n}}\exp\{-iz[(n-1)J_{\text{eff}} + nV_{\text{eff}}]t\} \tag{5.25}$$

for arbitrary J_{eff} and V_{eff}. Here $z = \sum_j^{\text{n.n.}} 1$ is the coordination number of the lattice.

While the pure s-wave superconductivity turned out to be stationary under the effective Hamiltonian, it does not necessarily imply the stability of the s-wave superconductivity. We can check the stability by considering a small perturbation $\delta\Psi$ to the macroscopic wave function Ψ to see how it evolves [127]. We express the wave function with the perturbation as

$$\Psi_i(t) = \Psi_0(t)\left[1 + \sum_{\boldsymbol{k}} \delta\Psi_{\boldsymbol{k}}(t)e^{i\boldsymbol{k}\cdot\boldsymbol{R}_i}\right], \tag{5.26}$$

then the equation of motion Eq. (5.24) can be linearized with respect to $\delta\Psi_{\boldsymbol{k}}$ as

$$i\frac{\partial}{\partial t}\begin{pmatrix}1 & 0\\ 0 & -1\end{pmatrix}\begin{pmatrix}\delta\Psi_{\boldsymbol{k}}\\ \delta\Psi^*_{-\boldsymbol{k}}\end{pmatrix} = J_{\mathrm{eff}}\begin{pmatrix}\mu_{\boldsymbol{k}}+\sigma_{\boldsymbol{k}} & \sigma_{\boldsymbol{k}}\\ \sigma_{\boldsymbol{k}} & \mu_{\boldsymbol{k}}+\sigma_{\boldsymbol{k}}\end{pmatrix}\begin{pmatrix}\delta\Psi_{\boldsymbol{k}}\\ \delta\Psi^*_{-\boldsymbol{k}}\end{pmatrix}, \tag{5.27}$$

where

$$\mu_{\boldsymbol{k}} = 2\sum_j^{\text{n.n.}} \sin^2\frac{\boldsymbol{k}\cdot\boldsymbol{R}_{ji}}{2}, \tag{5.28}$$

$$\sigma_{\boldsymbol{k}} = \frac{n(2-n)}{2}\left(1+\frac{V_{\mathrm{eff}}}{J_{\mathrm{eff}}}\right)\sum_j^{\text{n.n.}}\cos\boldsymbol{k}\cdot\boldsymbol{R}_{ji}. \tag{5.29}$$

While Eq. (5.27) can be reduced to an eigenvalue problem, as in the Bogoliubov equation for Bose-Einstein condensates, we should be aware that this equation describes the time evolution of elementary excitations and their charge conjugations[2] unlike the ordinary Schrödinger equation. Eq. (5.27) can be solved via the Bogoliubov transformation,

$$B_\alpha^\dagger = \begin{pmatrix}\cosh\alpha & \sinh\alpha\\ \sinh\alpha & \cosh\alpha\end{pmatrix}. \tag{5.30}$$

While this transformation is not unitary, the Bogoliubov norm

$$\langle\delta\Psi|\sigma_3|\delta\Psi\rangle = |\delta\Psi_{\boldsymbol{k}}|^2 - |\delta\Psi^*_{-\boldsymbol{k}}|^2, \tag{5.31}$$

is conserved under the transformation since $B_\alpha\sigma_3 B_\alpha^\dagger = \sigma_3$. The eigenvectors form an orthonormal basis with respect to the Bogoliubov inner product $\langle u|\sigma_3|v\rangle$. The Bogoliubov norm is not positive definite, and antisymmetric against the charge conjugation; the positive (negative) norm implies that the state vector represents a particle (antiparticle). Indeed, the Bogoliubov norm corresponds to whether the boson operator is an annihilation or a creation operator when the excitation is quantized as a boson.

By choosing α as

$$\alpha = \tanh^{-1}\frac{\sqrt{\mu_{\boldsymbol{k}}+2\sigma_{\boldsymbol{k}}}-\sqrt{\mu_{\boldsymbol{k}}}}{\sqrt{\mu_{\boldsymbol{k}}+2\sigma_{\boldsymbol{k}}}+\sqrt{\mu_{\boldsymbol{k}}}}, \tag{5.32}$$

we obtain

$$i\frac{\partial}{\partial t}B_\alpha^\dagger\begin{pmatrix}\delta\Psi_{\boldsymbol{k}}\\ \delta\Psi^*_{-\boldsymbol{k}}\end{pmatrix} = \begin{pmatrix}J_{\mathrm{eff}}\sqrt{\mu_{\boldsymbol{k}}(\mu_{\boldsymbol{k}}+2\sigma_{\boldsymbol{k}})} & 0\\ 0 & -J_{\mathrm{eff}}\sqrt{\mu_{\boldsymbol{k}}(\mu_{\boldsymbol{k}}+2\sigma_{\boldsymbol{k}})}\end{pmatrix}B_\alpha^\dagger\begin{pmatrix}\delta\Psi_{\boldsymbol{k}}\\ \delta\Psi^*_{-\boldsymbol{k}}\end{pmatrix}. \tag{5.33}$$

We have two eigenvalues with opposite signs, which is derived from the charge con-

[2]Here we define the charge conjugation as a combination of the momentum inversion $\boldsymbol{k}\leftrightarrow-\boldsymbol{k}$ and the complex conjugation, i.e., $\delta\Psi_{\boldsymbol{k}}\leftrightarrow\delta\Psi^*_{-\boldsymbol{k}}$.

jugation; indeed, one can obtain one eigenvector by applying the charge conjugation to another. Hence the excitation energy for the elementary excitation around the s-wave superconductivity is obtained as the eigenvalue for the positive norm solution,

$$\omega(\boldsymbol{k}) = J_{\text{eff}}\sqrt{\mu_{\boldsymbol{k}}(\mu_{\boldsymbol{k}} + 2\sigma_{\boldsymbol{k}})} \tag{5.34}$$

when $\mu_{\boldsymbol{k}} + 2\sigma_{\boldsymbol{k}} > 0$. As one can see from this relation, all the elementary excitations have a negative energy when $J_{\text{eff}} < 0$. Namely, when a coupling with a thermal bath exists, the s-wave superconductivity should collapse due to a Landau instability. However, note that the present system is periodically driven, so that it is nontrivial whether the system relaxes to the thermal equilibrium of the effective Hamiltonian. When the coupling to the thermal bath is absent or within a time scale where the heat dissipation can be neglected, the quasienergy is conserved and no Landau instability emerges.

On the other hand, the present system involves another instability: Since the eigenvalue problem is nonhermitian, the eigenvalues become imaginary when $\mu_{\boldsymbol{k}} + 2\sigma_{\boldsymbol{k}} < 0$, as

$$\omega(\boldsymbol{k}) = \pm i J_{\text{eff}}\sqrt{\mu_{\boldsymbol{k}}|\mu_{\boldsymbol{k}} + 2\sigma_{\boldsymbol{k}}|}. \tag{5.35}$$

In this case the eigenvalue cannot be interpreted as an elementary excitation, and the Bogoliubov norm is in fact zero. Imaginary eigenvalue implies that an infinitesimal perturbation $\delta\Psi$ grows exponentially, i.e., the s-wave superconductivity is unstable even in isolated systems; namely, the system exhibits a dynamical instability. The condition for the emergence of the dynamical instability can be expressed as

$$\frac{V_{\text{eff}}}{J_{\text{eff}}} < -1, \text{ or } 1 + \frac{2(n-1)^2}{n(2-n)} < \frac{V_{\text{eff}}}{J_{\text{eff}}}. \tag{5.36}$$

We have an imaginary eigenvalue at $\boldsymbol{k} = 0$, in the former case, while at $\boldsymbol{k} = \boldsymbol{Q} = (\pi, \pi, \pi)$ in the latter. Namely, it implies that these are respectively the instability toward the phase separation or the CDW state.

Let us show several examples of the dispersion relations of the elementary excitations in Fig. 5.5(a)-(d). We show the result for various values of A with $n = 1$ and $\omega = 0.8U$. We also indicate where the dynamical instability emerges for the s-wave superconductivity in Fig. 5.5(e), according to Eq. (5.36). We note that the dynamical instability toward the CDW and phase separation in $J_{\text{eff}} < 0$ ($|\tan^{-1} V_{\text{eff}}/J_{\text{eff}}| > \pi/2$) can be interpreted as the repulsive-attractive conversion of interactions due to the inverted population known, which is in repulsive Hubbard model [123].

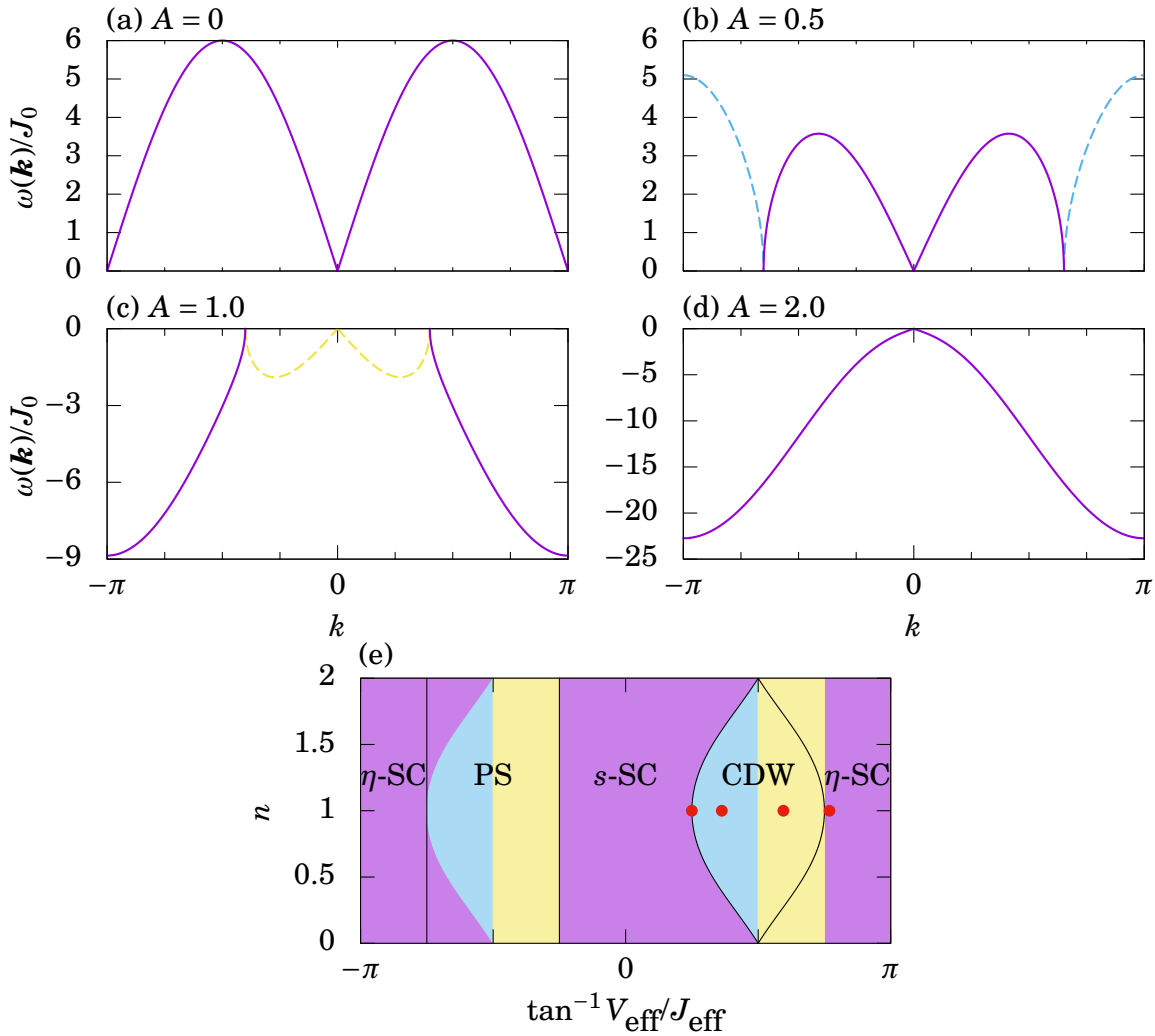

Figure 5.5: (a)-(d) Dispersions $\omega(\boldsymbol{k})$ for the elementary excitations along $\boldsymbol{k} = k(1,1,1)$ for various values of A with $n = 1$, $\omega = 0.8U$. Solid lines represent the real dispersion, Eq. (5.34), while dashed ones the imaginary modes, Eq. (5.35). (e) The phase diagram as in Fig. 5.2(a), but here colored according to the dynamical instability of s-wave superfluid: The purple regions have only real modes (i.e., stable), while the blue (yellow) ones have imaginary modes (i.e., unstable) around $\boldsymbol{k} = \boldsymbol{Q} = (\pi,\pi,\pi)$ ($\boldsymbol{k} = 0$). Red dots mark the parameters in (a)-(d).

5.4.2 Instability in terms of Hamiltonian mechanics

To grasp the origin of the dynamical instability and the associated collapse of the superconductivity, here we discuss Eq. (5.24) for a simple case where the lattice is bipartite and the state is uniform on each sublattice. While the equation becomes a coupled equation for $\Psi_A(t)$ and $\Psi_B(t)$ in that case, effective degrees of freedom are the following three:

$$\rho_Q = \frac{|\Psi_A(t)|^2}{1+|\Psi_A(t)|^2} - \frac{|\Psi_B(t)|^2}{1+|\Psi_B(t)|^2}, \tag{5.37}$$

$$2\theta = \arg\Psi_A(t) - \arg\Psi_B(t), \tag{5.38}$$

$$2\phi = \arg\Psi_A(t) + \arg\Psi_B(t) \tag{5.39}$$

due to the constraint on the particle number,

$$\frac{|\Psi_A(t)|^2}{1+|\Psi_A(t)|^2} + \frac{|\Psi_B(t)|^2}{1+|\Psi_B(t)|^2} = n. \tag{5.40}$$

The differential equations for the three variables can be rearranged under

$$H = \frac{z}{2}\left[(n^2-\rho_Q^2)V_{\text{eff}} - \sqrt{(n^2-\rho_Q^2)((2-n)^2-\rho_Q^2)}J_{\text{eff}}\cos 2\theta\right] \tag{5.41}$$

as

$$\frac{d\rho_Q}{dt} = \frac{\partial H}{\partial\theta}, \quad \frac{d\theta}{dt} = -\frac{\partial H}{\partial\rho_Q}, \tag{5.42}$$

$$\frac{dn}{dt} = \frac{\partial H}{\partial\phi} = 0, \quad \frac{d\phi}{dt} = -\frac{\partial H}{\partial n}. \tag{5.43}$$

Namely, ρ_Q and θ (or n and ϕ) can be regarded as canonical variables obeying the canonical equation under a classical Hamiltonian H. While we are interested in the time evolution of ρ_Q and θ, we can understand the behavior of these quantities without solving the equation explicitly, since they evolve along the contour of the conserved quantity H. While the time derivative of ϕ represents the chemical potential, we do not consider it hereafter since it is irrelevant to the time evolution of isolated systems.

For simplicity, we consider hereafter the case of half filling ($n = 1$), and show the contours of H for various values of A in Fig. 5.6, for $\omega = 0.8U$.

Let us see how the instability of the s-wave superconductivity emerges on the contour map. The s-wave superconductivity is represented as the origin $(\theta,\rho_Q) = (0,0)$ [and $(\theta,\rho_Q) = (\pi,0)$]. In the absence of the driving field, the origin corresponds to the

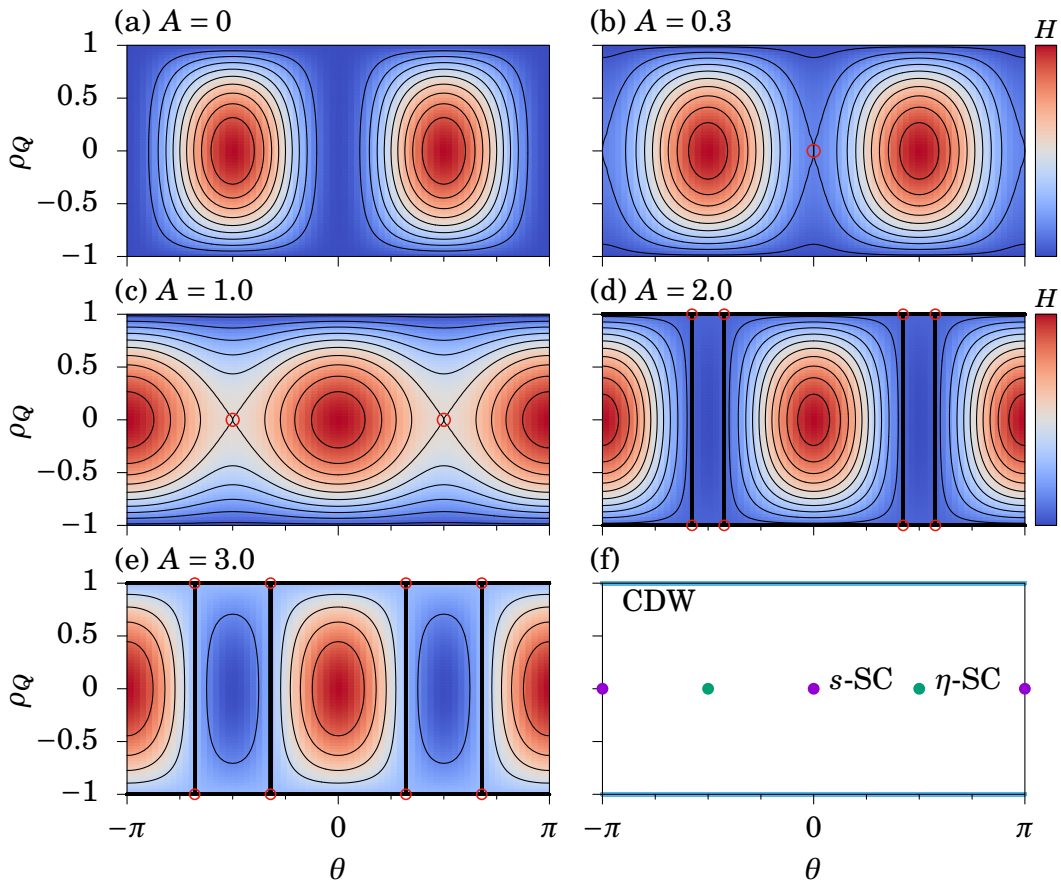

Figure 5.6: (a)-(e) Contour map of $H(\theta, \rho_Q)$ [Eq. (5.41)] for various values of A with $\omega = 0.8U$. Saddle points are marked by red circles. For (d) and (e), the contour for $H = 0$ is depicted with thick lines. (f) The location of the s-wave superconductivity $(0,0)$, $(\pi,0)$; η-pairing superconductivity $(\pm\pi/2,0)$; and charge-density wave $\rho_Q = \pm 1$ on the contour maps.

energy minima, and the state on this point does not evolve[3]. However, when the driving field is turned on to $A = 0.3$ to induce the dynamical instability for $V_{\text{eff}}/J_{\text{eff}} > 1$, a saddle point emerges at $(\theta, \rho_Q) = (0,0)$. This actually corresponds to the dynamical instability, and the CDW amplitude ρ_Q grows along the contour that contains the saddle point.

On the other hand, when we take $A = 2.0$ or 3.0, the η-pairing superconductivity is the ground state, indeed sitting at the bottom of the contour, while the s-wave superconductivity sits at the top of the energy surface, which is also a fixed point for the time evolution. We note for $A = 2.0$ that there should be a dynamical instability toward a phase separation, but it cannot be described in the present formulation where uniform solutions are assumed. Incidentally, whenever the contour is closed, the state returns to the initial state after a long enough time, but this is derived from the integrability of the equation of motion. If one takes the initial state as a nonuniform one unlike in the present formalism, the integrability is lost and the recurrence of the initial state does not happen but the relaxation toward the equilibrium described by the microcanonical ensemble happens.

We can observe the emergent instability from the saddle point not only for the s-wave superconductivity but for other ordered phases as well. For instance the case of Fig. 5.6(c), one can find the instability of the η-pairing superconductivity toward the CDW, while the instability of the CDW can be seen in Figs. 5.6(d) or 5.6(e).

5.4.3 Discussions

In this section, we have investigated the stability of the s-wave superconductivity under the periodic driving with two different formalisms. In the first formalism we have analyzed the response to general perturbations, while in the latter the global energy structure under an assumption of uniformity is explored. As an analogy with the Bose-Einstein condensation, one can classify the instability toward η-pairing superconductivity as a Landau instability while the CDW or phase separation may be regarded as a dynamical instability.

While our goal of the present study is a realization of the η-pairing, a coupling to a heat bath is essential to achieve this with the Landau instability. In general it is a nontrivial problem whether a thermal bath connected to the periodically-driven

[3]To be precise, one cannot judge whether the state on this point evolves or not only from the contour map; Indeed, for $n \neq 1$ the contour containing $(\theta, \rho_Q) = (0,0)$ shrinks into a point, and clearly no time evolution occurs (the contour map is like the case of (d) or (e) shifted by $\pi/2$ along θ), but for $n = 1$ with the η-SU(2) symmetry the ground state degenerates and the contour is a line along $\theta = 0$. However, as we have seen in the previous section, $(\theta, \rho_Q) = (0,0)$ is also a stationary solution of the equation, so that (θ, ρ_Q) will not change.

system acts to the effective static Hamiltonian like an ordinary bath, and it should depend on specific situations. Namely, to discuss the feasibility of the η pairing, we have to consider the specific set up based on the mechanism of dissipation in realistic systems for the strong-coupled attractive Hubbard model, or various regions of bath parameters.

Here let us concentrate on the most feasible candidate, ultracold atoms on optical lattices. The cold-atom systems are considered to be ideal systems to realize isolated quantum systems within the present-day technology. Since a cold-atom system is usually isolated in a trap, the dissipation is absent in the system, so that one cannot apply the scenario to cold-atom systems for the realization of the η-pairing superconductivity, which invokes the Landau instability. Thus here we leave the realization of the η-pairing superconductivity using the Landau instability as a future work. Then we can now discuss how we realize the η-pairing superconductivity in an isolated system. This will be useful even for solid-state systems for the timescale shorter than that for dissipation.

As the Landau instability is unavailable for such a setup, the dynamical instability should play a key role for inducing the desired phase transition. While no direct dynamical instabilities toward η-pairing superconductivity exist for the s-wave superconductivity, that toward the CDW is shown to exist in this section. Namely, we can expect a possibility of the dynamical phase transition toward the η-pairing by changing the field amplitude in time and induce two types of dynamical instabilities in turn as discussed in the next section.

5.5 Time evolution toward the η-pairing superconductivity in isolated systems

So we discuss temporal variations of the driving amplitude for realizing the dynamical phase transition toward the η-pairing superconductivity in this section. Now that the Hamiltonian is no longer time-periodic, the formalism adopted so far is not applicable as it is. While the effective Hamiltonian is expected to be described by the time-dependent parameters $J_{\text{eff}}(A(t))$ and $V_{\text{eff}}(A(t))$ at least in a qualitative sense, we first formulate the case in which the variation of the amplitude is sufficiently slow. We shall discuss two distinct protocols for realizing the η-pairing with sudden heating avoided: One is a two-step quench, where we induce collapses to the CDW then to η-pairing in turn. Another is an adiabatic amplitude ramping, during which similar collapses is induced.

5.5.1 Derivation of the time-dependent effective Hamiltonian

For general amplitude variations, the time-periodicity of the Hamiltonian is lost and the quasienergy is no longer conserved. Namely, the formulation using the Floquet effective Hamiltonian is not justified for the present setup. However, by recalling the procedure for deriving the effective Hamiltonian, one can notice that the strong-coupling expansion itself is applicable even in non-periodic cases, while the high-frequency expansion is not. We have imposed that the unitary transformation for the strong-coupling expansion is time-periodic, but this condition is derived from the requirement that the Hamiltonian remains time-periodic before and after the transformation. Hence, we can relax this condition for the cases where the time-periodicity of the effective Hamiltonian is not required, and the expansion is then applicable to arbitrary external fields. By expressing the counterpart of Eq. (4.11) for attractive cases, we have, to the first order in λ,

$$[-U\hat{D}, i\hat{S}^{(1)}(t)] - i\partial_t i\hat{S}^{(1)}(t) = \hat{T}(t). \tag{5.44}$$

Note for the attractive case that all the electrons form pairs so that there are no hopping processes that do not involve a change in double occupancy, which results in $\hat{H}^{(1)}_{\mathrm{SCE}} = 0$. This equation can formally be solved for arbitrary $\hat{T}(t)$ as

$$\begin{aligned} \hat{S}^{(1)}(t) &= e^{iUt\mathrm{ad}_{\hat{D}}}\hat{S}^{(1)}(0) + \int_0^t dt' e^{iU(t-t')\mathrm{ad}_{\hat{D}}}\hat{T}(t') \\ &= \sum_{d=\pm1}\left[e^{idUt}\hat{S}^{(1)}_{+d}(0) + \int_0^t dt' e^{idU(t-t')}\hat{T}_{+d}(t')\right], \end{aligned} \tag{5.45}$$

where $\hat{S}_{+d}$ and $\hat{T}_{+d}$ are defined as in Sec. 4.2. Suppose that the external field is absent for $t \le 0$, then $\partial_t\hat{S}^{(1)}(0) = 0$ reads

$$i\hat{S}^{(1)}(0) = -\sum_{d=\pm1}\frac{\hat{T}_{+d}(0)}{dU}, \tag{5.46}$$

and

$$\begin{aligned} \hat{H}^{(2)}_{\mathrm{SCE}}(t) &= \frac{1}{2}\sum_{d=\pm1}[i\hat{S}_{+d}(t), \hat{T}_{-d}(t)] \\ &= -\sum_{d=\pm1}\frac{e^{idUt}}{2dU}[\hat{T}_{+d}(0), \hat{T}_{-d}(t)] + \frac{1}{2}\sum_{d=\pm1} i\int_0^t dt' e^{idU(t-t')}[\hat{T}_{+d}(t'), \hat{T}_{-d}(t)]. \end{aligned} \tag{5.47}$$

For the case of

$$\hat{T}(t) = \sum_{i,j,\sigma} t_{i,j} e^{-i\boldsymbol{A}(t)\cdot\boldsymbol{R}_{i,j}} \hat{c}^\dagger_{i\sigma}\hat{c}_{j\sigma}, \tag{5.48}$$

we obtain the effective Hamiltonian as

$$\hat{H}^{(2)}_{\mathrm{SCE}}(t) = -\sum_{i,j} J_{i,j}(t)\hat{c}^\dagger_{i\uparrow}\hat{c}^\dagger_{i\downarrow}\hat{c}_{j\downarrow}\hat{c}_{j\uparrow} + \sum_{i,j} V_{i,j}(t)\frac{\hat{n}_i}{2}\frac{\hat{n}_j}{2} \tag{5.49}$$

where

$$J_{i,j}(t) = \frac{2t^2_{i,j}}{U} e^{-i\boldsymbol{A}(t)\cdot\boldsymbol{R}_{i,j}} \cos Ut + 2t^2_{i,j}\int_0^t dt' e^{-i(\boldsymbol{A}(t)+\boldsymbol{A}(t'))\cdot\boldsymbol{R}_{i,j}} \sin U(t-t'), \tag{5.50}$$

$$V_{i,j}(t) = \frac{2|t_{i,j}|^2}{U}\cos[\boldsymbol{A}(t)\cdot\boldsymbol{R}_{i,j}]\cos Ut + 2|t_{i,j}|^2\int_0^t dt' \cos[(\boldsymbol{A}(t')-\boldsymbol{A}(t))\cdot\boldsymbol{R}_{i,j}]\sin U(t-t'). \tag{5.51}$$

This is indeed the generalization of the case of periodic driving to arbitrary external field $\boldsymbol{A}(t)$. The expression is represented as an integral of the cause from all past times, where the first term in Eqs. (5.50) and (5.51) represents the contribution for $t < 0$ while the second term those for $t > 0$. The first term vanishes in time average if the driving frequency does not coincide with U, at which point the expansion becomes ill-defined. This implies that the correlation with past can be neglected after a time scale $\sim \omega^{-1}$.

5.5.2 Protocol I: Two-step amplitude quench

Having formulated the time evolution of the driven system with temporal variations of the field amplitude, here we keep track of the order parameters, which consist of the s-wave gap function

$$\Delta_0 = \frac{2}{N}\sum_j \langle \hat{c}_{j\downarrow}\hat{c}_{j\uparrow}\rangle, \tag{5.52}$$

the η-pairing gap function,

$$\Delta_Q = \frac{2}{N}\sum_j (-1)^j \langle \hat{c}_{j\downarrow}\hat{c}_{j\uparrow}\rangle, \tag{5.53}$$

and the CDW amplitude

$$\rho_Q = \frac{1}{N}\sum_{j,\sigma} (-1)^j \langle \hat{c}^\dagger_{j\sigma}\hat{c}_{j\sigma}\rangle. \tag{5.54}$$

We here prepare an initial states as $\Psi_i(0) = 1 + 0.001\cos(\boldsymbol{q}\cdot\boldsymbol{R}_i)$ with $\boldsymbol{q} =$

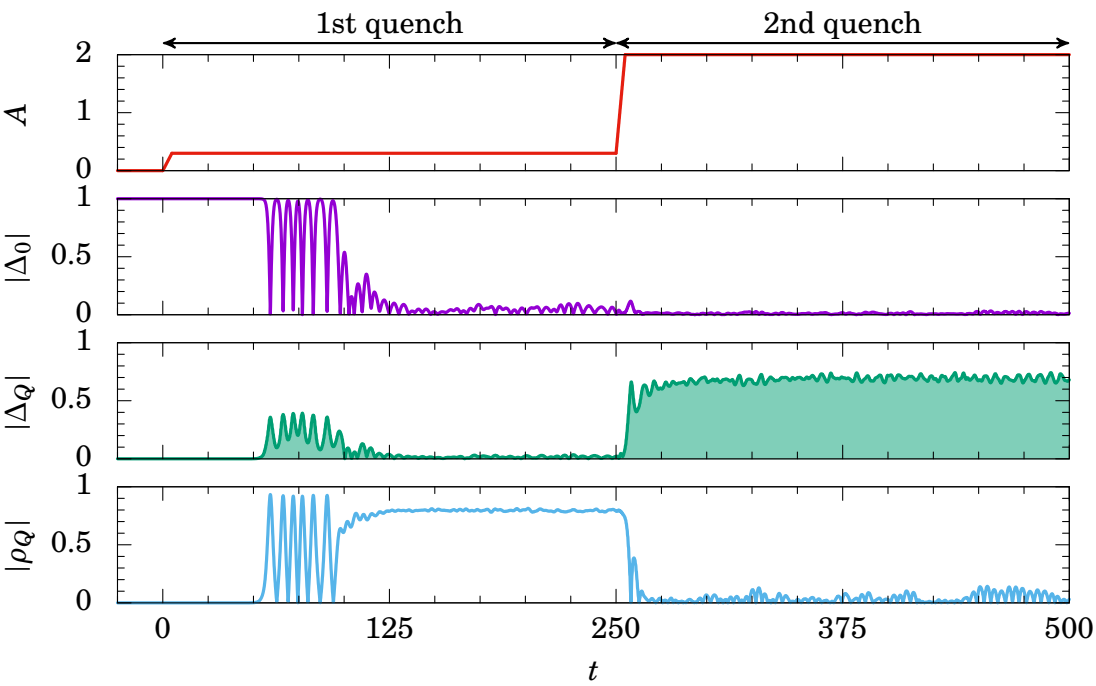

Figure 5.7: Time evolution of the order parameters for the two-step amplitude quench protocol. Here $U = 10$ and $\omega = 0.8U = 8$. The region where Δ_Q develops is highlighted in green.

$(\pi/6, \pi/6, \pi/6)$, and consider the time evolution with $U = 10$, $\omega = 8 = 0.8U$, and $\boldsymbol{A}(t) = A(t)(1,1,1)\sin\omega t$.

Figure 5.7 shows the numerical result for the time evolution within the time-dependent mean-field approximation for the two-step quench protocol. As the first quench we consider an amplitude quench from $A = 0$ to $A = A_1 = 0.3$, where the dynamical instability toward the CDW phase emerges, as seen in Sec. 5.4. In spite of the fact that the initial state is almost uniform, the s-wave gap function collapses while the CDW amplitude grows exponentially at $t \simeq 50$. The system then relaxes to a steady CDW state with no s-wave nor η-pairing amplitudes at $t \simeq 125$, which is characterized as the thermal equilibrium state of the effective static Hamiltonian for $A = A_1$. Then we consider the second step in the quench protocol. We perform an amplitude quench from $A = A_1$ to $A = A_2 = 2.0$ at $t = 250$. Then the system acquires the η-pairing ground state, while the CDW state becomes dynamically unstable. Namely, the CDW amplitude decays immediately and the system exhibits the significant η-pairing gap function after the quench.

In this protocol, the amplitudes of the intermediate steady CDW and the final η-pairing are determined mainly by how much thermodynamic work is transferred to

the system by the amplitude quenches. The CDW amplitude can be estimated with Eq. (5.13) from the total energy for the s-wave superconductivity with $|\Delta_0| = |\Delta_0^{(0)}| \neq 0$, $|\Delta_Q| = |\rho_Q| = 0$ as

$$E = -\frac{Nz}{4}|\Delta_0^{(0)}|^2 J_{\text{eff}}(A_1) + \frac{Nz}{4}n^2 V_{\text{eff}}(A_1), \tag{5.55}$$

which approximately gives the quasienergy after the quench, and thus should coincide with that after an equilibration ($|\rho_Q| = |\rho_Q^{(1)}| \neq 0$, $|\Delta_0| = |\Delta_Q| = 0$),

$$E = \frac{Nz}{4}(n^2 - \rho_Q^{(1)2})V_{\text{eff}}(A_1). \tag{5.56}$$

Namely the estimated CDW amplitude, $|\rho_Q^{(1)}|$, in the intermediate steady state is given as

$$|\rho_Q^{(1)}| = |\Delta_0^{(0)}|\sqrt{\frac{J_{\text{eff}}(A_1)}{V_{\text{eff}}(A_1)}}. \tag{5.57}$$

Note that $|\rho_Q^{(1)}| < |\Delta_0^{(0)}|$. Similarly, we can estimate the final η-pairing amplitude $|\Delta_Q^{(2)}|$ as

$$|\Delta_Q^{(2)}| = |\Delta_0^{(0)}|\sqrt{\frac{J_{\text{eff}}(A_1)}{V_{\text{eff}}(A_1)}}\sqrt{\frac{V_{\text{eff}}(A_2)}{-J_{\text{eff}}(A_2)}}. \tag{5.58}$$

This gives us a strategy for making the final amplitude large, which is to keep $|V_{\text{eff}}(A)/J_{\text{eff}}(A)|$ close to unity[4] over the whole time region in the quench protocol. This evaluation may be degraded by the slow heating due to higher-order terms in the expansion neglected here, especially when the exponential growth of the CDW amplitude Eq. (5.35) becomes slower as $|V_{\text{eff}}(A)/J_{\text{eff}}(A)|$ becomes closer to unity. A pulsed electric field due to the sudden change in the field amplitude may also induce additional heating.

5.5.3 Protocol II: Adiabatic amplitude ramping

We then introduce another protocol for realizing the sizable η-pairing gap functions, namely an adiabatic amplitude ramping, as opposed to quench protocols. While the ingredients for inducing the dynamical phase transition are essentially the same as the two-step quench protocol above, we can introduce an approximately conserved quantity during the time evolution, i.e., the adiabatic invariant for the present case, which may enrich understanding of the present system.

[4]This holds for the half filling, and in general the maximum value $|\Delta_Q^{(2)}| = |\Delta_0^{(0)}|$ is obtained when A_1 and A_2 are chosen to be the values on the phase boundary in Fig. 5.2.

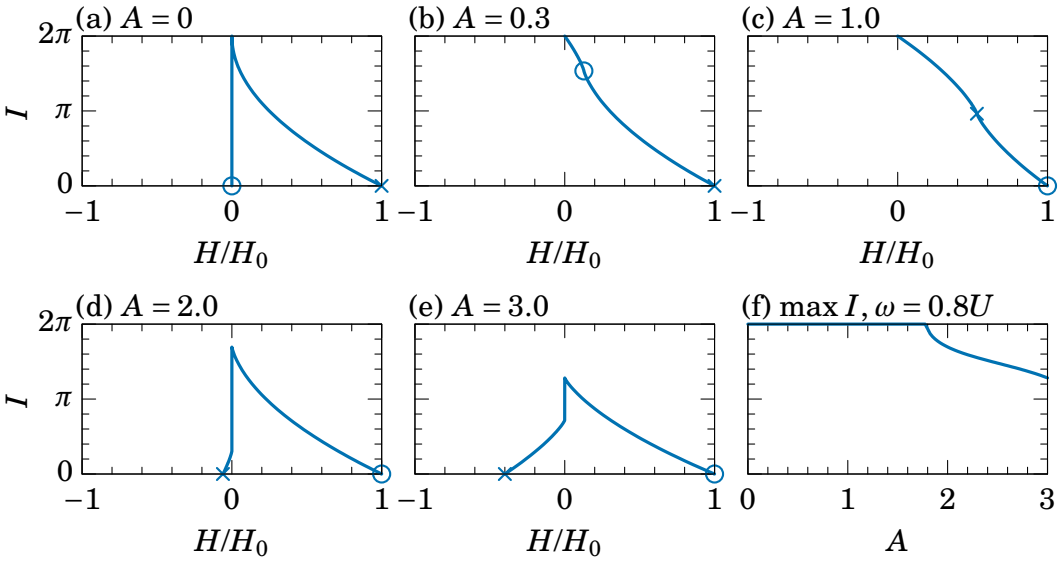

Figure 5.8: (a)-(e) The adiabatic invariant I against H for various values of A. Here H is normalized by $H_0 = (z/2)(|J_{\text{eff}}| + |V_{\text{eff}}|)$. The values for the s-wave superconductivity $H(\theta = 0, \rho_Q = 0)$ are marked by circles, while those for the η-pairing superconductivity $H(\theta = \pi/2, \rho_Q = 0)$ by crosses. The charge-density wave corresponds to $H(\rho_Q = 1) = 0$. (f) The maximum value of $I(H)$ (at $H = +0$) as a function of A, calculated here for $\omega = 0.8U$.

Here we again consider an initial state uniform on each sublattice of the bipartite lattice, whose evolution is described by the canonical equation, Eq. (5.42). In the following discussions, we assume that the time evolution is described by Eq. (5.42) with $J_{\text{eff}}(A(t))$ and $V_{\text{eff}}(A(t))$, while the numerical calculation is done without this assumption. Here we set $\omega = 0.8U$ and $n = 1$. Then we can employ the adiabatic theorem in classical mechanics [131, 132], which ensures that the adiabatic invariant,

$$I = \oint d\theta \rho_Q(\theta) \tag{5.59}$$

is conserved under a change of the parameters (J_{eff} and V_{eff} in the present case) slower as compared with the period of the motion. The adiabatic invariant represents the area enclosed by the trajectory in the phase space, which is generalized to the Boltzmann entropy for larger dimensions of the phase space[5]. We show the adiabatic invariant I as a function of H for various values of A in Fig. 5.8(a)-5.8(e).

We can again keep track of the time evolution without solving the equation of

[5]A rigorous proof for higher dimensions has been given only for ergodic systems so far, where the theorem is only applicable for an extremely slow changes of the parameters.

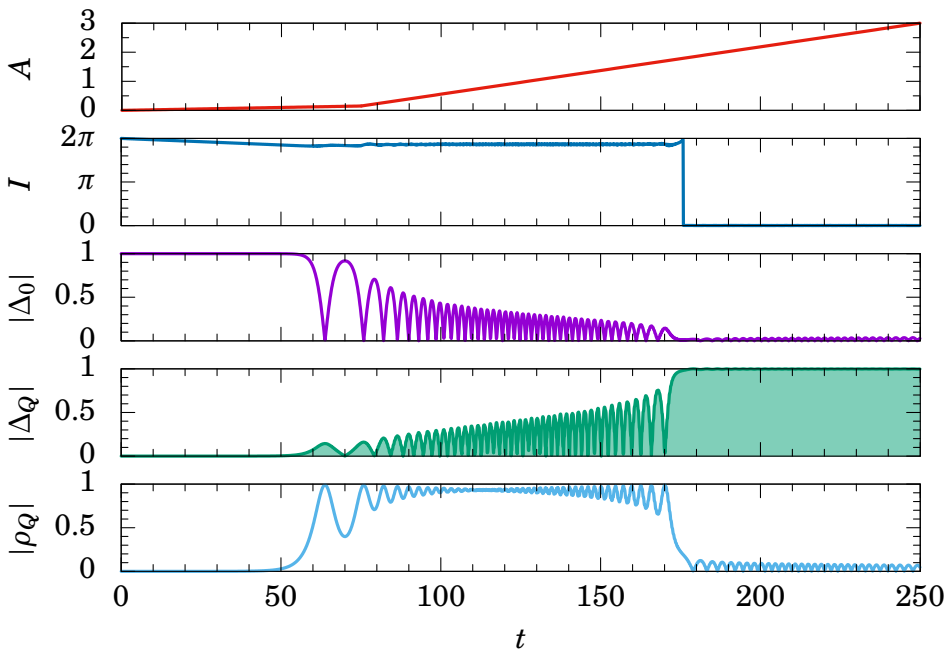

Figure 5.9: Time evolution of the order parameters for the adiabatic amplitude ramping, along with that of the adiabatic invariant I. Here $U = 10$ and $\omega = 0.8U = 8$. The region where Δ_Q develops is highlighted in green.

motion explicitly, by observing the change in the contour whose enclosing area on the contour maps coincides with the initial value of I. However, we should remark that the conservation of the adiabatic invariant is ensured only when the parameters change more slowly than the period of the motion. Namely, the adiabatic invariant has a discontinuous change even in an infinitely slow parameter change when the period of the motion diverges: This is indeed the case when the contour passes thorough a saddle point, i.e., when the dynamical instability emerges.

Let us look at how the adiabatic invariant and the order parameter evolve as the field amplitude is adiabatically changed from $A = 0$ to 3, along with the result for a numerical calculation shown in Fig. 5.9. While the initial s-wave superconductivity $(\theta, \rho_Q) = (0, 0)$ has $I = 0$ in the absence of the driving field, a dynamical instability toward the CDW state emerges when the field is turned on with an infinitesimal amplitude for the half filling[6]. Then the trajectory containing $(\theta, \rho_Q) = (0, 0)$ acquires $I = 2\pi$, which gives a discontinuous jump of the adiabatic invariant. With a finite ramp velocity the conservation of the adiabatic invariant may be degraded due to the extremely long period, but at any rate the system evolves to the CDW state with

[6]For the cases away from half filling, the adiabatic invariant remains zero up to a certain finite amplitude (see also Fig. 5.2).

I kept at a large value around 2π, which we denote here I_* (= 1.86π for the result displayed in Fig. 5.9). As the amplitude increases, the contour enclosing a large area shows a stable large CDW amplitude during the entire periodic motion.

Now the situation changes as another dynamical instability from the CDW to the η-pairing superconductivity emerges at $A \sim 1.8$. There the maximum of the adiabatic invariant $I(H = +0)$ decreases as the amplitude increases [see Fig. 5.8(f)], and at a certain A it coincides with I_*. If one increase the amplitude further, the adiabatic invariant cannot be conserved (since I_* is out of range) and has a discontinuous jump to $I(H = -0) = 2\pi - I_*$. This leads to a transition from the motion with a large I to that with a small I, namely from a motion along a contour that is close to the η-pairing ground state $(\theta, \rho_Q) = (\pi/2, 0)$. The numerical result shown in Fig. 5.9 indeed shows that the large η-pairing amplitude is achieved as desired after the ramping protocol.

5.6 Experimental implications

In the present chapter we have investigated the exotic η-pairing superconductivity induced by the dynamical instability, with a realization with ultracold atoms on an optical lattice in mind. The optical lattice system is the most promising candidate for realizing the present proposal on the attractive Hubbard model: The interaction between atoms can be tuned to a strong short-ranged attraction with the Feshbach resonance to realize the strong-coupling regime, and the periodic driving of the system can be realized by shaking the optical lattice [9]. Thus let us now discuss how the η-pairing superconductivity can be experimentally detected in ultracold atom systems.

A clear evidence for the η-pairing superconductivity is peaks in the distribution of the total momentum of the Cooper pairs concentrated around the corners of the Brillouin zone. This can be directly measured in the time-of-flight image, as has been established in the detection of the fermionic superfluids [122].

The time-of-flight image reflects the pair density in the momentum space

$$n_{\mathrm{D}}(\boldsymbol{p}) = \langle \hat{\Delta}_{\boldsymbol{p}}^{\dagger} \hat{\Delta}_{\boldsymbol{p}} \rangle, \tag{5.60}$$

where $\hat{\Delta}_{\boldsymbol{p}} = N^{-1} \sum_i \hat{c}_{i\downarrow} \hat{c}_{i\uparrow} e^{-i\boldsymbol{p}\cdot\boldsymbol{R}_i}$. We show in Fig. 5.10 a simulated time-of-flight image for typical snapshots of wave functions in the numerical simulation done for Fig. 5.7. The momentum distribution, summed over the z-axis, clearly exhibits distinct features between different phases, most notably the peaks exactly at the Brillouin zone corners for the η pairing.

For the experimental realization, the feasible temperature will be a central prob-

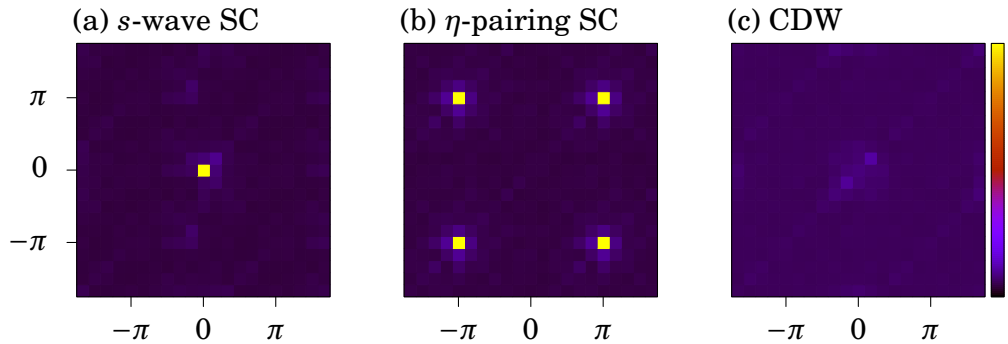

Figure 5.10: Simulated time-of-flight images for each ordered state: (a) s-wave superconductivity, (b) η-pairing superconductivity, and (c) charge-density wave.

lem. We have to cool the system below the critical temperature for the superfluid transition T_c to prepare the s-wave superfluid initial state. The required temperature is typically given as the Néel temperature for the repulsive Hubbard model, since it corresponds to T_c at half filling due to the equivalence between repulsive and attractive cases. Since the Néel order has been observed in a state-of-the-art experiment [133] for an 80-site Hubbard model on a square lattice, the required temperature for the present proposal might be available in near future. Typical values of other parameters are experimentally feasible: In the experiment reported in Ref. [133], the hopping amplitude and the onsite interaction are estimated as $t_{ij}/h = 0.90$ kHz and $U/t = 7.2$. With these parameters, the unit of time is given as $\hbar/t_{ij} = 0.18$ ms. The driving frequency $\omega \sim 0.8U$ amounts to a few kilohertz, which is achievable in shaking the optical lattice with piezo-electric actuators [9].

5.7 Summary of Chapter 5

In this chapter, we have investigated an exotic superconductivity emerging from periodic driving. By observing how the η-SU(2) symmetry in the Hubbard model behaves in nonequilibrium, we have clarified that a significant asymmetry between repulsive and attractive cases emerges in the driven Hubbard model, in particular for the η-spin degree of freedom. We then examined the strong-coupling regime of the model, using the strong-coupling expansion developed in the previous chapter. We have found that the effective model composed of the pair hopping and pair repulsion has drastic differences from that for the undriven case, and indeed has the η-pairing superconductivity as an exotic ground state.

We then note that, in order to realize the strong-coupling regime experimentally,

we should employ optical lattice systems, which is isolated from thermal baths. Without dissipation, the presence of an exotic ground state does not simply imply its realization, but some protocol for inducing a dynamical phase transition is required. From an observation of instabilities of the s-wave superconductivity, we have proposed two protocols for realizing the η-pairing superconductivity: One is a two-step amplitude quench while the other is an adiabatic amplitude ramping, and have actually demonstrated the transition as confirmed with numerical simulations.

The present study is based on the strong-coupling expansion truncated at the leading order and the mean-field approximation, which may overestimate the realizability of the η-pairing superconductivity. A systematic improvement using, e.g., the nonequilibrium dynamical mean-field theory [23] or the cluster mean-field approximation [134], remains as future works.

In particular, heating effects have not been discussed sufficiently in the present study. The collapse of the order parameter due to the dynamical instability should be significantly affected by fluctuations, which are ignored in the mean-field approximation. The Floquet prethermalization toward the CDW state, as in Figs. 5.7and 5.9 takes a long time in the present simulation, but we can expect this will occur faster in realistic situations due to various fluctuations. While this is favorable for the present proposal, the continuous heating toward infinite temperature due to the external field is underestimated by the truncation of the expansion. The deviation from the exact solution should become larger as the simulation time becomes longer, so that whether the protocol can be done before the temperature becomes too high should be discussed more precisely in future works as well.

Chapter 6

Conclusion and discussions

6.1 Summary of the thesis

In this thesis, we have investigated exotic quantum phenomena in periodically-driven systems. To this end, we have formulated perturbative expansions for three distinct regimes of periodically-driven systems: the high-frequency, small-amplitude, and strong-coupling regimes. We have particularly focused on the frequency regime where the high-frequency expansion breaks down, both in noninteracting and strongly-interacting cases. We have revealed rich possibilities for emergence of various exotic phases as follows:

Perturbative expansion based on the Brillouin-Wigner theory (Chapter 3)

We have formulated a perturbative expansion for the Floquet Hamiltonian in terms of Brillouin-Wigner theory, i.e., a framework for constructing the effective Hamiltonian for projected eigenstates, in contrast to the expansion based on the unitary transformation known previously. We have derived the high-frequency expansion based on the Brillouin-Wigner theory, and found that it has fewer number of terms compared to the Floquet-Magnus expansion or van Vleck theory, making the present formalism much more transparent. This formalism has further advantage that one can apply the same framework to other expansions such as the small-amplitude expansion. We have revealed that this framework can unify the description of Floquet topological systems in high- and low-frequency regimes as below.

Topological structures in Floquet topological insulators and Floquet Weyl semimetals under low-frequency driving (Chapter 3)

By using the Brillouin-Wigner theory, we have analyzed noninteracting two- and three-dimensional Dirac systems illuminated by circularly-polarized lasers. They are known to produce the effective Hamiltonian for the Floquet topological insulator and Floquet Weyl semimetal phases, respectively. While a complicated topological structure, which cannot be captured by the high-frequency expansion, is known to appear in the low-frequency regime for Floquet topological insulators, we have derived an effective Hamiltonian in this regime for the Dirac Hamiltonian with a continuous rotational symmetry, using the amplitude expansion in the Brillouin-Wigner formalism. We have also derived the effective Hamiltonian for the Floquet Weyl semimetals in the low-frequency regime, and found that the infinite number of Weyl nodes emerges there. We have also discussed the cases when the rotational symmetry becomes discrete by introducing lattice implementation of the Dirac dispersion, where the Weyl nodes with large monopole charges split.

Strong-coupling expansion for the Floquet Hamiltonian and photo-induced scalar spin chirality (Chapter 4)

We have discussed behaviors of the spin degree of freedom in the repulsive Hubbard model driven by ac circularly-polarized laser, using the strong-coupling expansion by extending it to periodically-driven systems. We have shown that a three-body spin correlation called the scalar spin chirality is induced, and found a remarkable enhancement compared to the case of high-frequency driving, which may extend a possibility of realizing the chiral spin liquid phase as a nonequilibrium steady state. We have also proposed that, conversely, an optical response of the Mott insulators can detect a chiral spin order as, e.g., circular dichroism.

Dynamical phase transition toward η-pairing superconductivity induced by periodic driving (Chapter 5)

We have discussed the fate of s-wave superconductivity in the attractive Hubbard model under a linearly-polarized laser. We have revealed that the η-SU(2) symmetry in the Hubbard model is significantly broken when the driving field is applied, and as a consequence the long sought-after η-pairing superconductivity emerges as an effective ground state. We then examined whether one can realize the η-pairing state during a time evolution of an isolated system, with an application to optical lattice systems in mind. By performing a stability analysis, we have shown that, while the direct phase transition from the s-wave to η-pairing superconductivity can-

not be realized without energy dissipations, there is another instability toward the charge-density wave, which occurs without dissipation. We have then shown that the η-pairing superconductivity can be realized via the charge-density wave state by changing the driving amplitude gradually. We have also discussed how to detect the η pairing experimentally in cold atom systems.

6.2 Future problems

Here we raise future problems and prospects of the present work.

Toward understanding of experiments in solid-state systems

In the present study, we have employed a perturbative scheme for all the applications: Namely, we have reduced the size of the Hilbert space and focused on the essential degree of freedom for the phenomenon of interest. While we have developed an qualitative understanding and a physical picture of the found phenomena, it might be insufficient in a quantitative sense. In particular, it should be quite important to consider heating and dissipation, which have not been discussed in this thesis, in a realistic manner for applications to solid-state systems.

On the other hand, to describe and understand various intriguing experiments microscopically, the number of relevant degrees of freedom is too large for the currently available numerical methods. The perturbative schemes developed in the present thesis have an advantage where the number of degrees of freedom is minimized. Such an approach might become important to develop an understanding of experiments in the future. Some of experimentally-observed interesting phenomena are suggested to be related to the structural distortion or transition, which is not taken into account in correlated lattice models. While it is quite difficult to treat the strong correlation and structural change on an equal footing, it would be a long-term objective to extract essential degrees of freedom in such systems with the perturbative scheme. In a short term, we should develop an understanding of weakly-correlated systems with a structural competition under a periodic driving.

Floquet topological insulators / Floquet Weyl semimetals

We have discussed that the topological structure appearing in the low-frequency regime in Chapter 3. While the whole aspect of the topological phase diagram for e.g., driven honeycomb lattice has not been clarified yet, we have revealed that there are lattice-specific contributions along with contributions from the Dirac cone in the continuous limit.

An emergence of large Chern numbers are remarkable, and a large Hall response might be realized by exploiting this structure. However, the distribution function of the (quasi)energy should be far from those in equilibrium, especially in the low-frequency regime with level resonances. Ultimately we should clarify whether one can control the distribution function, and we should first understand general behaviors of the distribution function to this end.

Laser-induced spin chirality

We have discussed the scalar spin chirality in Chapter 4. The present study may motivate to add the scalar spin chirality term to various spin models to study them.

How to characterize and detect the chiral spin liquid as a nonequilibrium state should be an important future work. While a realization in solids is desired, it would be more important to realize it in cold-atom systems, since various accurate measurements as quantum simulators should provide a deeper understanding of the unestablished nonequilibrium correlated topological phenomena.

We have also proposed to utilize the circularly-polarized laser as a probe of spin chiralities, which is desired to be improved quantitatively, by combining with the first-principle calculations.

η-pairing superconductivity

We have discussed the η-pairing superconductivity in Chapter 5. Toward its realization in cold-atom experiments, we should improve the accuracy of the simulation. We have truncated the strong-coupling expansion at the leading order, and applied the mean-field approximation. Quantitative improvement can be obtained systematically among which are: taking account of higher orders in the expansion, the cluster mean-field theory [134], stochastic mean-field approach [24], and nonequilibrium dynamical mean-field theory [23]. Taking account of interband matrix elements, which is significant in actual experiments, would be another path for improvements.

Toward applications in solid-state systems, the most important subject is how the present discussion should be modified when the attractive coupling is weaker. If we lower the driving frequency as the coupling is weakened, we finally reach the problem discussed in the excitation of the Higgs mode (on a lattice here). Since the broken η-SU(2) holds for any coupling, how the broken η-SU(2) (or the inequivalence between repulsive and attractive cases) manifests itself would be an interesting problem.

Bibliography

[1] K. Nasu, *Photoinduced Phase Transitions* (World Scientific, 2004).

[2] D. N. Basov, R. D. Averitt, D. van der Marel, M. Dressel, and K. Haule, "Electrodynamics of correlated electron materials," Rev. Mod. Phys. **83**, 471 (2011).

[3] S. Iwai, M. Ono, A. Maeda, H. Matsuzaki, H. Kishida, H. Okamoto, and Y. Tokura, "Ultrafast Optical Switching to a Metallic State by Photoinduced Mott Transition in a Halogen-Bridged Nickel-Chain Compound," Phys. Rev. Lett. **91**, 057401 (2003).

[4] D. Fausti, R. I. Tobey, N. Dean, S. Kaiser, A. Dienst, M. C. Hoffmann, S. Pyon, T. Takayama, H. Takagi, and A. Cavalleri, "Light-Induced Superconductivity in a Stripe-Ordered Cuprate," Science **331**, 189 (2011).

[5] S. Kaiser, C. R. Hunt, D. Nicoletti, W. Hu, I. Gierz, H. Y. Liu, M. Le Tacon, T. Loew, D. Haug, B. Keimer, and A. Cavalleri, "Optically induced coherent transport far above T_c in underdoped $YBa_2Cu_3O_{6+\delta}$," Phys. Rev. B **89**, 184516 (2014).

[6] M. Mitrano, A. Cantaluppi, D. Nicoletti, S. Kaiser, A. Perucchi, S. Lupi, P. Di Pietro, D. Pontiroli, M. Riccò, S. R. Clark, *et al.*, "Possible light-induced superconductivity in K_3C_60 at high temperature," Nature **530**, 461 (2016).

[7] Y. H. Wang, D. Hsieh, E. J. Sie, H. Steinberg, D. R. Gardner, Y. S. Lee, P. Jarillo-Herrero, and N. Gedik, "Measurement of Intrinsic Dirac Fermion Cooling on the Surface of the Topological Insulator Bi_2Se_3 Using Time-Resolved and Angle-Resolved Photoemission Spectroscopy," Phys. Rev. Lett. **109**, 127401 (2012).

[8] Y. H. Wang, H. Steinberg, P. Jarillo-Herrero, and N. Gedik, "Observation of Floquet-Bloch States on the Surface of a Topological Insulator," Science **342**, 453 (2013).

[9] G. Jotzu, M. Messer, M. Lebrat, T. Uehlinger, D. Greif, and T. Esslinger, "Experimental realisation of the topological Haldane model," Nature **515**, 237 (2014).

[10] F. Mahmood, C.-K. Chan, Z. Alpichshev, D. Gardner, Y. Lee, P. A. Lee, and N. Gedik, "Selective scattering between Floquet-Bloch and Volkov states in a topological insulator," Nat. Phys. **12**, 306 (2016).

[11] R. Grimm, M. Weidemüller, and Y. B. Ovchinnikov, "Optical dipole traps for neutral atoms," Adv. Atom. Mol. Opt. Phys. **42**, 95 (2000).

[12] I. Bloch, "Ultracold quantum gases in optical lattices," Nature Physics **1**, 23 (2005).

[13] M. R. Andrews, M.-O. Mewes, N. J. van Druten, D. S. Durfee, D. M. Kurn, and W. Ketterle, "Direct, Nondestructive Observation of a Bose Condensate," Science **273**, 84 (1996).

[14] M. Brzozowska, T. M. Brzozowski, J. Zachorowski, and W. Gawlik, "Nondestructive study of nonequilibrium states of cold trapped atoms," Phys. Rev. A **72**, 061401 (2005).

[15] R. Yamamoto, J. Kobayashi, K. Kato, T. Kuno, Y. Sakura, and Y. Takahashi, "Site-resolved imaging of single atoms with a Faraday quantum gas microscope," arXiv:1607.07045.

[16] A. Kamenev, "Many-body theory of non-equilibrium systems," arXiv:cond-mat/0412296.

[17] S. R. White and A. E. Feiguin, "Real-Time Evolution Using the Density Matrix Renormalization Group," Phys. Rev. Lett. **93**, 076401 (2004).

[18] N. Tsuji, T. Oka, and H. Aoki, "Correlated electron systems periodically driven out of equilibrium: Floquet+DMFT formalism," Phys. Rev. B **78**, 235124 (2008).

[19] M. Moeckel and S. Kehrein, "Interaction Quench in the Hubbard Model," Phys. Rev. Lett. **100**, 175702 (2008).

[20] G. Vidal, "Classical Simulation of Infinite-Size Quantum Lattice Systems in One Spatial Dimension," Phys. Rev. Lett. **98**, 070201 (2007).

[21] J. Berges and D. Mesterházy, "Introduction to the nonequilibrium functional renormalization group," Nucl. Phys. B (Proc. Suppl.) **228**, 37 (2012).

[22] A. Verdeny, A. Mielke, and F. Mintert, "Accurate Effective Hamiltonians via Unitary Flow in Floquet Space," Phys. Rev. Lett. **111**, 175301 (2013).

[23] H. Aoki, N. Tsuji, M. Eckstein, M. Kollar, T. Oka, and P. Werner, "Nonequilibirium dynamical mean field theory and applications," Rev. Mod. Phys. **86**, 779 (2014).

[24] D. Lacroix and S. Ayik, "Stochastic quantum dynamics beyond mean field," Eur. Phys. J. A **50**, 95 (2014).

[25] G. Floquet, "Sur les équations différentielles linéaires à coefficients périodiques," Ann. Sci. École Norm. Supér. **12**, 47 (1883).

[26] D. H. Dunlap and V. M. Kenkre, "Dynamic localization of a charged particle moving under the influence of an electric field," Phys. Rev. B **34**, 3625 (1986).

[27] A. Eckardt, C. Weiss, and M. Holthaus, "Superfluid-Insulator Transition in a Periodically Driven Optical Lattice," Phys. Rev. Lett. **95**, 260404 (2005).

[28] T. Mikami, S. Kitamura, K. Yasuda, N. Tsuji, T. Oka, and H. Aoki, "Brillouin-Wigner theory for high-frequency expansion in periodically driven systems: Application to Floquet topological insulators," Phys. Rev. B **93**, 144307 (2016).

[29] H. Lignier, C. Sias, D. Ciampini, Y. Singh, A. Zenesini, O. Morsch, and E. Arimondo, "Dynamical Control of Matter-Wave Tunneling in Periodic Potentials," Phys. Rev. Lett. **99**, 220403 (2007).

[30] A. Eckardt, M. Holthaus, H. Lignier, A. Zenesini, D. Ciampini, O. Morsch, and E. Arimondo, "Exploring dynamic localization with a Bose-Einstein condensate," Phys. Rev. A **79**, 013611 (2009).

[31] T. Ishikawa, Y. Sagae, Y. Naitoh, Y. Kawakami, H. Itoh, K. Yamamoto, K. Yakushi, H. Kishida, T. Sasaki, S. Ishihara, *et al.*, "Optical freezing of charge motion in an organic conductor," Nat. Commun. **5**, 5528 (2014).

[32] T. Oka and H. Aoki, "Photovoltaic Hall effect in graphene," Phys. Rev. B **79**, 081406 (2009).

[33] T. Kitagawa, T. Oka, A. Brataas, L. Fu, and E. Demler, "Transport properties of nonequilibrium systems under the application of light: Photoinduced quantum Hall insulators without Landau levels," Phys. Rev. B **84**, 235108 (2011).

[34] F. Casas, J. A. Oteo, and J. Ros, "Floquet theory: exponential perturbative treatment," J. Phys. A: Math. Gen. **34**, 3379 (2001).

[35] E. S. Mananga and T. Charpentier, "Introduction of the Floquet-Magnus expansion in solid-state nuclear magnetic resonance spectroscopy." J. Chem. Phys. **135**, 044109 (2011).

[36] M. Bukov, L. D'Alessio, and A. Polkovnikov, "Universal High-Frequency Behavior of Periodically Driven Systems: from Dynamical Stabilization to Floquet Engineering," Adv. Phys. **64**, 139 (2015).

[37] A. Eckardt and E. Anisimovas, "High-frequency approximation for periodically driven quantum systems from a Floquet-space perspective," New J. Phys. **17**, 093039 (2015).

[38] L. D'Alessio and M. Rigol, "Long-time Behavior of Isolated Periodically Driven Interacting Lattice Systems," Phys. Rev. X **4**, 041048 (2014).

[39] A. Lazarides, A. Das, and R. Moessner, "Equilibrium states of generic quantum systems subject to periodic driving," Phys. Rev. E **90**, 012110 (2014).

[40] T. Mori, T. Kuwahara, and K. Saito, "Rigorous Bound on Energy Absorption and Generic Relaxation in Periodically Driven Quantum Systems," Phys. Rev. Lett. **116**, 120401 (2016).

[41] T. Kuwahara, T. Mori, and K. Saito, "Floquet–Magnus theory and generic transient dynamics in periodically driven many-body quantum systems," Ann. Phys. **367**, 96 (2016).

[42] J. H. Shirley, "Solution of the Schrödinger Equation with a Hamiltonian Periodic in Time," Phys. Rev. **138**, B979 (1965).

[43] H. Sambe, "Steady States and Quasienergies of a Quantum-Mechanical System in an Oscillating Field," Phys. Rev. A **7**, 2203 (1973).

[44] N. Manakov, V. Ovsiannikov, and L. Rapoport, "Atoms in a laser field," Phys. Rep. **141**, 320 (1986).

[45] M. Grifoni and P. Hänggi, "Driven quantum tunneling," Phys. Rep. **304**, 229 (1998).

[46] S. Kehrein, *The flow equation approach to many-particle systems* (Springer, 2007).

[47] F. Faisal, "Floquet Green's function method for radiative electron scattering and multiphoton ionization in a strong laser field," Comput. Phys. Rep. **9**, 57 (1989).

[48] D. F. Martinez, "Floquet-Green function formalism for harmonically driven Hamiltonians," J. Phys. A: Math. Gen. **36**, 9827 (2003).

[49] H. Tasaki, "Typicality of Thermal Equilibrium and Thermalization in Isolated Macroscopic Quantum Systems," J. Stat. Phys. **163**, 937 (2016).

[50] P. Reimann, "Foundation of Statistical Mechanics under Experimentally Realistic Conditions," Phys. Rev. Lett. **101**, 190403 (2008).

[51] P. Reimann and M. Kastner, "Equilibration of isolated macroscopic quantum systems," New J. Phys. **14**, 043020 (2012).

[52] J. M. Deutsch, "Quantum statistical mechanics in a closed system," Phys. Rev. A **43**, 2046 (1991).

[53] M. Srednicki, "Chaos and quantum thermalization," Phys. Rev. E **50**, 888 (1994).

[54] T. N. Ikeda, Y. Watanabe, and M. Ueda, "Eigenstate randomization hypothesis: Why does the long-time average equal the microcanonical average?" Phys. Rev. E **84**, 021130 (2011).

[55] P. Reimann, "Eigenstate thermalization: Deutsch's approach and beyond," New J. Phys. **17**, 055025 (2015).

[56] A. Lenard, "Thermodynamical proof of the Gibbs formula for elementary quantum systems," J. Stat. Phys. **19**, 575 (1978).

[57] H. Tasaki, "Quantum Statistical Mechanical Derivation of the Second Law of Thermodynamics: A Hybrid Setting Approach," Phys. Rev. Lett. **116**, 170402 (2016).

[58] S. Sugiura and A. Shimizu, "Thermal Pure Quantum States at Finite Temperature," Phys. Rev. Lett. **108**, 240401 (2012).

[59] E. Altman and R. Vosk, "Universal Dynamics and Renormalization in Many-Body-Localized Systems," Annual Review of Condensed Matter Physics **6**, 383 (2015).

[60] R. Nandkishore and D. A. Huse, "Many-Body Localization and Thermalization in Quantum Statistical Mechanics," Annual Review of Condensed Matter Physics **6**, 15 (2015).

[61] P. Ponte, Z. Papić, F. m. c. Huveneers, and D. A. Abanin, "Many-Body Localization in Periodically Driven Systems," Phys. Rev. Lett. **114**, 140401 (2015).

[62] N. Tsuji, M. Eckstein, and P. Werner, "Nonthermal Antiferromagnetic Order and Nonequilibrium Criticality in the Hubbard Model," Phys. Rev. Lett. **110**, 136404 (2013).

[63] T. Shirai, T. Mori, and S. Miyashita, "Condition for emergence of the Floquet-Gibbs state in periodically driven open systems," Phys. Rev. E **91**, 030101 (2015).

[64] T. Shirai, J. Thingna, T. Mori, S. Denisov, P. Hänggi, and S. Miyashita, "Effective Floquet–Gibbs states for dissipative quantum systems," J. Phys. **18**, 053008 (2016).

[65] N. Tsuji, T. Oka, and H. Aoki, "Nonequilibrium steady state of photoexcited correlated electrons in the presence of dissipation," Phys. Rev. Lett. **103**, 1 (2009).

[66] L. Bucciantini, S. Roy, S. Kitamura, and T. Oka, "Emergent Weyl nodes and Fermi arcs in a Floquet Weyl semimetal," arXiv:1612.01541.

[67] J. E. Lennard-Jones, "Perturbation Problems in Quantum Mechanics," Proc. R. Soc. Lond. Ser. A Math. Phys. Eng. Sci. **129**, 598 (1930).

[68] Brillouin, L., "Les problèmes de perturbations et les champs self-consistents," J. Phys. Radium **3**, 373 (1932).

[69] E. P. Wigner, "On a Modification of the Rayleigh-Schrödinger Perturbation Theory," in *Part I: Physical Chemistry. Part II: Solid State Physics*, edited by A. S. Wightman (Springer Berlin Heidelberg, Berlin, Heidelberg, 1997) pp. 131–136.

[70] I. Hubač and S. Wilson, *Brillouin-Wigner Methods for Many-Body Systems* (Springer Verlag Gmbh, 2010).

[71] D. J. Thouless, M. Kohmoto, M. P. Nightingale, and M. den Nijs, "Quantized Hall Conductance in a Two-Dimensional Periodic Potential," Phys. Rev. Lett. **49**, 405 (1982).

[72] F. D. M. Haldane, "Model for a Quantum Hall Effect without Landau Levels: Condensed-Matter Realization of the "Parity Anomaly"," Phys. Rev. Lett. **61**, 2015 (1988).

[73] Y. Hatsugai, "Chern number and edge states in the integer quantum Hall effect," Phys. Rev. Lett. **71**, 3697 (1993).

[74] C. L. Kane and E. J. Mele, "Topological Order and the Quantum Spin Hall Effect," Phys. Rev. Lett. **95**, 146802 (2005).

[75] M. König, S. Wiedmann, C. Brüne, A. Roth, H. Buhmann, L. W. Molenkamp, X.-L. Qi, and S.-C. Zhang, "Quantum Spin Hall Insulator State in HgTe Quantum Wells," Science **318**, 766 (2007).

[76] I. Knez, R.-R. Du, and G. Sullivan, "Evidence for Helical Edge Modes in Inverted InAs/GaSb Quantum Wells," Phys. Rev. Lett. **107**, 136603 (2011).

[77] S. Raghu, X.-L. Qi, C. Honerkamp, and S.-C. Zhang, "Topological Mott Insulators," Phys. Rev. Lett. **100**, 156401 (2008).

[78] K. Sun, H. Yao, E. Fradkin, and S. A. Kivelson, "Topological Insulators and Nematic Phases from Spontaneous Symmetry Breaking in 2D Fermi Systems with a Quadratic Band Crossing," Phys. Rev. Lett. **103**, 046811 (2009).

[79] A. Kundu, H. A. Fertig, and B. Seradjeh, "Effective Theory of Floquet Topological Transitions," Phys. Rev. Lett. **113**, 236803 (2014).

[80] P. M. Perez-Piskunow, L. E. F. Foa Torres, and G. Usaj, "Hierarchy of Floquet gaps and edge states for driven honeycomb lattices," Phys. Rev. A **91**, 043625 (2015).

[81] S. Murakami, "Phase transition between the quantum spin Hall and insulator phases in 3D: emergence of a topological gapless phase," New J. Phys. **9**, 356 (2007).

[82] X. Wan, A. M. Turner, A. Vishwanath, and S. Y. Savrasov, "Topological semimetal and Fermi-arc surface states in the electronic structure of pyrochlore iridates," Phys. Rev. B **83**, 205101 (2011).

[83] O. Vafek and A. Vishwanath, "Dirac fermions in solids: From high-T_c cuprates and graphene to topological insulators and Weyl semimetals," Annu. Rev. Condens. Matter Phys. **5**, 83 (2014).

[84] A. Turner and A. Vishwanath, *Topological Insulators: Chapter 11. Beyond Band Insulators: Topology of Semimetals and Interacting Phases*, Contemporary Concepts of Condensed Matter Science (Elsevier Science, 2013) arXiv:1301.0330.

[85] H. B. Nielsen and M. Ninomiya, "A no-go theorem for regularizing chiral fermions," Phys. Lett. B **105**, 219 (1981).

[86] D. T. Son and B. Z. Spivak, "Chiral anomaly and classical negative magnetoresistance of Weyl metals," Phys. Rev. B **88**, 104412 (2013).

[87] A. A. Burkov, "Negative longitudinal magnetoresistance in Dirac and Weyl metals," Phys. Rev. B **91**, 245157 (2015).

[88] K. Fukushima, D. E. Kharzeev, and H. J. Warringa, "Chiral magnetic effect," Phys. Rev. D **78**, 074033 (2008).

[89] D. T. Son and N. Yamamoto, "Berry Curvature, Triangle Anomalies, and the Chiral Magnetic Effect in Fermi Liquids," Phys. Rev. Lett. **109**, 181602 (2012).

[90] R. Wang, B. Wang, R. Shen, L. Sheng, and D. Y. Xing, "Floquet Weyl semimetal induced by off-resonant light," Europhys. Lett. **105**, 17004 (2014).

[91] C.-K. Chan, P. A. Lee, K. S. Burch, J. H. Han, and Y. Ran, "When Chiral Photons Meet Chiral Fermions: Photoinduced Anomalous Hall Effects in Weyl Semimetals," Phys. Rev. Lett. **116**, 026805 (2016).

[92] S. Ebihara, K. Fukushima, and T. Oka, "Chiral pumping effect induced by rotating electric fields," Phys. Rev. B **93**, 155107 (2016).

[93] Z. Yan and Z. Wang, "Tunable Weyl Points in Periodically Driven Nodal Line Semimetals," Phys. Rev. Lett. **117**, 087402 (2016).

[94] H. Hübener, M. A. Sentef, U. de Giovannini, A. F. Kemper, and A. Rubio, "Creating stable Floquet-Weyl semimetals by laser-driving of 3D Dirac materials," Nat. Commun. **8**, 13940 (2017).

[95] P. Delplace, J. Li, and D. Carpentier, "Topological Weyl semi-metal from a lattice model," Europhys. Lett. **97**, 67004 (2012).

[96] Z. Wang, Y. Sun, X.-Q. Chen, C. Franchini, G. Xu, H. Weng, X. Dai, and Z. Fang, "Dirac semimetal and topological phase transitions in A_3Bi (A = Na, K, Rb)," Phys. Rev. B **85**, 195320 (2012).

[97] M. Neupane, S.-Y. Xu, R. Sankar, N. Alidoust, G. Bian, C. Liu, I. Belopolski, T.-R. Chang, H.-T. Jeng, H. Lin, *et al.*, "Observation of a three-dimensional topological Dirac semimetal phase in high-mobility Cd_3As_2," Nat. Commun. **5**, 3786 (2014).

[98] J. H. Mentink, K. Balzer, and M. Eckstein, "Ultrafast and reversible control of the exchange interaction in Mott insulators," Nat. Commun. **6**, 6708 (2015).

[99] R. Mikhaylovskiy, E. Hendry, A. Secchi, J. H. Mentink, M. Eckstein, A. Wu, R. Pisarev, V. Kruglyak, M. Katsnelson, T. Rasing, and A. Kimel, "Ultrafast optical modification of exchange interactions in iron oxides," Nat. Commun. **6**, 8190 (2015).

[100] J. He, S.-P. Kou, Y. Liang, and S. Feng, "Chiral spin liquid in a correlated topological insulator," Phys. Rev. B **83**, 205116 (2011).

[101] A. G. Grushin, A. Gómez-León, and T. Neupert, "Floquet Fractional Chern Insulators," Phys. Rev. Lett. **112**, 156801 (2014).

[102] S. Florens and A. Georges, "Slave-rotor mean-field theories of strongly correlated systems and the Mott transition in finite dimensions," Phys. Rev. B **70**, 035114 (2004).

[103] D. Sen and R. Chitra, "Large-U limit of a Hubbard model in a magnetic field: Chiral spin interactions and paramagnetism," Phys. Rev. B **51**, 1922 (1995).

[104] B. Bauer, L. Cincio, B. P. Keller, M. Dolfi, G. Vidal, S. Trebst, and A. W. Ludwig, "Chiral spin liquid and emergent anyons in a Kagome lattice Mott insulator," Nat. Commun. **5**, 5137 (2014).

[105] C. Hickey, L. Cincio, Z. Papić, and A. Paramekanti, "Haldane-Hubbard Mott Insulator: From Tetrahedral Spin Crystal to Chiral Spin Liquid," Phys. Rev. Lett. **116**, 137202 (2016).

[106] L. N. Bulaevskii, C. D. Batista, M. V. Mostovoy, and D. I. Khomskii, "Electronic orbital currents and polarization in Mott insulators," Phys. Rev. B **78**, 024402 (2008).

[107] E. Anisimovas, G. Žlabys, B. M. Anderson, G. Juzeliūnas, and A. Eckardt, "Role of real-space micromotion for bosonic and fermionic Floquet fractional Chern insulators," Phys. Rev. B **91**, 245135 (2015).

[108] M. Claassen, H.-C. Jiang, B. Moritz, and T. P. Devereaux, "Dynamical Time-Reversal Symmetry Breaking and Photo-Induced Chiral Spin Liquids in Frustrated Mott Insulators," arXiv:1611.07964.

[109] S. Takayoshi, H. Aoki, and T. Oka, "Magnetization and phase transition induced by circularly polarized laser in quantum magnets," Phys. Rev. B **90**, 085150 (2014).

[110] S. Takayoshi, M. Sato, and T. Oka, "Laser-induced magnetization curve," Phys. Rev. B **90**, 214413 (2014).

[111] M. R. Norman, "*Colloquium* : Herbertsmithite and the search for the quantum spin liquid," Rev. Mod. Phys. **88**, 041002 (2016).

[112] I. Mazin, H. O. Jeschke, F. Lechermann, H. Lee, M. Fink, R. Thomale, and R. Valentí, "Theoretical prediction of a strongly correlated Dirac metal," Nat. Commun. **5**, 4261 (2014).

[113] M. Hermele, V. Gurarie, and A. M. Rey, "Mott Insulators of Ultracold Fermionic Alkaline Earth Atoms: Underconstrained Magnetism and Chiral Spin Liquid," Phys. Rev. Lett. **103**, 135301 (2009).

[114] S. Taie, R. Yamazaki, S. Sugawa, and Y. Takahashi, "An SU(6) Mott insulator of an atomic Fermi gas realized by large-spin Pomeranchuk cooling," Nat. Phys. **8**, 825 (2012).

[115] S. Kitamura and H. Aoki, "η-pairing superfluid in periodically-driven fermionic Hubbard model with strong attraction," Phys. Rev. B **94**, 174503 (2016).

[116] L. N. Cooper, "Bound Electron Pairs in a Degenerate Fermi Gas," Phys. Rev. **104**, 1189 (1956).

[117] J. Bardeen, L. N. Cooper, and J. R. Schrieffer, "Microscopic Theory of Superconductivity," Phys. Rev. **106**, 162 (1957).

[118] J. Bardeen, L. N. Cooper, and J. R. Schrieffer, "Theory of Superconductivity," Phys. Rev. **108**, 1175 (1957).

[119] S. Giorgini, L. P. Pitaevskii, and S. Stringari, "Theory of ultracold atomic Fermi gases," Rev. Mod. Phys. **80**, 1215 (2008).

[120] M. Randeria and E. Taylor, "Crossover from Bardeen-Cooper-Schrieffer to Bose-Einstein Condensation and the Unitary Fermi Gas," Ann. Rev. Cond. Mat. Phys. **5**, 209 (2014).

[121] K. M. O'Hara, S. L. Hemmer, M. E. Gehm, S. R. Granade, and J. E. Thomas, "Observation of a Strongly Interacting Degenerate Fermi Gas of Atoms," Science **298**, 2179 (2002).

[122] C. A. Regal, M. Greiner, and D. S. Jin, "Observation of Resonance Condensation of Fermionic Atom Pairs," Phys. Rev. Lett. **92**, 040403 (2004).

[123] N. Tsuji, T. Oka, P. Werner, and H. Aoki, "Dynamical band flipping in fermionic lattice systems: An ac-field-driven change of the interaction from repulsive to attractive," Phys. Rev. Lett. **106**, 236401 (2011).

[124] R. Matsunaga, N. Tsuji, H. Fujita, A. Sugioka, K. Makise, Y. Uzawa, H. Terai, Z. Wang, H. Aoki, and R. Shimano, "Light-induced collective pseudospin precession resonating with Higgs mode in a superconductor," Science **345**, 1145 (2014).

[125] C. N. Yang, "η pairing and off-diagonal long-range order in a Hubbard model," Phys. Rev. Lett. **63**, 2144 (1989).

[126] C. N. Yang and S. C. Zhang, "SO_4 Symmetry in a Hubbard Model," Mod. Phys. Lett. B **4**, 759 (1990).

[127] C. Pethick and H. Smith, *Bose-Einstein Condensation in Dilute Gases* (Cambridge University Press, 2002).

[128] H. Shiba, "Thermodynamic Properties of the One-Dimensional Half-Filled-Band Hubbard Model. II Application of the Grand Canonical Method," Prog. of Theor. Phys. **48**, 2171 (1972).

[129] V. J. Emery, "Theory of the quasi-one-dimensional electron gas with strong "on-site" interactions," Phys. Rev. B **14**, 2989 (1976).

[130] B. Wu and Q. Niu, "Landau and dynamical instabilities of the superflow of Bose-Einstein condensates in optical lattices," Phys. Rev. A **64**, 061603 (2001).

[131] L. D. Landau and E. M. Lifshitz, *Mechanics* (Pergamon, Oxford, 1977).

[132] J. Liu, L. Fu, B.-Y. Ou, S.-G. Chen, D.-I. Choi, B. Wu, and Q. Niu, "Theory of nonlinear Landau-Zener tunneling," Phys. Rev. A **66**, 023404 (2002).

[133] A. Mazurenko, C. S. Chiu, G. Ji, M. F. Parsons, M. Kanász-Nagy, R. Schmidt, F. Grusdt, E. Demler, D. Greif, and M. Greiner, "Experimental realization of a long-range antiferromagnet in the Hubbard model with ultracold atoms," arXiv:1612.08436.

[134] D. Yamamoto, "Correlated cluster mean-field theory for spin systems," Phys. Rev. B **79**, 144427 (2009).